ROCKET AND LIDAR STUDIES OF WAVES AND TURBULENCE IN THE ARCTIC MIDDLE ATMOSPHERE

by

Colin Charles Triplett

RECOMMENDEND:
Dr. Uma S. Bhatt

Dr. Gerald Lehmacher

Dr. David Newman

Dr. Thomas Weingartner

Dr. Richard L. Collins
Advisory Committee Chair

Dr. Uma S. Bhatt
Chair, Department of Atmospheric Sciences

APPROVED:
Dr. Paul W. Layer
Dean, College of Natural Science and Mathematics

Dr. Michael Castellini
Dean of the Graduate School

Date

ROCKET AND LIDAR STUDIES OF WAVES AND TURBULENCE IN THE ARCTIC MIDDLE ATMOSPHERE

By

Colin Charles Triplett, M.S

A

DISSERTATION

Submitted in Partial Fulfillment

of the Requirements

for the Degree of

Doctor of Philosophy

in

Atmospheric Sciences

University of Alaska Fairbanks

August 2016

Abstract

This dissertation presents new studies of waves and turbulence in the Arctic middle atmosphere. The study has a primary focus on wintertime conditions when the large-scale circulation of the middle atmosphere is disrupted by the breaking of planetary waves associated with sudden stratospheric warming (SSW) events. We used ongoing Rayleigh lidar measurements of density and temperature to conduct a multi-year study of gravity waves in the upper stratosphere-lower mesosphere (USLM) over Poker Flat Research Range (PFRR) at Chatanika, Alaska. We analyzed the night-to-night gravity wave activity in terms of the wind structure and the ageostrophy. We find that the weak winds during disturbed conditions block the vertical propagation of gravity waves into the mesosphere. The gravity wave activity is correlated with the altitudes where the winds are weakest. During periods of weak winds we find little correlation with ageostrophy. However, during periods of stronger winds we find the USLM gravity wave activity is correlated with the ageostrophy in the upper troposphere indicating that ageostrophy in this region is a source of the gravity waves. Inter-annually we find the wintertime gravity wave activity is correlated with the level of disturbance of the middle atmosphere, being reduced in those winters with a higher level of disturbance and weaker winds. We used rocket-borne ion gauges to measure turbulence in the wintertime middle atmosphere while documenting the larger meteorological context from Rayleigh lidar and satellites. This investigation of turbulence was called the Mesosphere-Lower Thermosphere Turbulence Experiment (MTeX). During MTeX we found a highly disturbed atmosphere associated with an SSW where winds were weak and gravity wave activity was low. We found low levels of turbulence in the upper mesosphere. The turbulence was primarily found in regions of convective instability in the topside of mesospheric inversion layers (MILs). The strongest and most persist turbulence was found in a MIL that is associated with the breaking of a monochromatic gravity wave. These MTeX observations indicate that turbulence is generated by gravity wave breaking as opposed to gravity wave saturation. These MTeX findings of low levels of turbulence are consistent with recent model studies of vertical transport during SSWs and support the view that eddy transport is not a dominant transport mechanism during SSWs.

Table of Contents

Page

Signature Page i

Title Page iii

Abstract v

Table of Contents vii

List of Figures xi

List of Tables xvii

Acknowledgements xix

Chapter 1 Introduction 1

    1.1. The middle atmosphere 1

    1.2. Vertical transport in the middle atmosphere 6

    1.3. Model studies of NOx transport in the middle atmosphere 11

    1.4. Existing turbulent measurements 15

    1.5. Scope of this study 17

Chapter 2 Effects of Wind Filtering and Ageostrophic Generation on Middle Atmosphere Gravity Wave Activity at Chatanika Alaska 21

    2.1. Introduction 21

    2.2 Methods and techniques 23

        2.2.1 Rayleigh lidar 23

2.2.2 Meteorological reanalysis 25

2.3. Rayleigh lidar measurements of gravity wave activity 27

2.4. The 2009 Sudden Stratospheric Warming 31

2.5 Correlation between gravity wave activity and winds 40

2.6. Correlation between gravity wave activity and ageostrophy 45

2.7. Summary and conclusions 50

Chapter 3 CONE Ion Gauge and Rayleigh Lidar Instruments 51

3.1. Introduction 51

3.2. CONE ionization gauge 51

3.3. CONE data retrieval and methodology 56

3.4. Retrieval of density profile from CONE measurements 58

3.5. Retrieval of temperature profile from CONE measurements 66

3.6. Retrieval of small-scale fluctuations from CONE measurements 72

3.7. Estimation of turbulent parameters from CONE measurements 76

3.8. Upgrade of Rayleigh lidar system 83

3.9. Summary and conclusions 96

Chapter 4 The Mesosphere-Lower Thermosphere Turbulence Experiment 99

4.1. Introduction 99

4.2. Synoptic scale meteorology from satellite and reanalysis data 100

- 4.3. Local meteorology from Rayleigh lidar 104
- 4.4. High resolution data from CONE 118
  - 4.4.1. Temperature and stability 118
  - 4.4.2. Small-scale fluctuations 120
  - 4.4.3. Characterization of turbulence 126
- 4.5. Evidence of wave breaking. 128
- 4.6. Summary and conclusions... 132

Chapter 5 Summary and Conclusions... 133

References.. 139

List of Figures

Page

Figure 1.1. Conditions in the Arctic middle atmosphere for quiet winters (left) and Distributed winters (right) 2

Figure 1.2. Data from the FTS onboard ACE showing NO_X for the winters of 2003-2004 (top), 2004-2005 (middle), and 2005-2006 (bottom) from January through March in altitude.......... 8

Figure 1.3. Data from MIPAS onboard Envisat showing NO_X in the middle atmosphere for the 2003-2004 winter form October through March in pressure altitudes.......... 9

Figure 1.4. 50-day back trajectories from WACCM over the Northern Hemisphere in pressure altitudes.......... 12

Figure 1.5. Results of tracer experiments in HAMMONIA 13

Figure 1.6. Existing measurements of turbulent parameters in the middle atmosphere16

Figure 2.1. Histogram of Rayleigh lidar observations at Chantanika, Alaska from November 1997 through April 2014 24

Figure 2.2. Calculated buoyancy periods for 152 nights of Rayleigh lidar study averaged over 40 km to 50 km in day of year. Solid squares are monthly average buoyancy periods 28

Figure 2.3. Gravity wave activity averaged over the 40-50 km altitude region as a function of day of year 29

Figure 2.4. 3-D structure of the stratospheric vortex and anticyclones for four days in January-February 2009 32

Figure 2.5. MERRA Horizontal wind speeds in false color over Alaska in January and February 2009 at 350 hPa (upper panels) and 7 hPa (lower panels 34

Figure 2.6. MERRA ΔNBE in false color over Alaska in January and February 2009 at 350 hPa (upper panels) and 7 hPa (lower panels) 35

Figure 2.7. Rayleigh lidar temperature profiles for the seven nights of Rayleigh lidar data in January-February 2009. 36

Figure 2.8. Specific potential energy for the seven nights of Rayleigh lidar data in January-February 2009 in day of year 38

Figure 2.9. MERRA wind profiles over (top) and RMS winds speed in 800 km radius circle around (bottom) Poker Flat Research Range for the seven nights of Rayleigh lidar data in January-February 2009 39

Figure 2.10. MERRA derived ΔNBE profiles over the 800 km radius circle centered on Poker Flat Research Range for the seven nights of Rayleigh lidar data in January-February 2009 41

Figure 2.11. Spearman correlations of specific potential energy average over 40 km to 50 km and horizontal wind speed over Poker Flat Research Range in altitude 42

Figure 2.12. Example scatter plot of specific potential energy and horizontal wind speed at 10 hPa 44

Figure 2.13. Wintertime averaged values of specific potential energy 46

Figure 2.14. Wintertime median horizontal wind over Poker Flat Research Range 47

Figure 2.15. Spearman correlations of specific potential energy average over 40 km to 50 km and ΔNBE around Poker Flat Research Range in altitude 48

Figure 3.1. The CONE instrument 53

Figure 3.2. Photo of MTeX Payload taken at NASA Wallops Flight Facility during system integration and testing 55

Figure 3.3. Example of electrometer (top) and emission (middle) current from the flight of 46.009 and their ratio (bottom) showing raw relative density values 57

Figure 3.4. Example of CONE pressure calibration data (left) and calibration curves (right) for CONE senor #2 and CONE electronics #2 59

Figure 3.5. Example of iterative method used to make the CONE data continuous over range changes 60

Figure 3.6. The density profile for the upleg of 46.009 of the MTeX investigation........ 67

Figure 3.7. Ram corrected ratios for the MTeX investigation 70

Figure 3.8. Calculated temperature (top) and buoyancy frequency squared (bottom) from the gain-corrected CONE data for the upleg of 46.009 71

Figure 3.9. An example of raw CONE ratioed data from the upleg in 46.009 in a nonturbuent region (top) and a turbulent region (bottom)... 73

Figure 3.10. Relative density fluctuations for the same data as shown in Figure 3.9 ... 75

Figure 3.11. Relative density fluctuations filtered between 3 and 20 Hz used to find RMS density fluctuations for the same data in Figures 3.9 and 3.10 77

Figure 3.12. Power Spectra in frequency of the same altitudes from Figures 3.9 with turbulent fitting shown in the bottom panel where turbulence was found. 84

Figure 3.13. Schematic diagram of the new dual-channel Rayleigh lidar system at PFRR 86

Figure 3.14. Lidar signal profiles for data taken on 25-26 January 2015 for the MTeX investigation 89

Figure 3.15. Plot of high altitude channel signal (RH) and low altitude channel signal (RL) on the night of 25-26 January 2015.. 93

Figure 3.16. Nightly temperature profile for 25-26 January 2015 measured by the Rayleigh lidar 95

Figure 4.1. SABER derived geopotential perturbations for 26 January 2015 101

Figure 4.2. Gradient winds as calculated by SABER data on the night of 25-26 January 2015 (left) and zonal wind speed from MERRA reanalysis for 6 UT 26 January 2015 over Chantanika, Alaska (right) 103

Figure 4.3. ΔNBE in altitude over PFRR for the MTeX investigation 105

Figure 4.4. Nightly averaged lidar, 120-minute lidar centered on MTeX rocket launch times, MSIS and SPARC temperature profiles for 25-26 January 2015...................... 107

Figure 4.5. False color temperature plot on the night of 25-26 January 2015 109

Figure 4.6. Temporal evolution of peak altitude (first, top), amplitude (second), topside lapse rate (third), and depth (fourth, bottom) for the upper MIL in red and the lower MIL in green. 110

Figure 4.7. Gravity waves as seen in the Rayleigh lidar density perturbations on the night of 25-26 January 2015 113

Figure 4.8. Temperature (left) and buoyancy frequency (right) profiles from CONE instruments.......... 119

Figure 4.9. Final power spectra from the CONE data for 25-26 January 2015.......... 121

Figure 4.10. RMS density fluctuation (left) and RMS vertical displacement (right) with temperature profiles on 25-26 January 2015.......... 123

Figure 4.11. RMS density fluctuations versus the buoyancy frequency squared for all three analyzed legs (top) and RMS vertical displacement versus the buoyancy frequency squared for all three analyzed legs (bottom). 125

Figure 4.12. Energy dissipation rate (left) and inner scale (right) with error bars and temperature profiles on 25-26 January 2015.......... 127

Figure 4.13. Energy dissipation rate versus buoyancy frequency squared and location in the MIL 129

Figure 4.14. Sodium densities (top) and potential temperatures (bottom) in time on 25-26 January 2015 131

Figure 5.1. Updated energy dissipation rates (top) and eddy diffusion coefficients (bottom) with values found from the MTeX investigation.......... 136

List of Tables

Page

Table 3.1: Summary of MTeX Flights 55

Table 3.2: CONE normalized relative gain from pressure chamber calibration[1]........ 62

Table 3.3: CONE normalized relative gain from pressure chamber calibration[1]........ 62

Table 3.4: CONE normalized relative gain from inflight calibration. 65

Table 3.5: CONE background signal from inflight calibration. 65

Table 3.6: Rayleigh Lidar Performance. 91

Table 4.1: Average characteristics of MILs at PFRR on 25-26 January 2015 111

Table 4.2: Gravity wave activity at PFRR on 25-26 January 2015[1] 114

Table 4.3 Characteristics of Monochromatic Gravity Waves at PFRR on 25-26 January 2015. 117

Acknowledgements

First I would like to thank my advisor, Dr. Richard Collins, for opportunity to work with him. I would like to thank him for his guidance and advice he has giving me during my time at the University of Alaska Fairbanks. The experiences and opportunities Dr. Collins has provided me while working with him have been invaluable. I would also like to thank my committee members, Drs. Uma Bhatt, David Newman, and Thomas Weingartner of the University of Alaska Fairbanks and Dr. Gerald Lehmacher of Clemson University. I would like to thank my former advisor Dr. Kenneth Sassen for bringing me up to Alaska and inviting me to study under him during his last few years at the University of Alaska Fairbanks.

I would like to thank both the National Aeronautics and Space Administration (NASA) for funding the Mesosphere-Lower Thermosphere Turbulence Experiment (MTeX) investigation and the National Science Foundation for funding my initial studies.

I would to thanks the faculty of the Department of Atmospheric Sciences for their help in my studies. I want to especially thank Barbara Day for all of her help to both myself personally and the department in general. I would like to thank the faculty of the Departments of Chemistry, Physics, and Oceanography for their teaching and advice. I would like to thank the Coupling Energetics and Dynamics of Atmospheric Regions (CEDAR) working group for funding my attendance of their workshops in 2014 and 2015. I especially would like to thank the staffs at both the Poker Flat Research Range (PFRR) and NASA's Wallops Flight Facility for their support of equipment and facilities used in this study.

I would like to thank the graduate students of the Departments of Atmospheric Sciences, Chemistry, and Geophysics for their discussion on this research and in general. I would like to thank Sean Egan, Christine Waigl, and Robin Wing for our long discussion for math and science over the years. I would like to thank my laboratory mate Jintai Li for his help in all things personal and professional over the years, but in particular for his operating the sodium resonance lidar on the night of the MTeX investigation. I would like to thank Dr. Brentha Thurairajah of Virginia Polytechnic Institute and State University for her help with satellite data and retrieval.

Finally I would like to thank my parents, Pamela Triplett and Roger Triplett, for everything thing they have done and sacrificed for me. Their continued support and love has been a continuous source of strength and motivation for me through all of my studies and life. I would like to thanks my brother, Nathan Triplett, for always being a great example to me since I was young. I would like to thank my sister-in-law, Sarah Triplett, for all of her support of my family and me. I would like to thank my nephew, Theodore Triplett. You might not have been in our lives very long, but you have already help so much without knowing it. I would like to thank my partner Luke Wetzel for all the love and support you have given me over these years. Lastly, I would like to thank all of my family for all they have done for me since I was born.

Chapter 1 Introduction

1.1. The middle atmosphere

The Earth's atmosphere is conventionally described by spheres based on how temperature varies with altitude [Wallace and Hobbs, 2006]. The lowest sphere is known as the troposphere where the temperature decreases with altitude. The location where this decrease stops and forms a minimum is known as the tropopause. The tropopause is generally located at ~10 km. Above the tropopause the temperature increases in region the known as the stratosphere. This increase in temperature is due to the absorption of solar ultraviolet (UV) radiation by ozone. A maximum temperature is reached ~50 km and called the stratopause. Above the stratopause the temperature again decreases with altitude and this region is known as the mesosphere. A temperature minimum, called the mesopause, is found ~85 km and marks the top of the mesosphere. Above the mesopause the temperature rises quickly in the region called the thermosphere where high-frequency solar radiation and energetic particles are absorbed by the atmosphere. This temperature-based model is the atmosphere as presented in introductory undergraduate meteorology textbooks (e.g., Ahrens [2009]). However, the real atmosphere is a balance between radiative and dynamic forcing, where large-scale planetary wave and small-scale gravity waves lead to significant departures from radiative equilibrium and chemical transport (e.g., Andrews et al. [1987]). These waves propagate upward in the atmosphere transporting energy from the lower to the middle and upper atmosphere as they grow with altitude and break (e.g., Sutherland [2010]).

In Figure 1.1 we show the temperature, winds, and wave-forcing in the Arctic middle atmosphere in winter as described in a 50-year simulation by the Whole

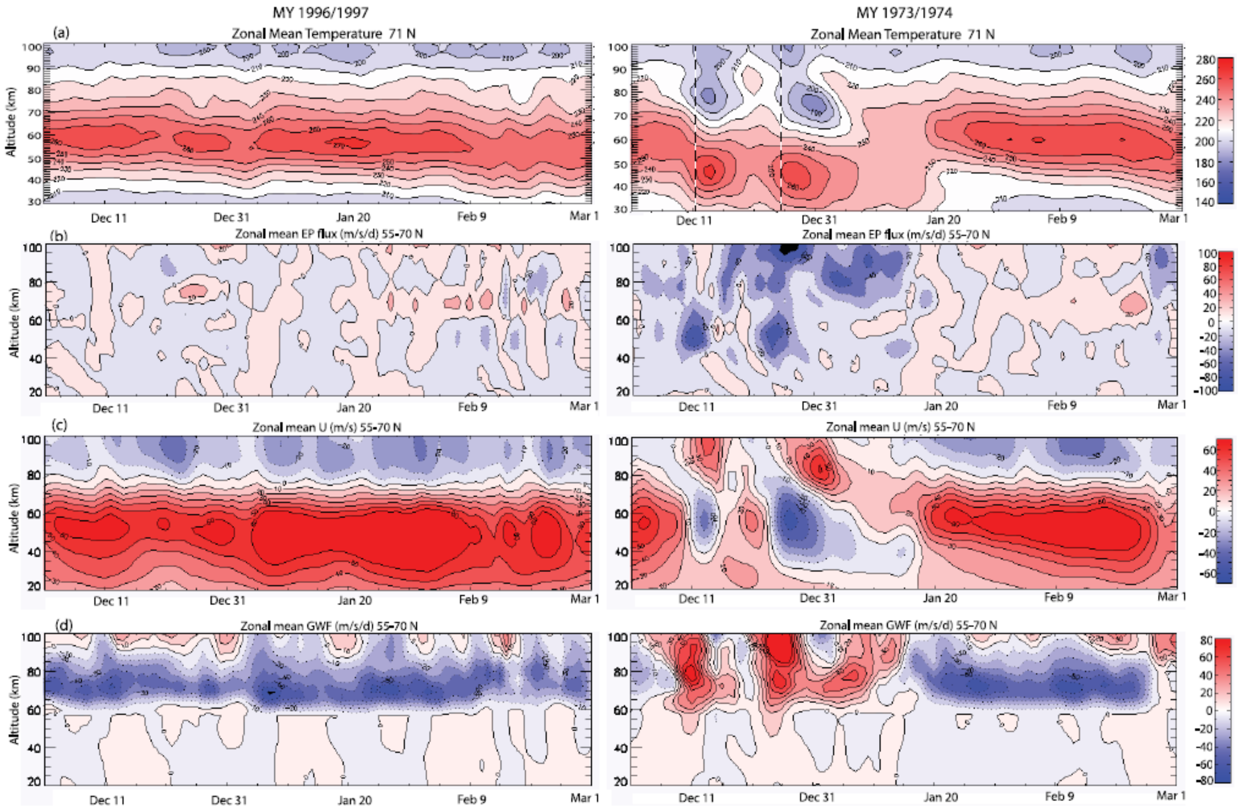

Figure 1.1. Conditions in the Arctic middle atmosphere for quiet winters (left) and Distributed winters (right). All panels are zonal means between December and March. The tops panels are temperature at 71° N. The next panels are planetary wave forcing averaged over 55° N to 70° N. The next panels are zonal mean winds averaged 55° N to 70° N. The bottom panels are gravity wave forcing averaged over 55° N to 70° N. All are functions of time and altitude. Taken from Chandran et al. [2011].

Atmosphere Community Climate Model (WACCM) [Chandran et al., 2011]. WACCM is a general circulation model that extends all the way from the Earth's surface to the lower thermosphere. WACCM is derived from the Community Atmosphere Model (CAM3) and is a fully-coupled chemistry climate model (e.g., Garcia et al. [2007] and references therein). The middle atmosphere is composed of the stratosphere, mesosphere, and lower-thermosphere and stretches between 10 and 100 km. Figure 1.1 is composed of two sets of four panels: model year 1996-1997 (left) and model year 1973-1974 (right). We first discuss model year 1996-1997. In the upmost panel we see the zonally averaged temperature at 71° N from December to March. This temperature plot shows a well-defined stratosphere and mesosphere with the stratopause at 60 km throughout the winter. The next panel shows the forcing by planetary waves averaged over 55° N to 70°N. There is no significant planetary wave activity in this winter. The next panel shows the zonally averaged winds over 55° N to 70° N. They are persistently eastward in the stratosphere and reverse westward in the mesosphere. This reversal is not expected from geostrophic balance. The temperature gradients in the middle atmosphere would lead to an eastward jet that steadily strengthens with altitude. The lowest panel shows the forcing by gravity waves. It is westward in the mesosphere. This westward forcing is the cause of the reversal of the jet in the mesosphere. The forcing arises when the eastwardly propagating gravity waves are removed through Doppler shifting by the eastward winds in the stratosphere (e.g., Cushman-Roisin and Beckers [2011]). The resulted westward propagating gravity waves break in the mesosphere (e.g., Houghton [1978]; Fritts and Alexander [2003]). This wave-breaking results in deposition of energy and momentum and the resultant westward forcing reverses the zonal winds. Globally, this small-scale wave breaking causes a pole-to-pole circulation cell with upwelling over the summer pole and downwelling over the winter pole. This downwelling also results in adiabatic heating that reinforces the wintertime stratopause during the long polar night [Hitchman et al., 1989]. This model winter represents a quiet winter where the characteristics of the stratopause and the zonal jet are undisturbed and planetary wave activity is low.

We now discuss model year 1973-1974 in the right panels of Figure 1.1. This model winter of 1973-1974 reproduces a winter with two SSWs, one on the 11 December and one on 26 December. In the upmost panel of temperature we see that the stratopause is not persistent through the winter. This panel shows a stratopause that falls in altitude and warms at the beginning and end of December and disappears for two weeks in January. Above the lowered stratopause we see a cooling in the mesosphere. The next panel shows the forcing by planetary waves that is significant in this winter. The periods of strong westward forcing coincide with the lowering and warming of the stratopause and cooling of the lower mesosphere. The next panel shows the zonally average winds that are no longer persistently eastward in the stratosphere and westward in the mesosphere. This panel shows a reversal of the eastward jet to a westward jet in the stratosphere when the stratopause is lower and warmer. This westward forcing causes a poleward flow and downwelling in the stratosphere at the altitude of the planetary wave breaking [Matsuno, 1970]. The downwelling results in adiabatic heating of the air and a lowering of the stratopause. This pattern of behavior in temperature and winds is consistent with the planetary wave forcing and a sudden stratospheric warming (SSW) (e.g., Scherhag, [1952]; Matsuno, [1971]; Labitzke and van Loon, [1999]). The model also shows that an eastward jet forms in the mesosphere at these times. The lowest panel shows the forcing by gravity waves is eastward in the mesosphere during the period of the zonal wind reversal. The planetary wave-forcing causes a reversal in the mean stratospheric winds from eastward to westward. The westward jet removes the westwardly propagating gravity waves in the stratosphere. The eastwardly propagating gravity waves propagate into the mesosphere and break and set up an eastward jet in the mesosphere. The zonal jet moves downward over a period of three weeks as the circulation is restored to the quite wintertime circulation.

The SSW events in Figure 1.1 represent major disturbances of the Arctic atmosphere and are characterized as major SSWs. The World Meteorological Organization defines a major SSW as one that leads to a reversal of the zonal mean wind at 60° of latitude and 10 hPa, and a positive poleward temperature gradient from 60° latitude to the pole, at or below 10 hPa. In a minor warming the temperature gradient reverses over a range of altitude below 10 hPa, but the zonal wind at 10 hPa does not. WACCM reproduces the character of SSWs as observed by satellites and reanalysis [Chandran et al., 2014]. Over the 34 winters from 1979-1980 through 2012-2013 major SSWs have occurred in 16 of the 34 winters, or 47% of the time and minor SSWs have occurred in 15 of the 34 winters, or 44% of the time [Chandran et al., 2014]. Thus disturbed winters (DW) represent 91% of Arctic winters while quite winters (QW) represent only 9% of Arctic winters. In contrast there has only been one major SSW in Antarctica over this period [Allen et al., 2003; Baldwin et al., 2003].

The two model years described above show how the dynamics of large-scale planetary waves and small-scale gravity waves both affect and are affected by the mean conditions of the atmosphere. We see that in both QW and DW wave activity is an important part of the circulation. We also see that understanding the large-scale condition of the atmosphere is necessary for understanding the gravity wave activity.

1.2. Vertical transport in the middle atmosphere

Gravity wave breaking is not just important in the forcing of the mean flow, breaking waves are also the energy source of atmospheric turbulence (e.g., Andrews et al. [1987]; Fritts and Alexander [2003]). WACCM, like other general circulation models, properly resolves the large-scale processes that occur during both QW and DW. However, the small-scale gravity wave forcing, and thus turbulence, is too small for WACCM to resolve and has to be parameterized. These parameterizations can have a large effect on model-based investigations of small-scale motions. This is particularly important in the vertical transport of chemical species.

Vertical transport in the atmosphere has three main mechanisms: advection, eddy diffusion, and molecular diffusion. Advection is the bulk motion of air. Eddy diffusion is the motion due to eddies caused by turbulence. Molecular diffusion is the random kinetic motion of atoms and molecules. One family of chemicals that is vertical transported in the middle atmosphere is odd nitrogen. During solar events there is precipitation of energetic particles into the thermosphere. These energetic particles dissociate nitrogen molecules (N_2) resulting in the formation of atomic nitrogen (N) and the eventual formation of nitrogen oxide (NO) and nitrogen dioxide (NO_2) [Crutzen et al., 1975; Brasseur and Solomon, 1995; Wayne, 2000]. Vertical motion of NO_X ($NO+NO_2$) during Arctic winter has been observed by satellites as shown in Figures 1.2 and 1.3. Figure 1.2 shows three different winters, January through March, from the Fourier Transform Spectrometer (FTS) onboard the Atmospheric Chemistry Experiment (ACE) satellite [Bernath et al., 2005; Randall et al., 2006]. The upper panel is winter 2003-2004 when there was high solar activity and significant precipitation of energetic particles into the thermosphere. Starting in February, motion of NO_X is seen down to 40 km. The middle panel shows winter 2004-2005. In this winter, no NO_X is transported from the thermosphere. The lower panel is winter 2005-2006. This winter had very low solar activity. Starting in February, transport of NO_X is seen down to 50 km. These three winters demonstrate that solar activity alone is not responsible for the transport of NO_X and that meteorological conditions must play a significant role in the transport. Figure 1.3 shows the same winter 2003-2004 as the upper panel of Figure 1.2, but from the Michelson Interferometer for Passive Atmospheric Sounding (MIPAS) onboard the Environmental Satellite (Envisat). [Fischer and Oelhaf, 1996; López-Puertas et al., 2006]. Here we see NO_2, a component of NO_X, from October through March. In the Arctic middle atmosphere, again we see downward transport of NO_X from the thermosphere into the stratosphere. This transport is a problem for ozone in the stratosphere [Allen et al., 2003]. NO_X is long-lived and aids in ozone destruction [Funke et al., 2007; Sinnhuber et al., 2014].

Destruction of ozone by NOx is not the primary mechanism of ozone depletion. The primary method of ozone depletion is the catalytic destruction of ozone by halogens and the formation of the “ozone hole”. The “ozone hole” is the springtime depletion of ozone that occurs over Antarctica and was first observed in the 1980’s [Farman et al., 1985]. In Antarctica, the robust stratospheric vortex results in widespread lower

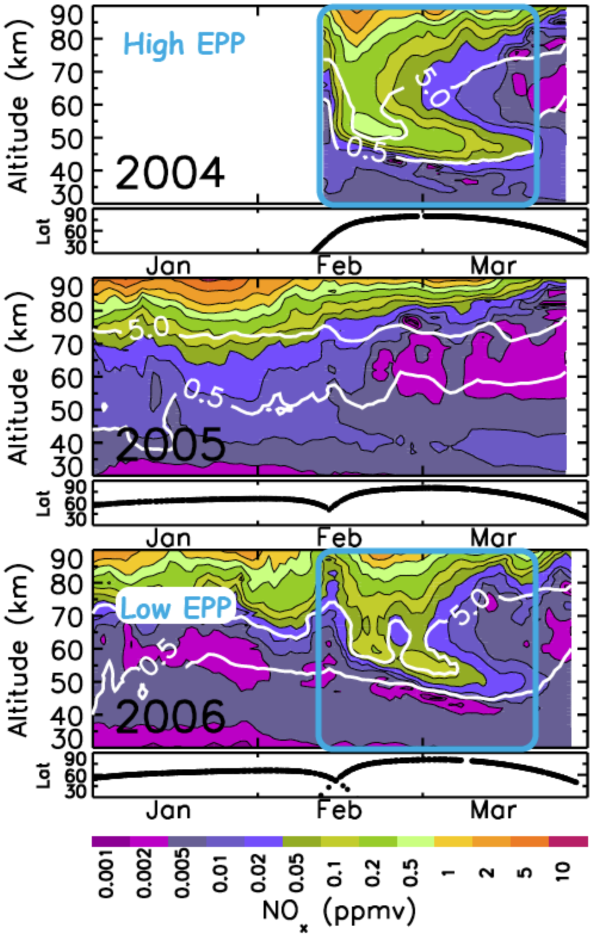

Figure 1.2. Data from the FTS onboard ACE showing NO_X for the winters of 2003-2004 (top), 2004-2005 (middle), and 2005-2006 (bottom) from January through March in altitude. Adapted from Randall et al. [2006].

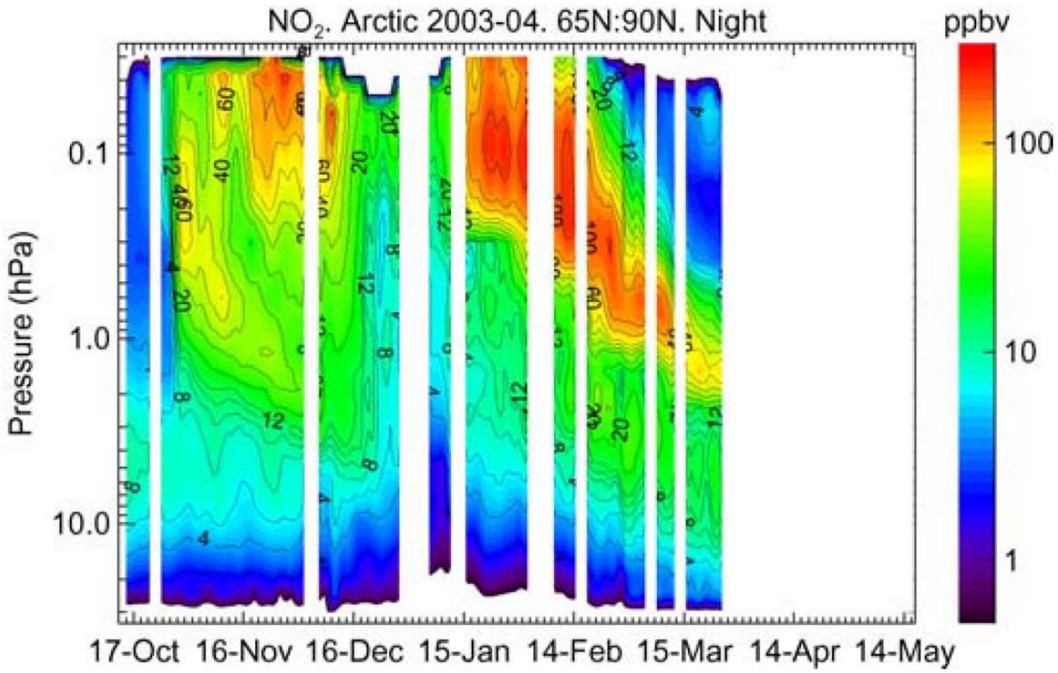

Figure 1.3. Data from MIPAS onboard Envisat showing NO_X in the middle atmosphere for the 2003-2004 winter form October through March in pressure altitudes. Adapted from López-Puertas et al. [2006].

temperatures, formation of polar stratospheric clouds, buildup of chemically active halogen species, and the springtime catalytic destruction of ozone (see review by Solomon [1999] and references therein). In contrast, as we have seen, the Arctic circulation is more disturbed and the vortex is less robust, so that while there are regions and periods when PSCs can form in the Arctic, the conditions for an "ozone hole" are not usually met. In fact, only in the winter of 2010-2011 did meteorological conditions result in a robust Arctic stratospheric vortex with cold temperatures that resulted in the destruction of ozone at levels similar to those seen in Antarctica [Manney et al., 2011]. While there is less ozone depletion in the Arctic than the Antarctic, ozone-poor air can travel over more densely populated regions in the northern hemisphere than the southern hemisphere, and thus pose more of a threat to human health. For discussion of health factors associated with ozone depletion see Chipperfield et al. [2015] and references therein.

The difference between the meteorology associated with these two methods of ozone destruction leads to the following idea. The transport of thermospheric NOx into the stratosphere occurs when the circulation recovers during a disturbed winter when the stratospheric jet and vortex are disrupted (common in the Arctic and rare in the Antarctic). The catalytic destruction of ozone occurs in quiet winters when the jet and vortex are undisturbed and there is widespread formation of PSCs (common in the Antarctic and rare in the Arctic). Thus the transport of thermospheric NOx downward into the stratosphere has a more significant role in the Arctic. With this observation and the knowledge that the ozone hole can move over populated areas, we need to understand how dynamic motions in the middle atmosphere could transport ozone destroying chemicals, such as NOx, to the stratosphere. Prompted by the satellite observations of NOx two studies have used contemporary circulation models to investigate this vertical transport.

1.3. Model studies of NOx transport in the middle atmosphere

Both Smith et al. [2011] (S11) and Meraner and Schmidt [2016] (MS16) investigated vertical transport from the thermosphere into the middle atmosphere in whole-atmosphere models. S11 used WACCM while MS16 used the HAmburg MOdel of Neutral and Ionized Atmosphere (HAMMONIA). S11 reviewed 50-day back trajectories within WACCM to see where air come form in the high latitude mesosphere. Their results are plotted in Figure 1.4. From Figure 1.4 we can see that these WACCM trajectories primarily show motion from the low latitude mesosphere to the high latitude mesosphere, but trajectories from the high latitude thermosphere are few. Thus S11 concluded that advection could not explain the transport from the polar thermosphere to the polar mesosphere. The authors suggested that the downward transport of NOx could result from turbulent transport downward over the pole, and entrainment into the mesospheric advection. However, they found that the turbulence in the model was not strong enough transport the NOx downward [Smith et al., 2011].

The MS16 study turned the three different vertical motion mechanisms (i.e., advection, eddy diffusion, molecular diffusion) on and off to see how each affected a passive tracer within HAMMONIA. Their results for the SSW in January 2009 are in Figure 1.5. MS16 injected a passive tracer into the lower thermosphere at ~ 95 km. The

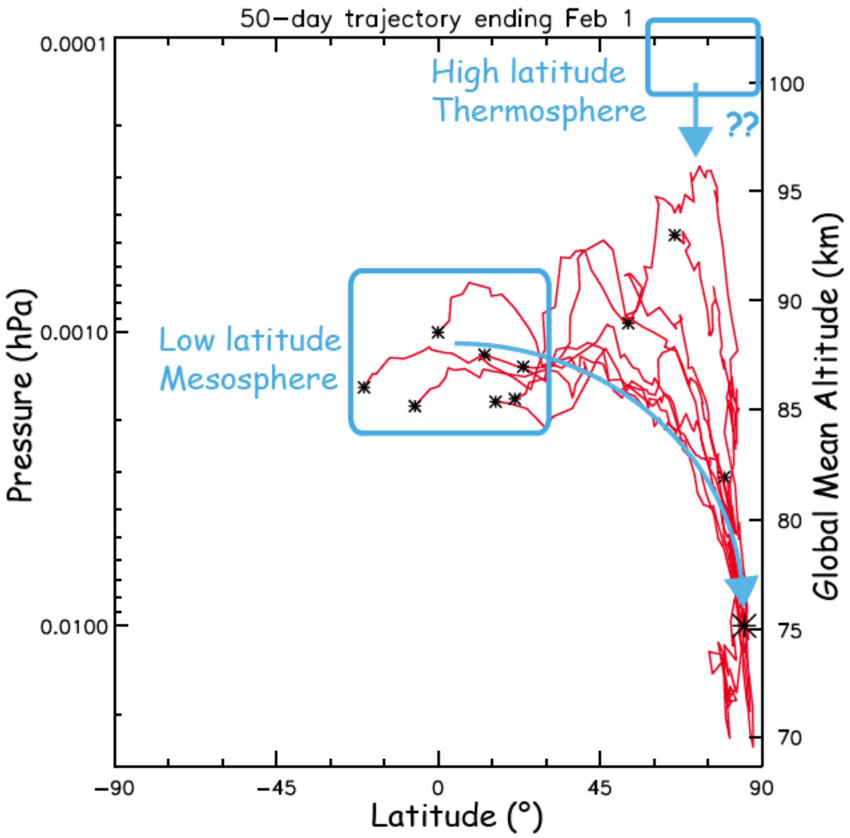

Figure 1.4. 50-day back trajectories from WACCM over the Northern Hemisphere in pressure altitudes. Adapted from Smith et al. [2011]

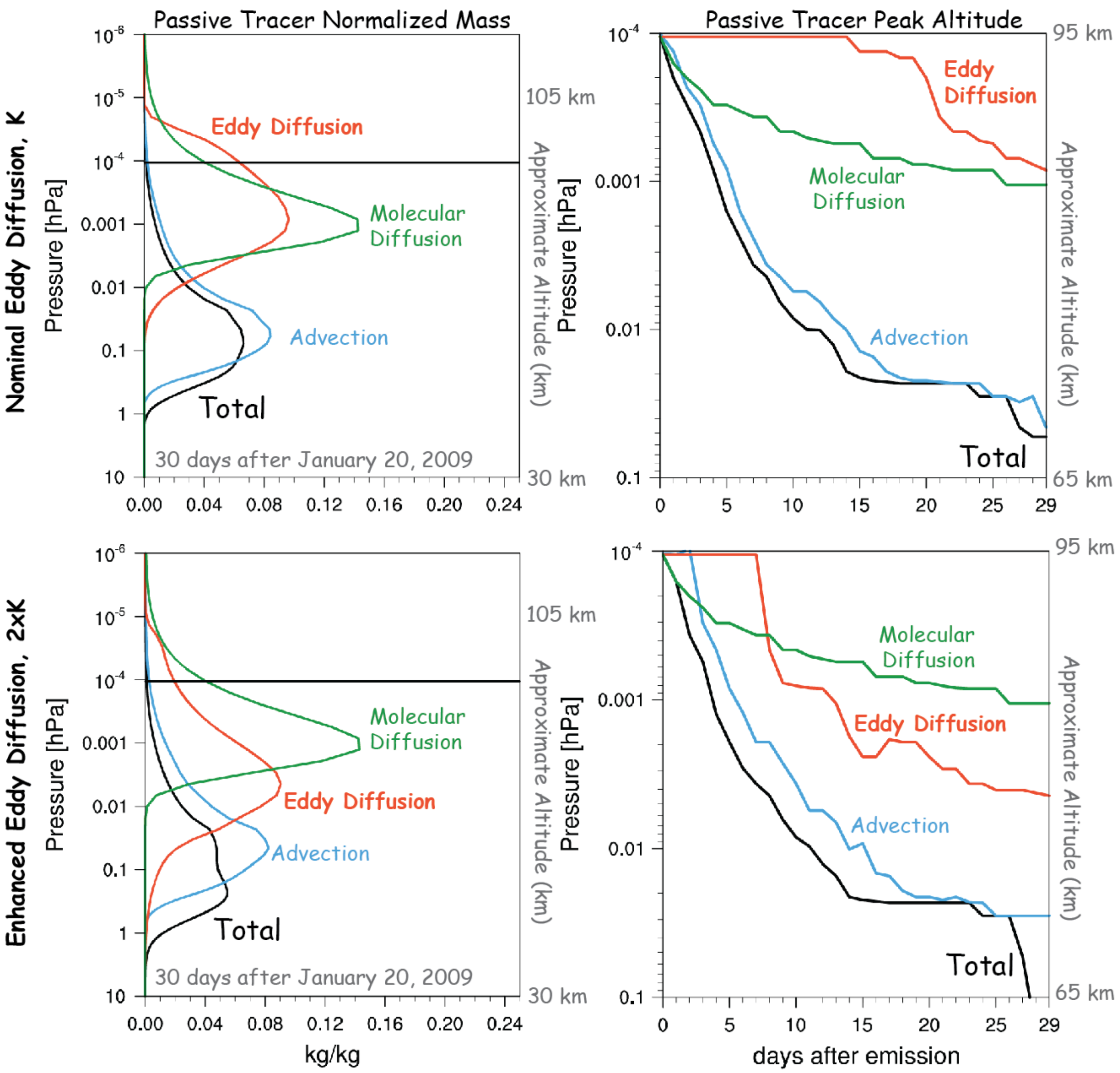

Figure 1.5. Results of tracer experiments in HAMMONIA. The left panels show the location in altitude of the normalized tracer masses after 30 days. The right panels show the location of the peak of the tracer in altitude during 30 days after emission. The top panels represent nominal eddy diffusion coefficient of HAMMONIA while the bottom panels represent a doubling of the eddy diffusion coefficient. Adapted from Meraner and Schmidt [2016].

left panels of Figure 1.5 show the vertical distribution of the normalized tracer mass after 30 days. The right panels of Figure 1.5 show the location of the peak of the tracer in days after the release of the tracer. The upper left panel shows that advection alone moves the majority of the tracer from the thermosphere into the stratosphere. Both the molecular and eddy diffusions result in weaker vertical transport than the advection. The upper right panel shows that only advection is strong enough to move the peak location of the tracer downward into the stratosphere. The lower panels of Figure 1.5 show the results of an HAMMONIA simulation where the eddy diffusion coefficient has been doubled. The lower left panel still shows that advection is still the most important mechanism, however, now the eddy diffusion now moves the tracer lower than it did previously. The lower right panel shows that the eddy diffusion has moved the peak of the tracer further down than previously. MS16 investigated this doubling of the eddy diffusion because the authors recognized that values of eddy diffusion within HAMMONIA differ from those of other models and observations. Figure 1.5 shows that this study found that advection was the most important mechanism for vertical transport the doubling of eddy diffusion has a large effect on the tracer transport [Meraner and Schmidt, 2016].

These two studies find two very different things. S11 finds that advection fails as the mechanism of transport from the high latitude thermosphere to the mesosphere while MS16 found that advection can explain the transport. However, what is important for our study is the fact that both papers show that eddy diffusion, and therefore turbulent motions, are not well understood, and there is significant uncertainty in the contribution of eddy transport. Our study aims to better understand turbulent parameters in the middle atmosphere in the winter so that more accurate values can be used in models.

1.4. Existing turbulent measurements

Measurements of turbulence in the middle atmosphere have been made since the 1990s [Lehmacher and Lübken, 1995 (L&L95); Lübken, 1997 (L97); Bishop et al., 2004 (Betal04); Lehmacher et al., 2006 (Letal06); Collins et al., 2011 (Cetal11); Lehmacher et al., 2011 (Letal11)]. We plot the values from these studies in Figure 1.6. The L97 values are averages based on in-situ measurements of turbulence from multiple rocket missions. The Cetal11 value is calculated from the motion of the mesospheric sodium layer measured with a resonance lidar on one night. All other data sets are based on individual rocket-based measurements of turbulent fluctuations or expansion of chemical tracers. The top panel of Figure 1.6 shows the values of the energy dissipation rate, ε. The energy dissipation rate indicates how much heating is caused by the turbulence in a region. For example, a dissipation rate of 1 W/kg is equivalent to a heating of 86 K/day. The bottom panel of Figure 1.6 shows the values of the eddy diffusion coefficient, K. The eddy diffusion coefficient indicates how much mixing is caused by the turbulence. The relationship between ε and K is given as,

$$\varepsilon = \frac{1}{0.81} N^2 K \tag{1.1}$$

where N^2 is the buoyancy frequency square [Weinstock, 1978]. Equation 1.1 tells us when the atmosphere is more stable (i.e., higher N^2) more energy is needed to create a given amount of mixing. Conversely, when the atmosphere is less stable (i.e., lower N^2) less energy is needed to create a given amount of mixing. This shows how meteorological conditions affect turbulence. Figure 1.6 shows that values of ε vary over three orders of

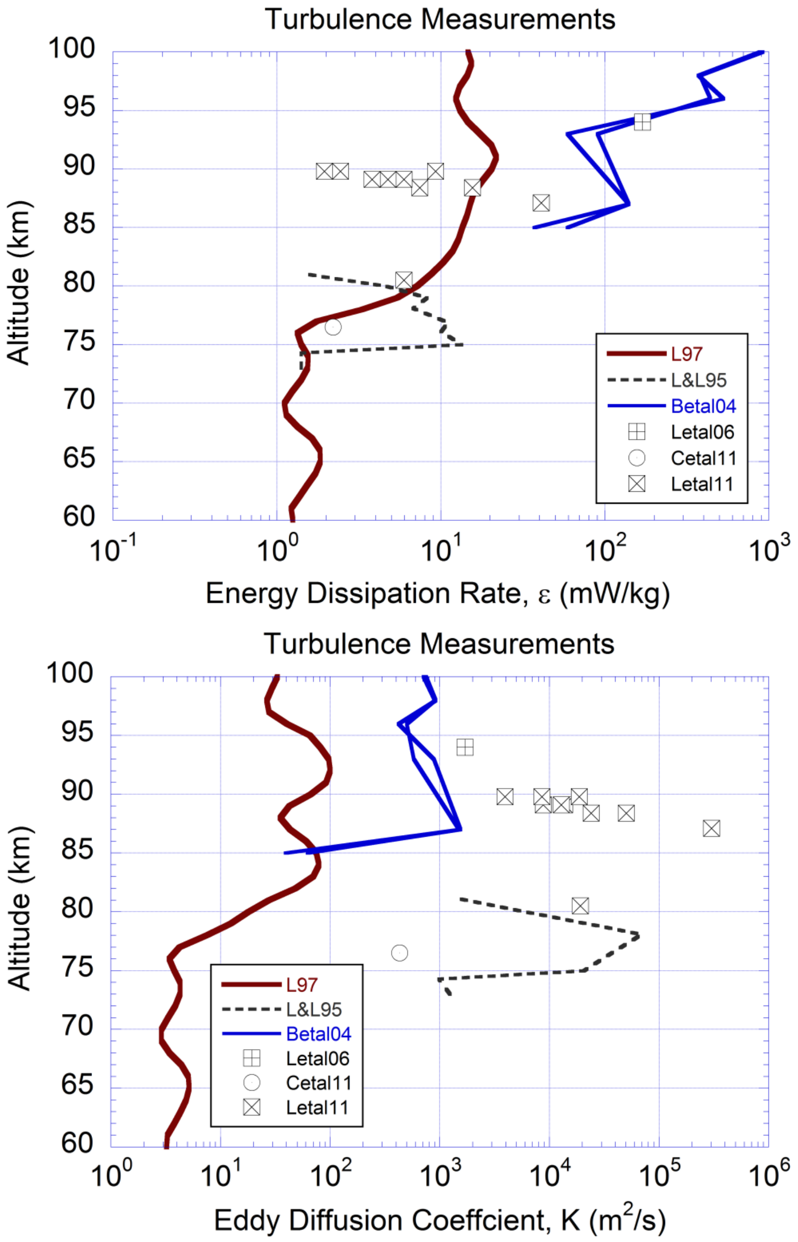

Figure 1.6. Existing measurements of turbulent parameters in the middle atmosphere. The top panel gives the studies' values of the energy dissipation rate, ε. The bottom panel gives the studies' values of the eddy diffusion coefficient, K. Both panels are in altitude.

magnitude while values of K vary over six orders of magnitude. Thus in order to understand the turbulence seen in the middle atmosphere, we have to have an understanding of the atmospheric conditions under which the turbulence occurs. We must study turbulence while we know the atmospheric conditions in order to properly describe the motions seen in the atmosphere. This will allow modelers to better parameterize turbulence and thus be more accurate when they study its effects.

This variation in the measured values of K (i.e., six orders of magnitude in Figure 1.6) also sheds light onto MS16 findings. The value of K used in HAMMONIA from MS16 is 53 m^2/s. This value is typical of the seasonally averaged values reported by L97. With the doubling of K causing such a significant change in the behavior seen in HAMMONIA, a six orders of magnitude change would make eddy diffusion rival the advective motion.

1.5. Scope of this study

In this study I do two things. First, I investigate the gravity wave activity measured over several years at Poker Flat Research Range, PFRR (65°N, 147°W) as representative of Arctic wintertime conditions. Second, I perform a focused study of the atmospheric conditions, gravity wave activity, and turbulent measurements taken with the COmbined measurement of Neutrals and Electrons (CONE) ion gauge during the Mesosphere-Lower Thermosphere Turbulence Experiment (MTeX): a rocket investigation I was a part of in January 2015. Based on these two studies I aim to understand the meteorological controls of gravity wave activity and the generation of turbulence in the wintertime Arctic middle atmosphere.

In Chapter 2 I present a multi-year study of gravity wave activity at Chatanika Alaska. This study is based on my review of the single-channel Rayleigh lidar system at PFRR and its data retrieval methods. I use reanalysis data from the Modern-Era Retrospective analysis for Research and Applications (MERRA) to define the meteorological conditions. I investigate the meteorological control of gravity wave activity through both waveblocking by the winds and wave generation by ageostrophy. These two processes are important during SSWs in the Arctic winter. I presented initial results from this study at the Coupling Energetics and Dynamics of Atmospheric Regions (CEDAR) meetings in summer 2014 and 2015 [Triplett et al., 2014; 2015a]

In Chapter 3 I present the methods and techniques I developed and employed to analyze and interpret the MTeX rocket and lidar measurements. I participated in the MTeX investigation since 2013. I upgraded the Rayleigh lidar to a two-channel system in support of the MTeX investigation. I also participated in the integration and testing of the CONE instrument at NASA Wallops Flight Facility in 2014. During the MTeX investigation in January 2015 I operated the upgraded Rayleigh lidar system and provided and interpreted real-time density and temperature retrievals in support of the launch decision. Since the MTeX launch I have developed independent retrieval methods for the lidar and CONE instruments. I was a co-author of a newsroom article that described the MTeX investigation and reported preliminary results [Collins et al., 2015]. I presented initial analysis and interpretation of the MTeX CONE measurements at the 2015 AGU fall meeting [Triplett et al., 2015b].

In Chapter 4 I present the scientific observations and measurements associated with the MTeX investigation on the night of 25-26 January 2016. I present the meteorology of the middle atmosphere as revealed by the SABER instrument onboard the TIMED satellite. I then present the Rayleigh lidar measurements and the CONE measurements. I analyze the turbulent activity measured by CONE in terms of the local meteorological conditions measured by both CONE and the lidar, and the regional meteorological conditions measured by SABER.

In Chapter 5 I summarize my key findings, present my conclusions, and make recommendations for future work.

Chapter 2 Effects of Wind Filtering and Ageostrophic Generation on Middle Atmosphere Gravity Wave Activity at Chatanika Alaska

2.1. Introduction

Understanding of gravity waves is critical to the study of the middle atmosphere [Houghton, 1978]. How these waves affect the circulation of the stratosphere has been a focus of the Stratospheric Processes and their Role in Climate (SPARC) Gravity Wave Activity [Alexander and Sato, 2015] and the recent DEEPWAVE campaign [Fritts et al., 2016]. Gravity wave sources include orographic generation, convection, and meteorological conditions including wind shears, geostrophic adjustment and wave-wave interaction [Fritts and Alexander, 2003]. Contemporary satellite studies have identified the global distribution of stratospheric gravity wave activity, confirming regional sources associated orographic hotspots (e.g., Andes, Antarctic Peninsula) and convection (e.g., North American Plains in summer) as well as mesoscale hotspots found near prominent orographic features [Hoffmann et al., 2013].

The Arctic wintertime middle atmosphere provides a natural laboratory for understanding the role of gravity waves in the general circulation. When the middle atmosphere is disturbed during a sudden stratospheric warming event (SSW), breaking planetary waves reverse the circulation resulting in blocking of orographic gravity waves while non-orographic waves propagate into the mesosphere and contribute to the recovery of the circulation (e.g., Chandran et al. [2011; 2013; 2014], Limpasuvan et al., [2011], and Ren et al. [2011]). During these events there is significant ageostrophy as the tropospheric and stratospheric jets depart from geostrophic flows. The generation of gravity waves by geostrophic adjustment of an ageostrophic flow returning to the lower geostrophic state and radiating the excess energy as gravity waves has been recognized as a classic problem [Rossby, 1938; Cahn, 1945; Obukhov, 1949]. In the absence of convection during the winter, ageostrophic flow is expected to be a significant source of gravity waves.

We present a new analysis of Rayleigh lidar measurements of gravity wave activity on 152 nights at Poker Flat Research Range (PFRR), Chatanika, Alaska (65°N, 147°W) over 14 years between 1998 and 2014. Previous Rayleigh lidar studies have focused on gravity wave activity measured on 61 nights associated with SSWs over three winters between 2002 and 2005 and two winters during the International Polar Year between 2007 and 2009 [Thurairajah et al., 2010a;b]. Those studies focused on the relationship between the gravity wave activity and the wind. In this study we extend the scope of these earlier studies to investigate the both the role of both the winds and ageostrophic flow in determining the gravity wave activity in the Arctic upper stratosphere and lower mesosphere (40-50 km). This paper is arranged as follows. In Section 2.2 we describe the Rayleigh lidar system at PFRR, the MERRA reanalysis, and the techniques and the methods used to determine and characterize gravity wave activity, winds, and ageostrophy. In Section 2.3 we investigate the relationship between gravity wave activity wind, and ageostrophy during the major SSW in 2009. In Section 2.4 we investigate the correlation between the gravity wave activity and the winds in all years. In Section 2.5 we investigate the relationship between the gravity wave activity and ageostrophy in all years. Finally, in Section 2.6 we present our summary and conclusions.

2.2 Methods and techniques

2.2.1 Rayleigh lidar

The National Institute of Information and Communications (NICT) Rayleigh lidar has been operated at Poker Flat Research Range, Chatanika, Alaska since 1997. Earlier studies of gravity waves at Chatanika have focused on single observations [Collins et al. 2011], observations over several winters [Thurairajah et al., 2010a; b], or observations associated with Mesospheric Inversion Layers [Irving et al., 2014]. Here we draw on observations made on 327 nights under clear sky conditions between 14 November 1997 and 10 April 2014. We limit our attention to the highest quality observations which meet the following criteria; the duration of the observation is greater than five hours, there are no gaps in the observation of more than 30 minutes, the lidar signal does not change by more than 50% between successive raw lidar profiles. We found that 152 observations satisfied these criteria. Of these 152 observations, 81 observations (or 53%) were made during December-January-February (DJF), 46 observations (or 32%) were made during March-April-May (MAM), only two observations (or 1%) were made in June-July-August (JJA), and 23 (or 15%) were made during September-October-November (SON). We plot the monthly distribution of observations in Figure 2.1. The seasonal distribution of observations reflects both the skylight conditions, where observations are made after nautical twilight (-12° solar declination) and the cloudiness, where March is the least cloudy month at Chatanika. There are no observations that satisfy our data quality criteria made during the months of May, June, and July due to the short and bright nights at this high latitude site.

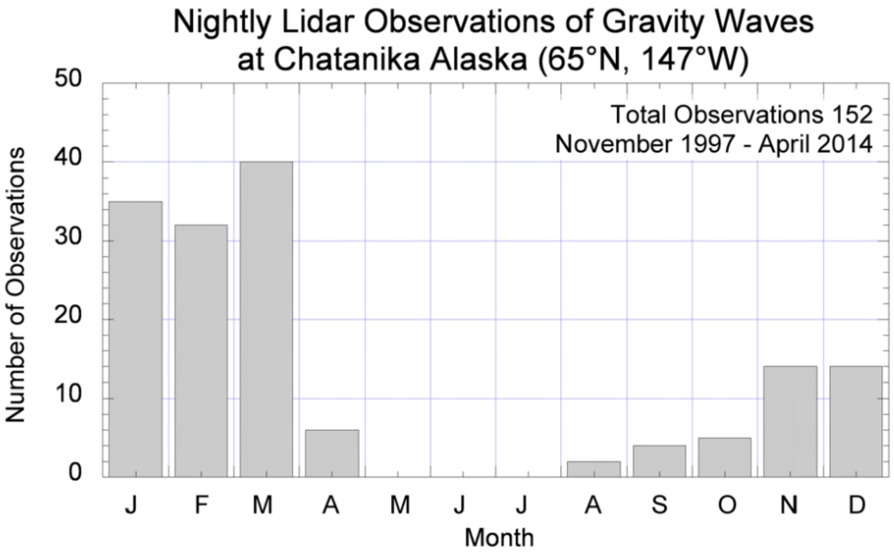

Figure 2.1. Histogram of Rayleigh lidar observations at Chatanika, Alaska from November 1997 through April 2014.

We use the same methods for the retrieval of density and temperature profiles from raw lidar signal profiles as in earlier studies at Chatanika [Thurairajah et al., 2009; 2010a; b, Collins et al., 2011, Irving et al., 2014]. In summary we determine the relative density fluctuations from the sequence of 30-minute density profiles, and the buoyancy frequency from the average temperature profile. We use an initial temperature at 80 km from the Stratospheric Processes and their Role in Climate (SPARC) atlas [SPARC, 2002; Randel et al., 2004]. We remove fluctuations with periods longer than 4 h from the density fluctuations. We determine the average mean square fluctuations over a given altitude (i.e., 40-50 km), the average buoyancy period over the same altitude range, and then determine the corresponding RMS displacement, and specific potential energy (energy per unit mass) using established relationships (e.g., Thurairajah et al. [2010a; b] and Gill [1982]). We report the RMS density fluctuations, the buoyancy period, displacement, and specific potential energy (energy per unit mass). The removal of low-frequency fluctuations has important implications for the values of the potential energy. Without this high-pass filtering, the fluctuations would include contributions from waves with periods up to the length of the observation period, and so include contributions from tides. We have determined the specific potential energies and found that inclusion of periods longer than 4 h increase the specific potential energies by a factor of between 1.3 and 13, with an average value of 4.5.

2.2.2 Meteorological reanalysis

The Modern-Era Retrospective Analysis for Research and Applications (MERRA) reanalysis dataset describes the meteorological conditions in the troposphere, stratosphere and lower-mesosphere since 1980 [Rienecker et al., 2011]. We use MERRA to study the relationships between the gravity wave activity and the mean winds and the ageostrophy. For this study we use the Data Assimilation System 3d analyzed state on pressure (inst6_3d_ana_Np) data set at 06 UT (21 LST) to represent the nighttime conditions corresponding to the lidar observation. This set has spatial resolution of 1/2° x 2/3° and 40 vertical levels set on constant pressure surfaces. We determined the corresponding geometric altitudes using techniques established by Champion et al. [1985].

We investigate the correlation between the gravity wave specific potential energy (energy per unit mass) and the magnitude of the horizontal wind by combining the zonal and meridional components of the wind at each pressure level over Chatanika. We investigate the correlation between the gravity wave specific potential energy and the ageostrophy as characterized by the residual in the Nonlinear Balance Equation (ΔNBE) [Petterssen, 1953; Zhang et al., 2000; 2001]. We calculate ΔNBE using the following equation,

$$\Delta NBE = 2J(u,v) - \beta u + f\zeta - \nabla^2\phi \tag{2.1}$$

$$J(u,v) = \frac{\partial u}{\partial x}\frac{\partial v}{\partial y} - \frac{\partial v}{\partial x}\frac{\partial u}{\partial y} \tag{2.2}$$

where u and v are the zonal and meridional wind, respectively, and ϕ is the geopotential height. J is the Jacobian, β is the meridional derivative of the Coriolis parameter, f is the Coriolis parameter, and ζ is the relative vorticity. We validated our implementation by reproducing ΔNBE for two earlier studies [Hertzog et al., 2001; Zhang et al., 2001]. We then average the ΔNBE at each pressure level over all points within an 800 km radius of Chatanika.

In our correlation study we calculate both the Pearson and Spearmen correlation coefficients [Press et al., 1992]. The Pearson correlation coefficient represents the traditional linear correlation coefficient. The Spearman correlation coefficient is the correlation based on the rank of the data, it does not require the data to have a normal distribution, and it's less susceptible to outliers [Hoffmann et al., 2013].

2.3. Rayleigh lidar measurements of gravity wave activity

We plot the buoyancy period averaged over the 40-50 km altitude range as a function of day of year in Figure 2.2. We plot the data from August through April. The corresponding values of the measured buoyancy periods are plotted in the center panel. The values vary between 256 s and 360 s with an average of 304 s. The values of the buoyancy period show increasing stability in August, September and October. However, from November through March there is significantly more variability in the stability, with the largest range of values found in January with values varying between 267 s and 360 s. We plot the gravity wave activity period averaged over the 40-50 km altitude region as a function of day of year in Figure 2.3. The values of the measured RMS relative density fluctuations are plotted in the top panel. The 152 values vary between 0.13 % and 1.04 % with an average of 0.40 %. (± 0.01 %). The signal-to-noise ratio (SNR) of the measurements varies between 0.27 and 22 with an average value of 4.4 (± 0.3). We also plot the monthly average values of the RMS relative density fluctuations with their standard errors. The monthly average averages show a wintertime maximum extending from November through January. We plot the corresponding values of the RMS

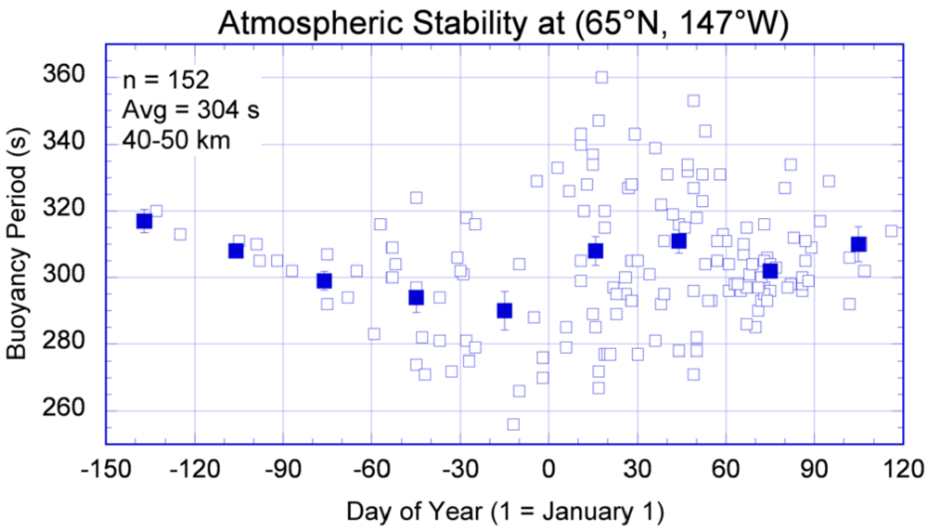

Figure 2.2. Calculated buoyancy periods for 152 nights of Rayleigh lidar study averaged over 40 km to 50 km in day of year. Solid squares are monthly average buoyancy periods.

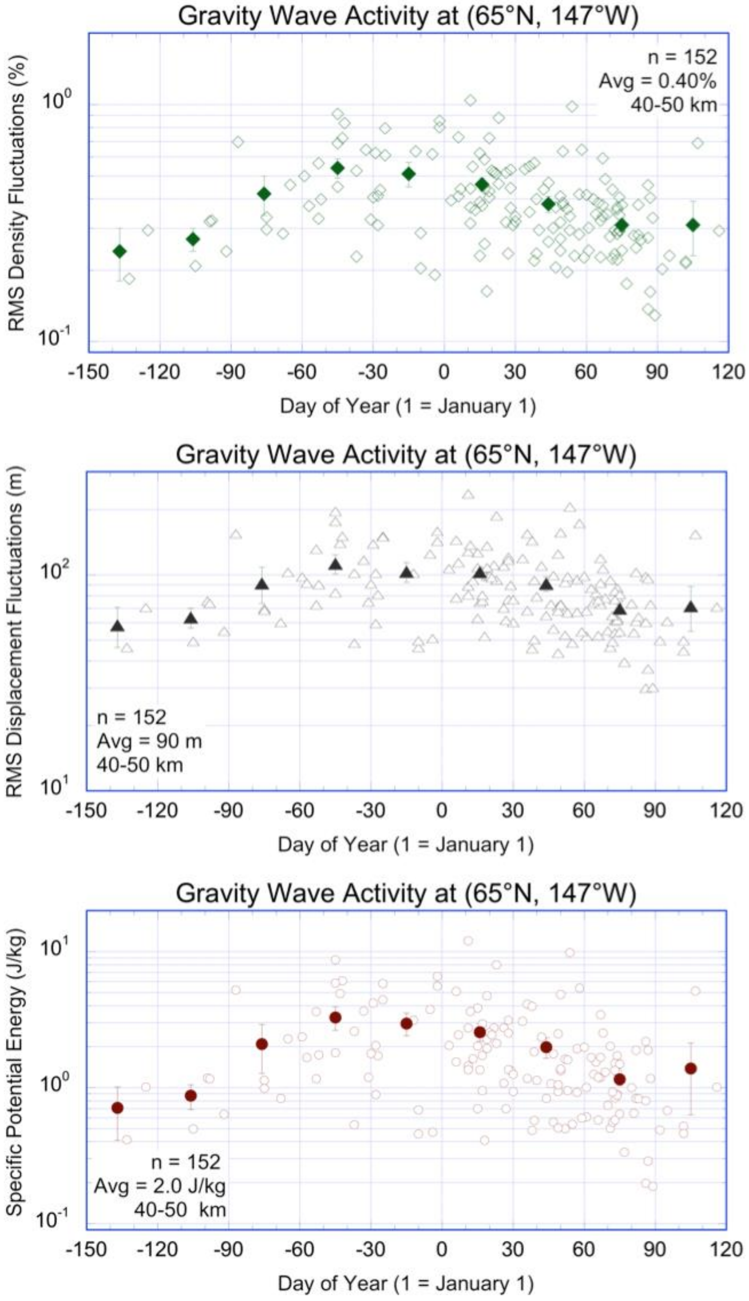

Figure 2.3. Gravity wave activity averaged over the 40-50 km altitude region as a function of day of year. The top panel are RMS density fluctuations with average values as solid diamonds. The middle panel are RMS displacement fluctuations with average values as solid triangles. The bottom panel are specific potential energies with average values as solid circles.

displacement fluctuations in the middle panel. The 152 values vary between 29.9 m and 237 m with an average value of 89.5 m (± 3.1 m). We plot the specific potential energies in the lowest panel. The values vary between 0.41 and 12 J/kg with an average value of 2.6 J (± 0.2 J). The maximum nightly values in all quantities are found in January and the lowest values in March. The night-to-night variability is greatest in January and values of the specific potential energy vary by a factor of 29, reflecting both the variability in the RMS relative density fluctuations and the buoyancy period. The maximum monthly average in all three quantities of gravity wave activity is found in November and the minimum monthly value is found in August. The maximum in November represents a seasonal maximum in wave activity, as during November, December and January the monthly mean values of all quantities differ by less than their standard errors.

To better understand how the waves are propagating with altitude we calculate the ratio of the specific potential energy calculated over the 45-55 km to that over the 40-50 km altitude ranges. We take the ratio of the specific potential energies and multiply it by the corresponding ratio of the atmospheric densities as measured by the lidar, yielding the ratio of the potential energy density. For conservative waves that are propagating freely the energy ratio is 1, for waves that are losing energy the energy ratio is less than 1, and for waves that are gaining energy the energy ratio is greater than 1. We limit our attention to those nights where the SNR of the RMS relative density fluctuations in the 40-50 km altitude range is greater than 1 yielding 145 nights of observations. The ratio of the specific potential energies varies between 0.31 and 5.1 with an average value of 1.51 (± 0.06), corresponding to a growth length of 12 km. The ratio of the densities varies between 0.44 and 0.53 with an average value of 0.49 (± 0.002), corresponding to a scale height of 7 km. The energy ratio varies between 0.15 and 2.6, with an average value of 0.74 (± 0.03 m). On 119 nights the ratio is less than 1 while on 26 nights the ratio is greater than 1. This indicates that on average the waves are losing energy with altitude with a decay length of 17 km.

2.4. The 2009 Sudden Stratospheric Warming

During the 2008-2009 winter, a major sudden stratospheric warming (SSW) occurred during the third week of January 2009 when the Aleutian high strengthened and the vortex split in two. In Figure 2.4 we show the 3-D structure of the stratospheric vortex and anticyclones in January and February 2009. The 3-D structure was calculated using the United Kingdom Meteorological Office (MetO) global analyses data to calculate the characteristics of the vortices [Harvey et al., 2002]. Harvey et al. [2002] identify anticyclones and vortex in terms of evolving three-dimensional air masses, based on stream function analysis. The plots Figure 2.4 were originally created for an International Polar Year study of the circulation of the Arctic middle atmosphere [Thurairajah et al., 2010b]. In Figure 2.4 (upper left panel) we show the nearly pole centered, undisturbed polar vortex on 6 January 2009. The vortex first split in the upper stratosphere around 19-20 January and continued to split downward to the mid-stratosphere (800 K, ~30 km, ~10 hPa) on 22 January (Figure 2.4, upper right panel). The vortex continued to split and was split through the entire stratosphere by the 29 January (Figure 2.4, lower left panel). The vortex remained split for almost three weeks until early February when the upper stratospheric vortex recovered with colder temperatures. By the second week of February the upper stratospheric vortex had completely recovered and strengthened

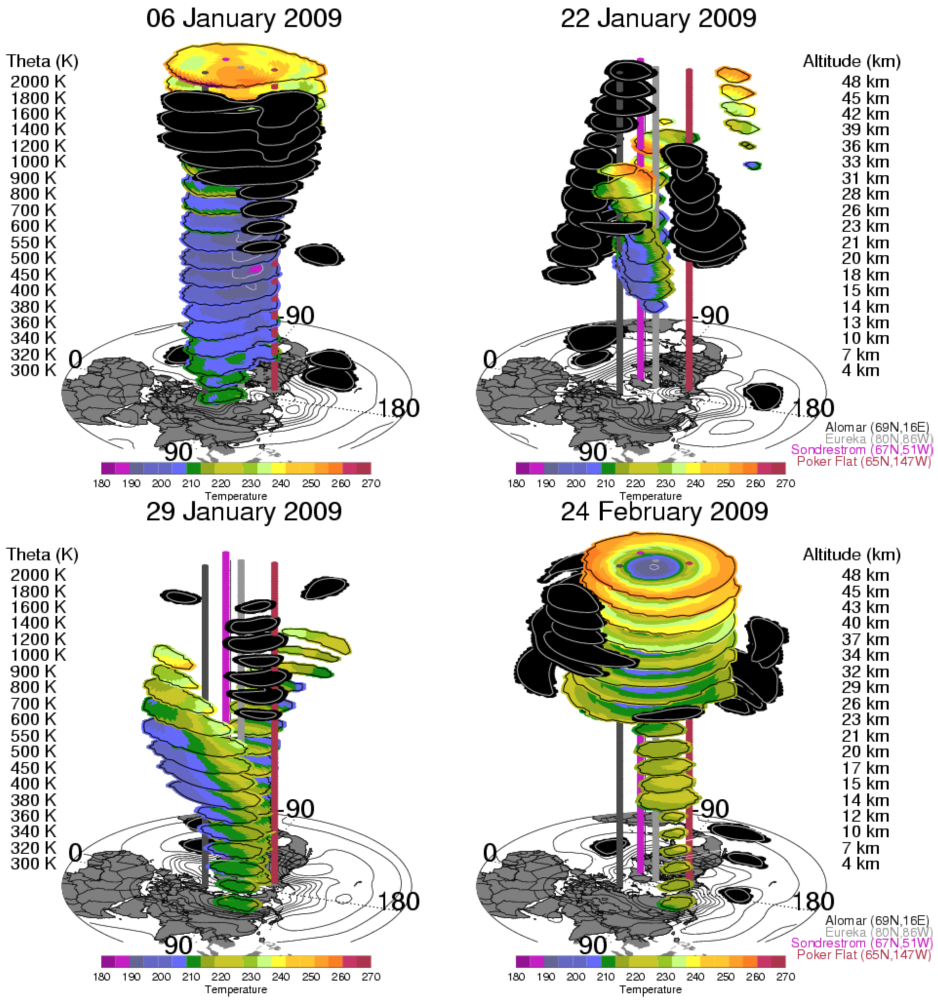

Figure 2.4. 3-D structure of the stratospheric vortex and anticyclones for four days in January-February 2009. The upper left panel are the structures before a sudden stratospheric warming. The upper right panel are the structures at the beginning of a sudden stratospheric warming. The lower left panels are the structures a week after the upper right panel. The lower right panel are the structures after the reformation of the vortex.

while the mid- and lower stratospheric vortex remained weak and lead to the formation of an elevated stratopause by 24 February 2009 (Figure 2.4, lower right panel). The red column indicates the location of Chatanika. On 06 January 2009 Chatanika is under the edge of the vortex, on 22 January and 29 January Chatanika lies between the small split vortices and anticyclones, and on 24 February Chatanika lies below the center of the upper stratospheric vortex.

We show the corresponding winds over Alaska in Figure 2.5 at 350 hPa (~8 km) and 7 hPa (~34 km). The winds at both altitudes are strongest on 6 January 2009 with Chatanika lying inside the edge of the vortex. Subsequently the winds at 350 hPa reflect the movement of the small vortices with discontinuous jets present. During this period, the winds at 7 hPa progressively weaken. We show the corresponding ΔNBE over Alaska in Figure 2.6 again at 350 hPa and 7 hPa. We see that the local maxima in ΔNBE correspond to the location of the jets in Figure 2.5. The ageostrophy is greatest at both altitudes on 6 January 2009 consistent with presence of the strongest winds and wind shears on that day. Subsequently the ageostrophy remains relatively strong at 350 hPa. During this period, the ageostrophy at 7 hPa progressively decreases as the winds weaken.

The evolution of the temperature profiles measured by the Rayleigh lidar at Chatanika is at consistent with the evolution of the stratospheric vortex. We plot the temperature profiles measured by the Rayleigh lidar in January and February 2009 in Figure 2.7. In early January when the vortex is well-formed, the temperature profile has a well-defined stratopause of 277 K at 58 km. By late January when the vortex is split the stratopause has disappeared. By late February when the vortex begins to reform an

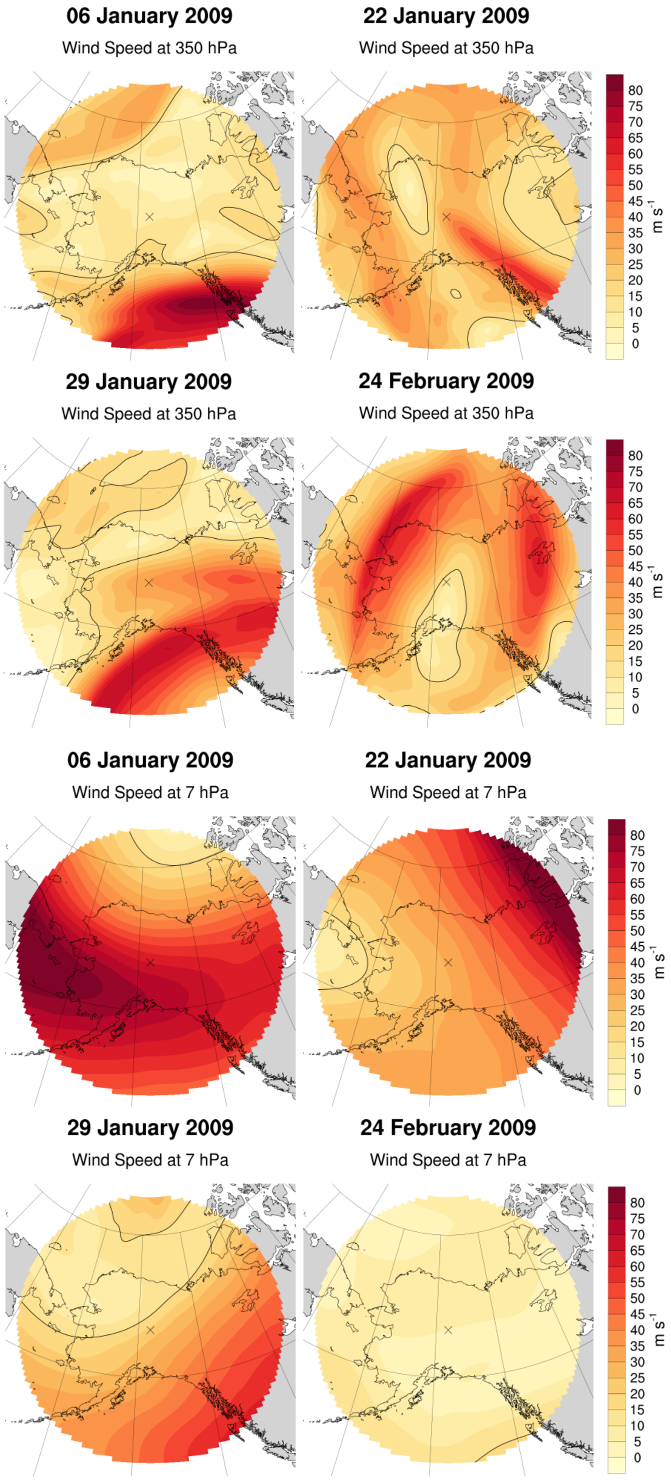

Figure 2.5. MERRA Horizontal wind speeds in false color over Alaska in January and February 2009 at 350 hPa (upper panels) and 7 hPa (lower panels). The solid line is the 15 m/s contour.

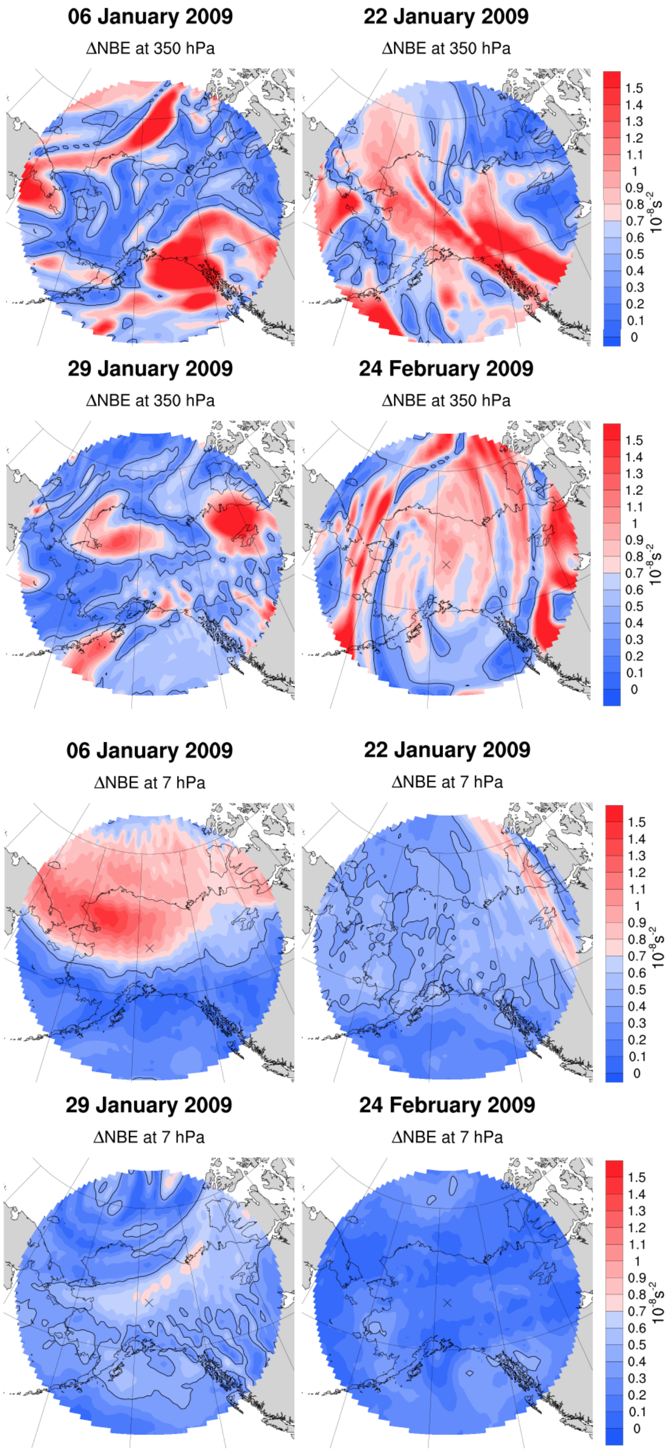

06 January 2009
ΔNBE at 350 hPa

22 January 2009
ΔNBE at 350 hPa

29 January 2009
ΔNBE at 350 hPa

24 February 2009
ΔNBE at 350 hPa

06 January 2009
ΔNBE at 7 hPa

22 January 2009
ΔNBE at 7 hPa

29 January 2009
ΔNBE at 7 hPa

24 February 2009
ΔNBE at 7 hPa

Figure 2.6. MERRA ΔNBE in false color over Alaska in January and February 2009 at 350 hPa (upper panels) and 7 hPa (lower panels). The solid line is the 4×10^{-8} s^{-2} contour.

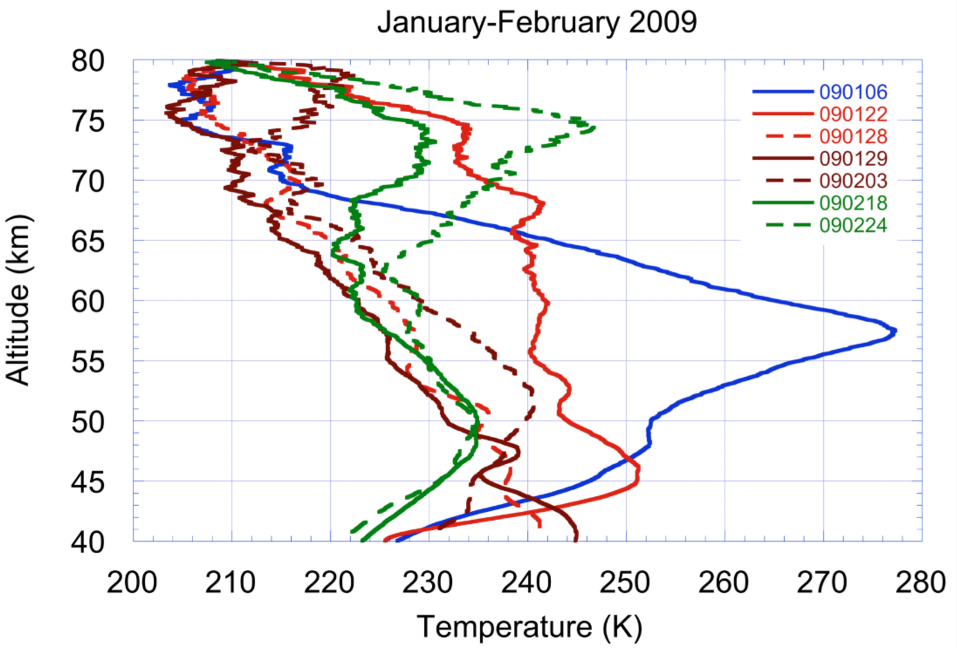

Figure 2.7. Rayleigh lidar temperature profiles for the seven nights of Rayleigh lidar data in January-February 2009.

elevated stratopause of 240 K at 73 km appears. The temperature profiles measured at Chatanika in January and February 2009 capture some of the key features of a major SSW as we discussed in Chapter 1. After the SSW the well-defined stratopause disappears, and a near isothermal temperature profile appears with no clear stratosphere evident. Once the circulation begins to recover, the winds and the vortex reform first at the upper altitudes and an elevated stratopause appears.

We plot the gravity wave activity measured at Chatanika during this period in Figure 2.8. We see that the gravity waves have the largest specific potential energies in early January, and the energy of the waves generally decreases in late January and February. We plot the wave energies over the 40-50 km and 45-55 km altitude ranges. On 6 January the gravity waves are growing most rapidly with altitude, and appear to be gaining energy with altitude and have an energy growth length of 44 km. For the six subsequent observations the gravity waves are losing energy with altitude and have an average of decay length of 8 km. On 21 January the waves have the shortest decay length of 4 km. There is no apparent relationship between the wave energy and the wave growth, the waves with higher energy do not appear to grow more or less rapidly than the lower energy waves. For example on 27 January the gravity waves have similar specific potential energy of 2.5 J/kg as on the 21 January of 2.8 J/kg but a such longer decay length of 12 km.

We plot the local wind profiles above Chatanika and the RMS winds over a circle of radius 800 km around Chatanika in Figure 2.9. The RMS winds show the presence of the polar night jet in the upper troposphere at 400 mb and the progressive disappearance of the stratospheric jet. The local wind profiles how more variability but the same general

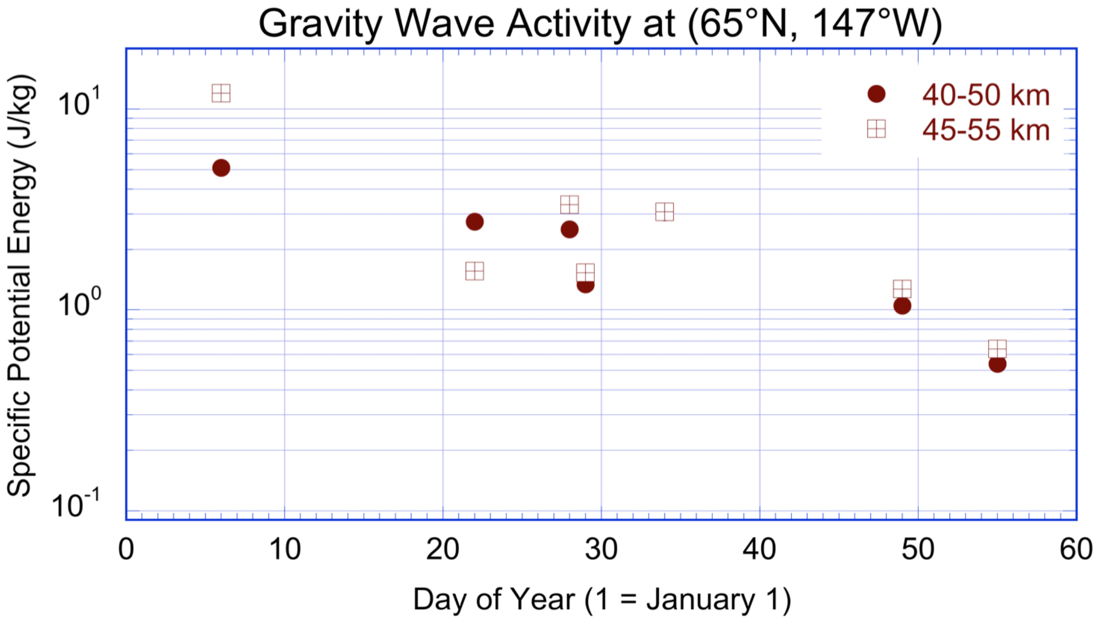

Figure 2.8. Specific potential energy for the seven nights of Rayleigh lidar data in January-February 2009 in day of year. Circles are averaged over 40 km to 50 km. Squares are averaged over 45 km to 55 km.

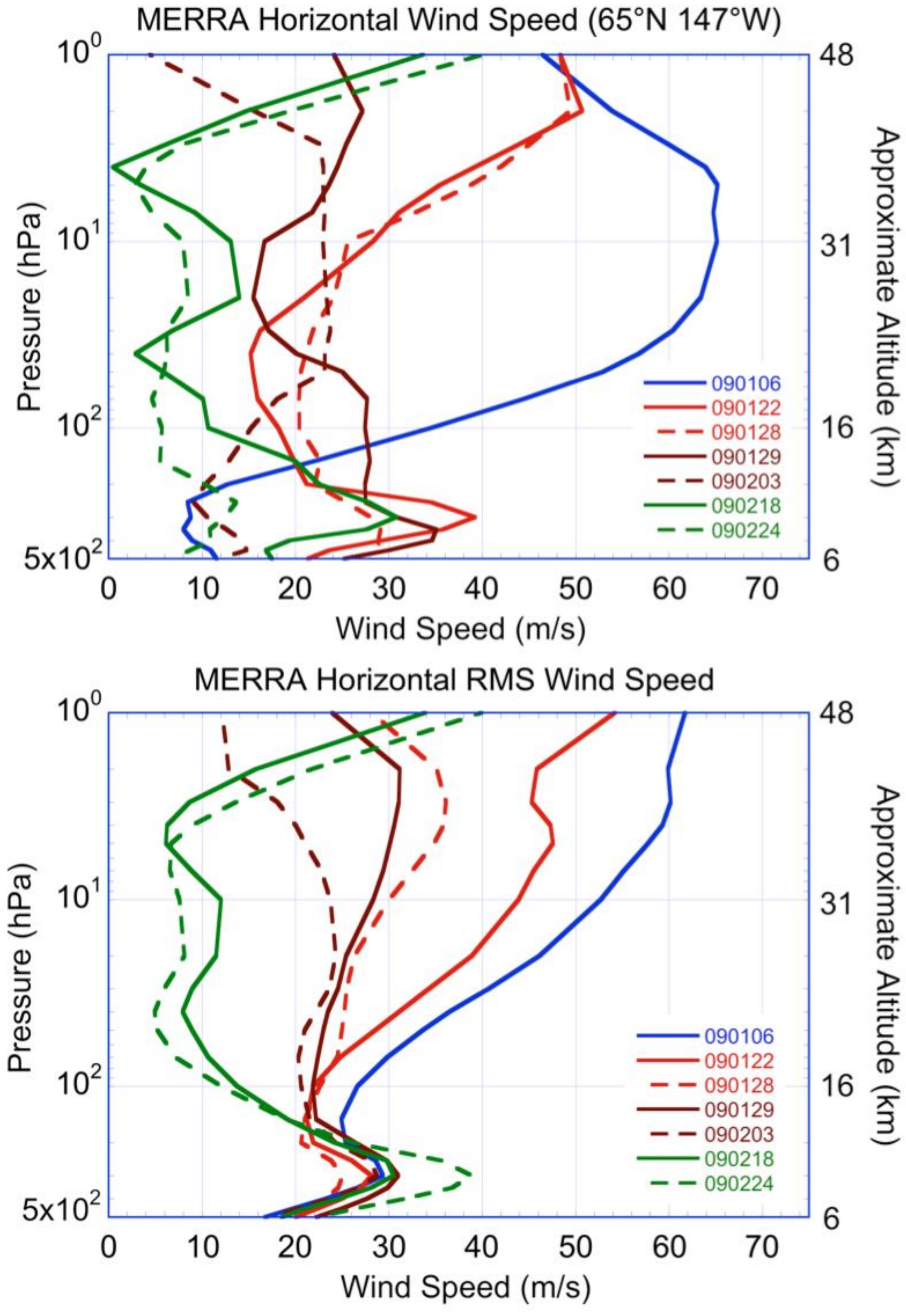

Figure 2.9. MERRA wind profiles over (top) and RMS winds speed in 800 km radius circle around (bottom) Poker Flat Research Range for the seven nights of Rayleigh lidar data in January-February 2009.

behavior. We plot ΔNBE averaged over a circle of radius 800 km around Chatanika in Figure 2.10. We see the largest values associated with the polar night jet in the upper troposphere. In the stratosphere the values of ΔNBE generally decrease over the two-month period. The behavior of ΔNBE is consistent with the evolution of the wind field, as the ageostrophy generally increases with the strength of the jets.

The variation of the gravity wave activity and the winds and ageostrophy in January and February 2009 highlights one of the main ambiguities in determining the origin of gravity waves as pointed out by O'Sullivan and Dunkerton [1995]. Strong winds can both generate gravity waves and also allow gravity waves to propagate. The largest wave energies are found when both the winds are strongest and the ageostrophy is largest on 6 January. The lowest wave energies are found when the winds are weakest and the ageostrophy is smallest on 18 February and 24 February.

2.5 Correlation between gravity wave activity and winds

To understand the relationship between winds and the gravity wave activity at Chatanika we calculate the correlation between the potential energy density of the gravity waves at 40-50 km and the horizontal wind speeds over Chatanika at each of the 26 altitudes. We present the Spearman correlation coefficients as a function of altitude in Figure 2.11. We consider the correlation in four distinct ways; all 152 observations ("All"), 81 observations from December, January, and February ("DJF"), 65 observations from DJF when the winter was disturbed ("DJF – DW"), and 16 observations from DJF when the winter was quiet ("DJF – QW"). Of the 13 winters, 11 are disturbed and 2 are quiet

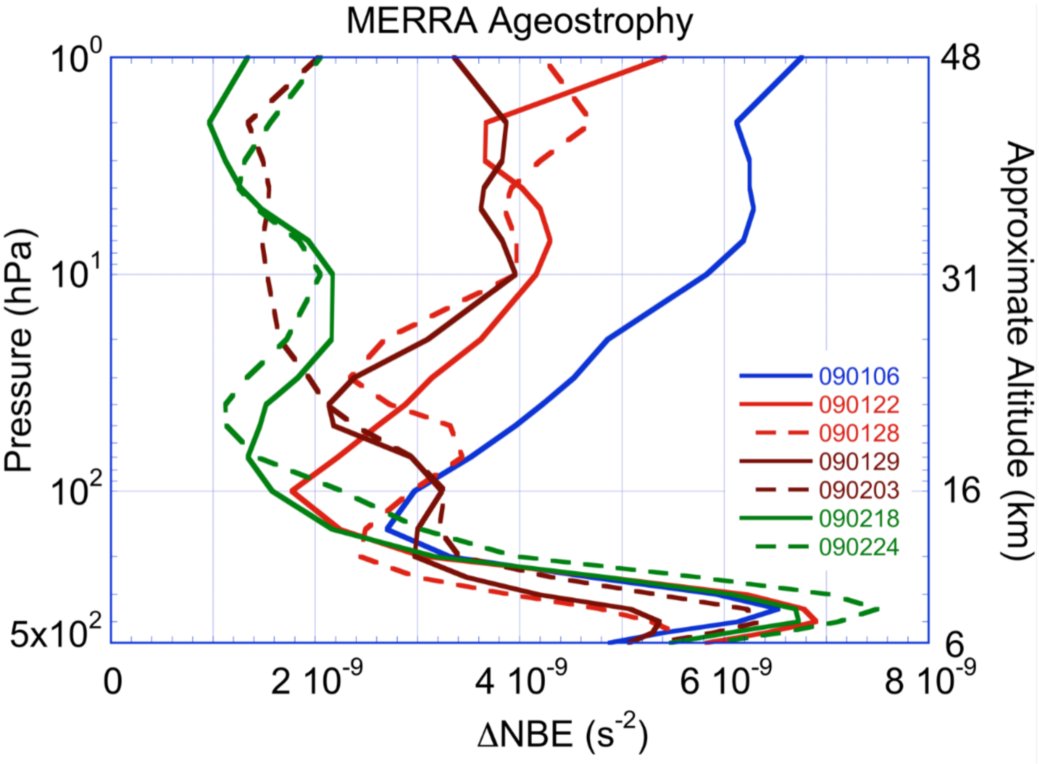

Figure 2.10. MERRA derived ΔNBE profiles over the 800 km radius circle centered on Poker Flat Research Range for the seven nights of Rayleigh lidar data in January-February 2009.

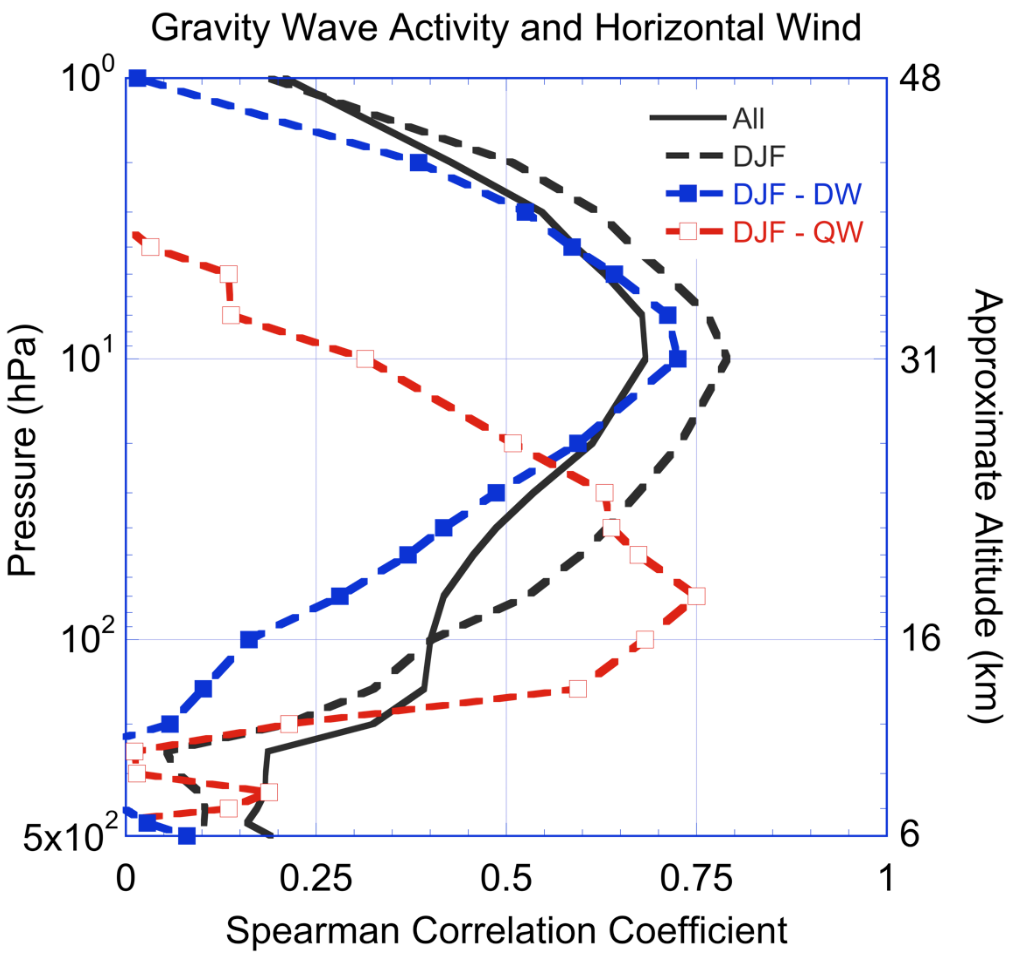

Figure 2.11. Spearman correlations of specific potential energy average over 40 km to 50 km and horizontal wind speed over Poker Flat Research Range in altitude. All is 152 night. DJF is all winter nights. DJF-DW is all winter nights in a DW. DJF-QW is all winter nights in a QW.

[Chandran et al., 2014]. Over all the 152 observations the correlation coefficient is greater than 0.6 between 20 hPa (~ 26 km) and 5 hPa (36 km) with a maximum value of 0.7 at 10 hPa (~31 km). The correlation coefficients increase when we only consider the wintertime gravity wave activity, and the correlation coefficient is greater than 0.6 between 40 hPa (~22 km) and 3 hPa (~40 km) with a maximum value of 0.8 at 10 hPa (~31 km). The altitude distribution changes significantly between disturbed and quiet winters. During disturbed winters the altitude distribution is similar to the distribution during all observations, with a maximum value of 0.7 at 10 hPa (~31 km), while during quiet winters the correlation moves downward having a maximum value of 0.8 at 70 hPa (~18 km). The Pearson correlation coefficients show similar altitude behavior. The correlation analysis shows a positive correlation indicating that the gravity wave potential energies increase with wind speed at all altitudes. We plot the gravity wave specific potential energies and horizontal wind speeds at an altitude of 10 hPa in Figure 2.12. The analysis of disturbed and quite winters shows that the highest correlation are found at the altitudes where the winds are weakest and indicates that the wind controls the propagation of gravity waves by low winds blocking the upward propagation of waves in the lower stratosphere.

The difference between the correlation in disturbed and quite winters reflects the change in the structure of the middle atmosphere winds. During quiet winters the winds in the middle atmosphere increase steadily with altitude in the stratosphere, while during disturbed winters the winds are weaker in the stratosphere, and a zero wind line moves down through the stratosphere and blocks the propagation of low phase speed gravity waves (e.g., Thurairajah et al. [2010a;b]). The wintertime correlation between the gravity

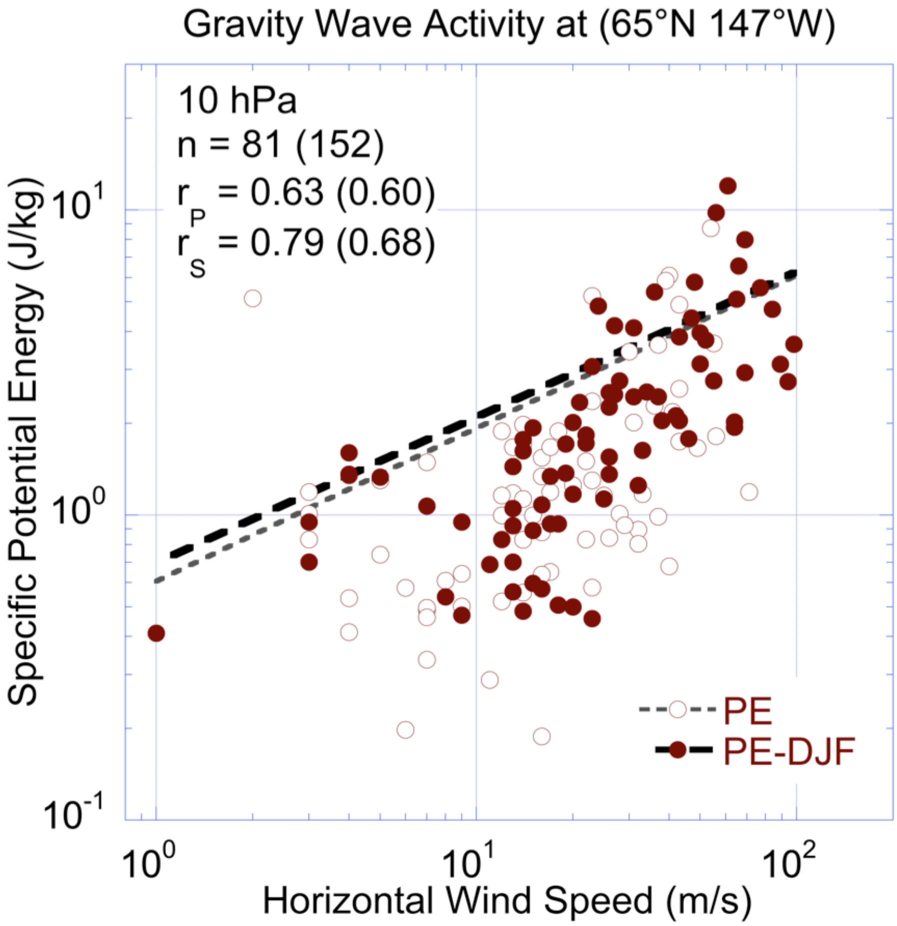

Figure 2.12. Example scatter plot of specific potential energy and horizontal wind speed at 10 hPa. The r values for both a Pearson Linear and Spearman's Rank correlation are given.

wave activity and the stratospheric winds is also evident inter-annually. We plot the mean wintertime gravity wave activity as a function of year in Figure 2.13 and the median wind profile over 13 winter seasons in Figure 2.14. The specific potential energies vary by a factor of 6 between 1 J/kg and 6 J/kg. There is only one observation in the winters of 1999-2000 and 2000-2001. The median wind profiles also show significant variability with strong winds during quite winters (e.g., 2004-2005, 2010-2011) and weak winds during strongly disturbed winters (e.g., 2001-2002, 2003-2004). The gravity wave activity is highest during the quiet winters of 2004-2005 and 2010-2011 (4-6 J/kg) and lowest in the disturbed winters of 2001-2002 and 2003-2004 (1 J/kg). The winter of 2003-2004 was highly disturbed due to the occurrence of a major and persistent stratospheric warming and formation of an elevated stratopause, while the winter of 2004-2005 was undisturbed with a robust polar vortex [Thurairajah et al., 2010a; Chandran et al., 2014].

2.6. Correlation between gravity wave activity and ageostrophy

To understand the ageostrophy and the gravity wave activity at Chatanika we calculate the correlation between the potential energy density of the gravity waves at 40-50 km and the ΔNBE at each of the 26 altitudes. We present the Spearman correlation coefficients as a function of altitude in Figure 2.15. We first consider the correlation for all 152 observations (“All”) and then for the 81 wintertime observations (“DJF”). In both these cases we see that the values of the Spearman correlation coefficient steadily increase with altitude from the troposphere to the stratosphere, but are 0.4 or less at all altitudes. Given the fact that the winds can block the upward propagation of gravity waves

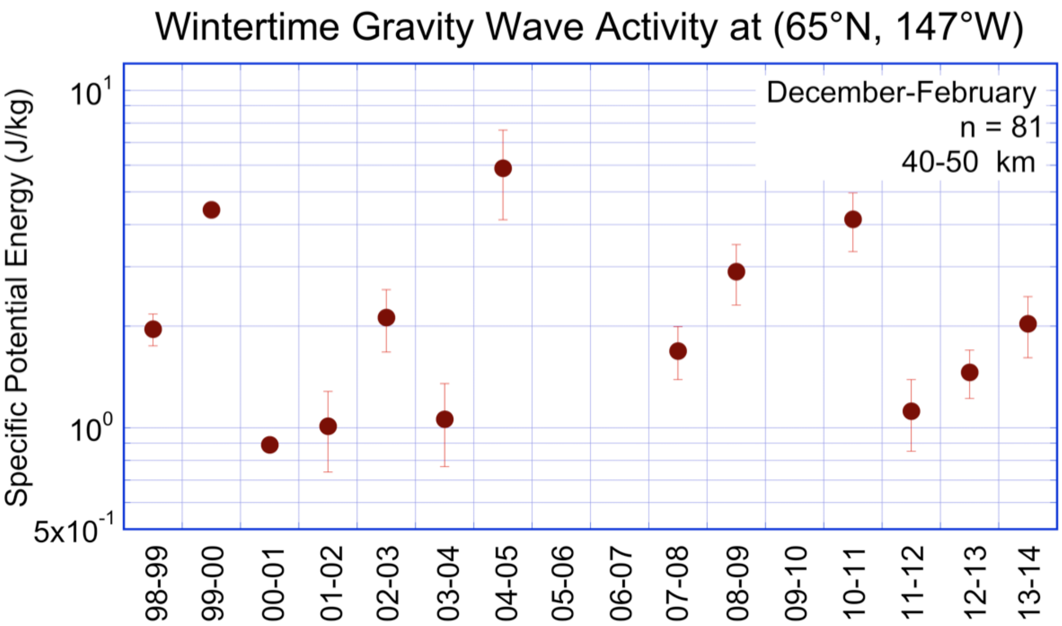

Figure 2.13. Wintertime averaged values of specific potential energy. Values for 05-06, 06-07, and 09-10 are omitted because no data was taken.

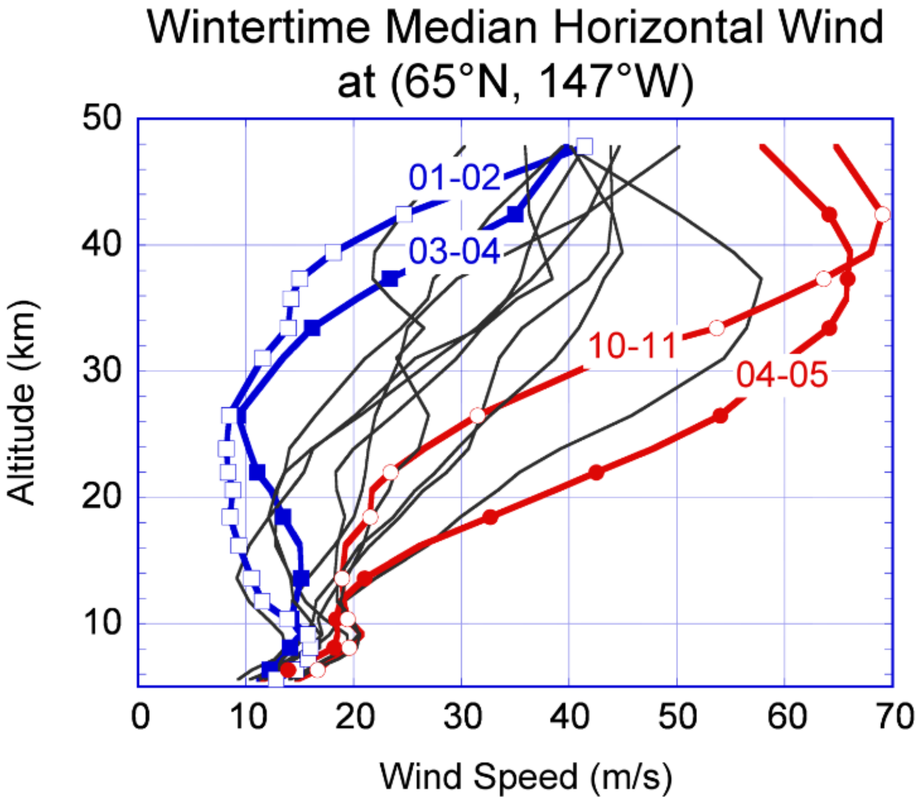

Figure 2.14. Wintertime median horizontal wind over Poker Flat Research Range. Winters of low wind speed are plotted in blue. Winters of high wind speed are plotted in red.

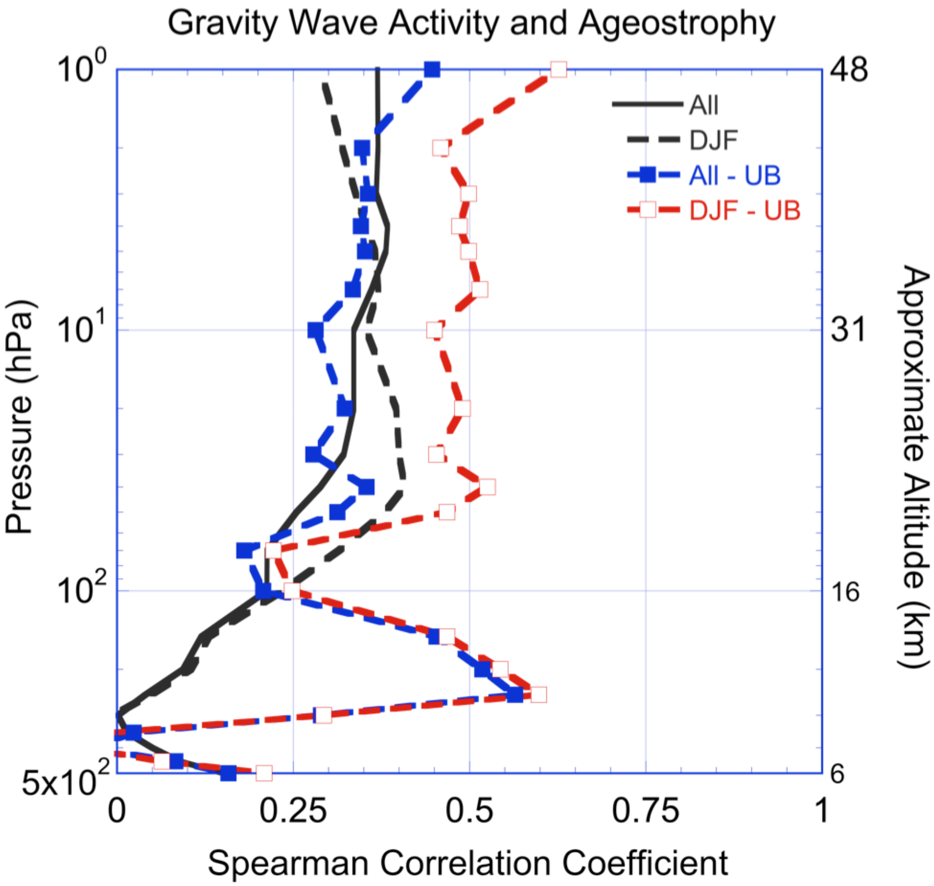

Figure 2.15. Spearman correlations of specific potential energy average over 40 km to 50 km and ΔNBE around Poker Flat Research Range in altitude. All is 152 night. DJF is all winter nights. ALL-UB is all nights where the winds are higher than 15 m/s (i.e., unblocked). DJF-UB is all winter nights where the winds are higher than 15 m/s.

we also consider those days where winds are strong and the propagation of gravity waves is unblocked. We set a threshold of 15 m/s and consider those observations where the winds are greater than that threshold value. There are 18 observations where the wave propagation is unblocked (“All - UB”). There are 15 wintertime observations where the wave propagation is unblocked (“DFJ - UB”). For the unblocked data the correlation between the gravity wave activity and the ΔNBE increases to greater than 0.6 at 250 hPa (~ 10 km) and increases to about 0.5 through the stratosphere above 50 hPa (~21 km). This high correlation between the gravity wave activity in the upper stratosphere and ΔNBE in the upper troposphere reflects the action of the jet stream which is typically found near 300 hPa. The northern hemisphere tropospheric jet stream has significant ageostrophy and has characteristic NBE with large magnitude and variability. ΔNBE has units of s^{-2} and a given value of ΔNBE has a larger forcing in the denser lower atmosphere than the sparser upper atmosphere.

The values of the correlation coefficients in the stratosphere for the unblocked observations in wintertime are higher than for all unblocked observations. This may reflect larger ageostrophy in the wintertime middle atmosphere. However, the values of ΔNBE are correlated between altitudes reflecting the influence of upwardly propagating planetary waves that are breaking and yielding ageostrophic flows. We conclude that the correlation analysis that the ageostrophy in the upper troposphere, rather than the stratosphere, is the primary contribution to the gravity waves activity in the 40-50 km altitude region.

2.7. Summary and conclusions

We have documented the gravity wave activity in the upper stratosphere and lower mesosphere (USLM) over 14 years based on uniform processing of a high-quality set of Rayleigh lidar observations. Despite large daily variability, the gravity wave activity shows a clear annual cycle with a maximum in winter, and systematic inter-annual variability associated sudden stratospheric warming events. The gravity waves in the USLM are losing energy with altitude and have a decay length of 17 km, indicating that the gravity waves are saturated.

We find that the gravity wave activity in the upper stratosphere and lower mesosphere is controlled by the winds in the lower stratosphere, where weak winds in the lower stratosphere block the upward propagation of gravity waves through critical layer filtering. This control is evident on both daily and seasonal time scales, where systematic changes in the winds are associated with sudden stratospheric warming events.

We find that the gravity wave activity in the upper stratosphere and lower mesosphere is correlated with the ageostrophy in the tropospheric jet. This coupling is only apparent when the waves are not blocked by the winds in the lower stratosphere. Thus we conclude that the primary control of the gravity wave activity is critical layer filtering by the winds in the lower stratosphere, and the secondary control of gravity wave activity is ageostrophic adjustment by the tropospheric jet.

Chapter 3 CONE Ion Gauge and Rayleigh Lidar Instruments

3.1. Introduction

In this Chapter we describe the COmbined measurement of Neutrals and Electrons (CONE) ionization gauge and the Rayleigh lidar used in the Mesosphere-Lower Thermosphere Turbulence Experiment investigation. We provide a detailed described of the data retrieval techniques that we developed for both instruments. For the CONE ionization gauge we have developed a new method to determine the atmospheric density profile from the inflight data rather than laboratory calibration curves [Rapp et al., 2001]. For the Rayleigh lidar system we have extended and upgraded the lidar to make measurements of temperature and density to higher altitudes than in previous studies [Collins et al., 2011].

3.2. CONE ionization gauge

The CONE ionization gauge is a classic triode-type ionization gauge that is optimized for a pressure range of 10^{-5} hPa to 1 hPa. CONE consists of a set of spherical electrode grids that allow air molecules to pass freely through the sensor. This spherical architecture was designed to reduce the instrument time constant and biases due to aerodynamic effects. The instrument was developed in the 1990s in the University of Bonn [Hillert et al., 1994; Rapp et al., 2001]. There are two primary signals of interest in the CONE instrument; the emission current, and the electrometer current. The emission current is the current that ionizes the air. The electrometer current is the resultant ion current that is proportional to the density of the air passing through the sensor. In Figure

3.1 we show the CONE sensor. Two CONE instruments were required for the two sounding rocket flights of the National Aeronautics and Space Administration (NASA) sponsored Mesosphere-Lower Thermosphere Turbulence Experiment (MTeX) investigation (46.009 and 46.010). The CONE instrument consists of an integrated sensor and electronics package. For the MTeX investigation the Leibnitz Institute of Atmospheric Physics (L-IAP) provided the two CONE sensors. The sensors were identical in design to those used in earlier investigations (e.g., Lehmacher et al. [2011]). However, the CONE electronics were redesigned with contemporary Field Programmable Gate Array circuitry to yield higher measurement sensitivity and sampling rate, and to interface with NASA telemetry signals. The sampling rate was increased from 3255 Hz to 5209 Hz yielding a new sampling resolution of 192 μs. The new CONE electronics were redesigned and fabricated by von Hoerner and Sulger GmbH (Schwetzingen, Germany). The new design was implemented with a contemporary set of Field Programmable Gate Arrays. The Programmable Logic used in the previous CONE had become obsolete. The CONE sensor is designed to make measurements at low density in the middle and upper atmosphere with pressure less than 1 hPa and density less than 2×10^{-3} kg/m^3. At higher pressure and densities the emission and electrometer currents are too large and the sensor filament burns out. During the MTeX mission the CONE sensor was turned on above 60 km at an expected pressure of 0.2 hPa and a density of 2×10^{-4} kg/m^3 [MSIS, 2016]. The CONE electronics were designed with autoranging to allow for density measurements over five orders of magnitude. The autoranging had five ranges; range four (least sensitive, at highest density and lowest altitude) to range zero (most sensitive, at lowest density highest altitude). The electronic gain increases by a

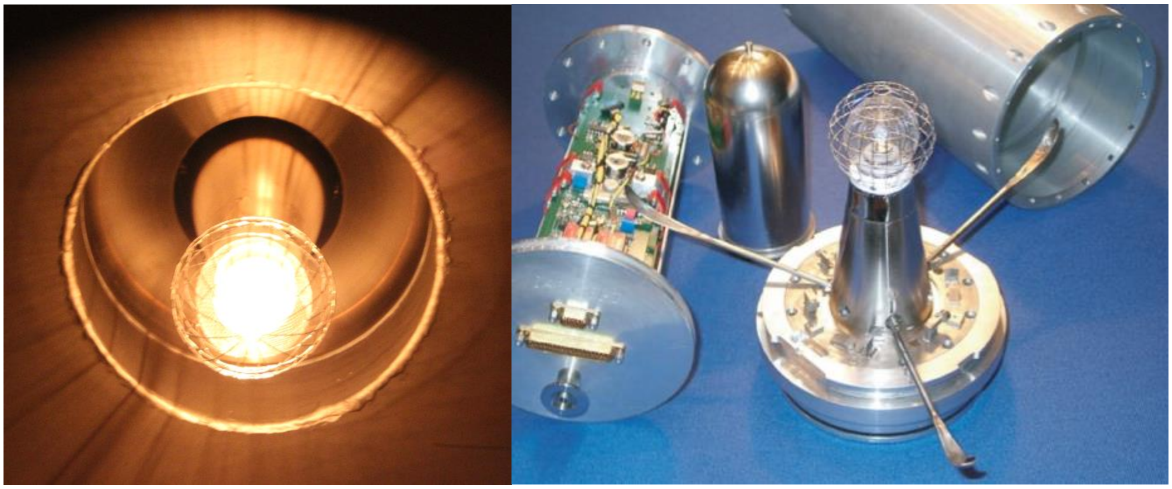

Figure 3.1. The CONE instrument. Left: Photograph of CONE sensor with filament ignited in a vacuum chamber during testing. Right: CONE sensor and electronics on benchtop. Photos by Richard Collins (left) and Gerald Lehmancher (right).

nominal factor of 10 as the range decreased from one range to the next. The CONE sensors and electronics were integrated into the CONE instruments at L-IAP in July of 2014. The CONE instruments were then integrated into the two MTeX payloads at NASA Wallops Flight Facility in August of 2014. In Figure 3.2 we show one of the MTeX payloads with the CONE instrument at the front of the payload. The MTeX rocket payloads incorporate attitude control systems that turned the payloads at apogee to allow measurements to be made on both the upleg and downleg of the flights.

Before discussing the CONE data retrieval we summarize the details of the MTeX 46.009 and 46.010 flights. The 46.009 rocket (the ninth Terrier-Improved Malemute launched by NASA) was launched at 00:13:01 LST (09:13:01 UT) on the morning of 26 January 2015. The 46.010 rocket (the tenth Terrier-Improved Malemute launched by NASA) was launched at 00:46:01 LST (09:46:01 UT) on the morning of 26 January 2015. The details of both rocket trajectories are listed in Table 3.1. The CONE signals were recorded with an internal clock that started when the CONE instrument was turned on before launch. The rocket position and time along its trajectory is recorded at 50 ms resolution using the Global Positioning System (GPS). The CONE instrument began making measurements when the filament in the CONE sensor was turned on about one minute after launch. The filament remained on through the flight until the filament burnt out in the downleg near 60 km. The primary measurement altitude range is between 70 km and 120 km. The CONE instrument requires an angle of attack (i.e., angle between payload axis and ram direction) of less than 10° to make accurate density measurements [Lehmacher et al., 2011]. In both MTeX flights the rocket angle of attack remained less than 6° over the measurement range of 70 km to 120 km. We visually inspected the

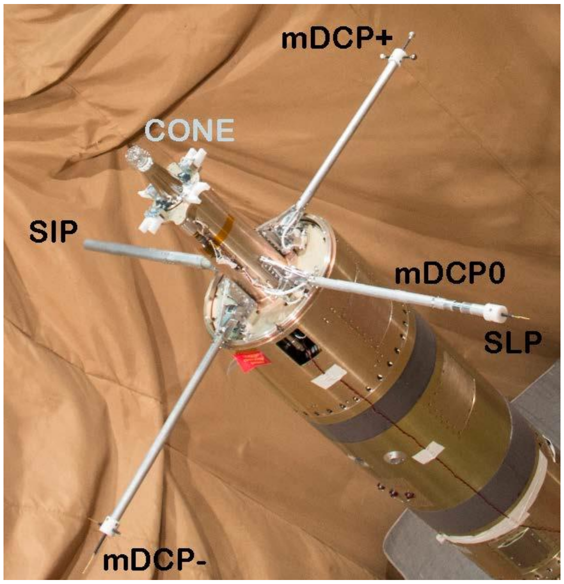

Figure 3.2. Photo of MTeX Payload taken at NASA Wallops Flight Facility during system integration and testing. The CONE sensor is seen on the top of the payload with plasma instrumentation on booms around it. Photo by Richard Collins.

Table 3.1: Summary of MTeX Flights

	Payload	
	46.009	46.010
CONE turn on time[1]	-681.236 s	-693.741 s
CONE filament on time[1]	61.85 s	62.15 s
CONE filament on altitude[2]	65.7 km	65.6 km
70 km	65.20 s	65.55 s
120 km	111.95 s	113.05 s
Apogee time	202.30 s	201.35 s
Apogee altitude	158.2 km	156.4 km
120 km	292.70 s	289.55 s
70 km	339.45 s	337.05 s
Angle of attack	< 6°	< 6°

[1]: Time is relative to launch at t = 0 s.

[2]: Flight times and altitudes are recorded at 0.05 s resolution

electrometer current for both flights. We find that during the upleg of 46.010 there were anomalies in the electrometer current at altitudes below 80 km. We did not analyze the data from the 46.010 upleg further. We describe the CONE data retrieval and methodology and highlight the measurements from the upleg in MTeX flight 46.009 for illustration.

3.3. CONE data retrieval and methodology

We averaged the electrometer and emission currents over 50 ms intervals to correspond to the GPS time resolution. We then took the ratio of the averaged electrometer current to the average emission current. This avoids changes in the electrometer current due to changes in the emission current appearing as atmospheric features. This ratio gives us the CONE relative measurement of the density. We plot the electrometer current (top panel), emission current (middle panel), and the ratio of the electrometer to the emission current (bottom panel) for flight 46.009 in Figure 3.3. All three panels of Figure 3.3 are in time after the CONE instrument was turned on 681 s before launch. In the 46.009 upleg the CONE sensor filament turned on in range 4, providing measurements from 66 to 74 km, then switched to range 3 from 74 to 88 km, range 2 from 88 to 103 km, range 1 from 103 to 117 km, and range 0 from 117 to 158 km. In the 46.009 downleg the CONE instrument remained in range 4 down to 116 km, then switched to range 1 from 116 to 102 km, range 2 from 102 to 87 km, range 3 from 87 to 74 km, and range 4 from 74 to 62 km. There is a glitch in the electrometer current at 818 s and 138 km. This glitch (like others) were identified by visual inspection and removed from further analysis.

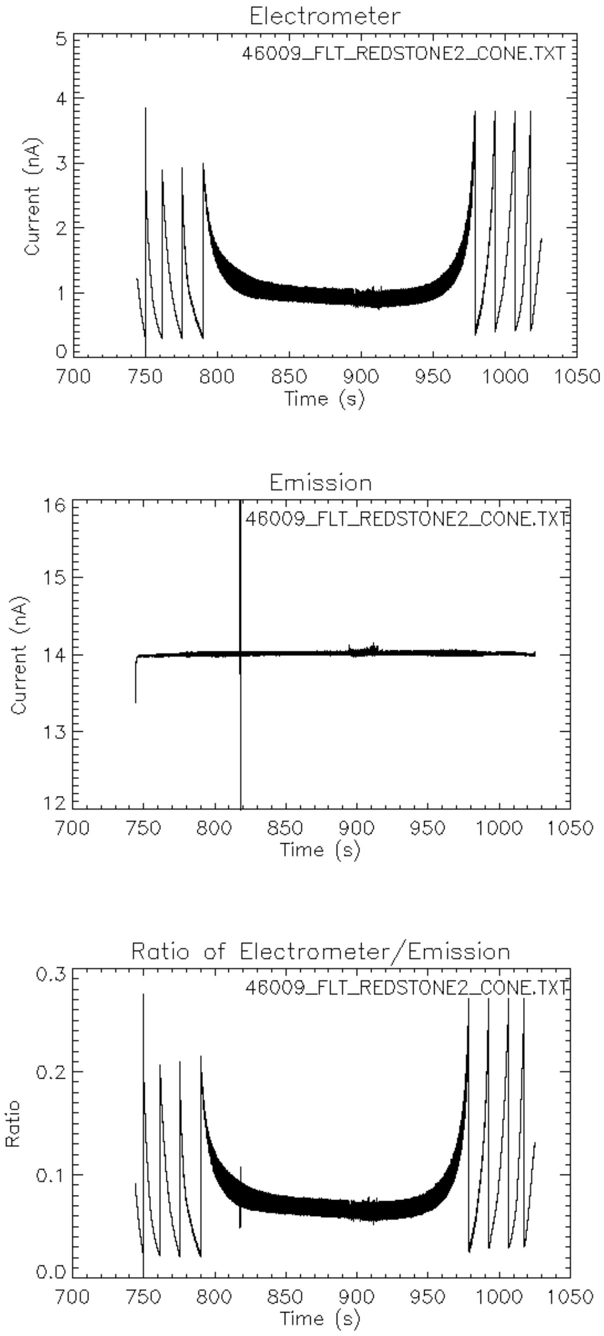

Figure 3.3. Example of electrometer (top) and emission (middle) current from the flight of 46.009 and their ratio (bottom) showing raw relative density values. The time on the x-axis to time after CONE instrument turn on.

The range changes are seen in the top and bottom panel of Figure 3.3 as discontinuities. In order to produces continuous density profiles, we need to correct these discontinuities. Also, around range changes there is contamination of the currents from electronic switching and turn-on that could affect the density measurement. We omitted 20 data points on both sides of the range change from the calculation to avoid this possible contamination.

3.4. Retrieval of density profile from CONE measurements

The CONE density retrieval was performed as an independent check on existing retrieval methods [Szewczyk, 2015]. We decided that this method would be based solely on continuity arguments and give an along-the-flight renormalization of the CONE profile. We assumed that the large-scale density should vary continuously over each range transition. Continuity calculations were done independently for each leg of each flight of the MTeX investigation. We begin our analysis with pressure chamber calibrations that were performed on the CONE instruments at L-IAP. These measurements were used to calibrate the sensitivity of each range to pressure; these will be referred to as the "L-IAP calibration". The temperature in the pressure chamber remained constant during the measurements, and so the sensitivity to pressure represents the sensitivity to density. We show the basic measurement in each range in Figure 3.4 for the combination of CONE sensor #2 and CONE electronics #2 that was used in payload 46.009. In the left panels of Figure 3.4 we show the measurements of ratio of the electrometer to emission current and pressure as a function of time. The raw measurements were made every 196 μs and then averaged over one second. In the right panels of Figure 3.5 we show the

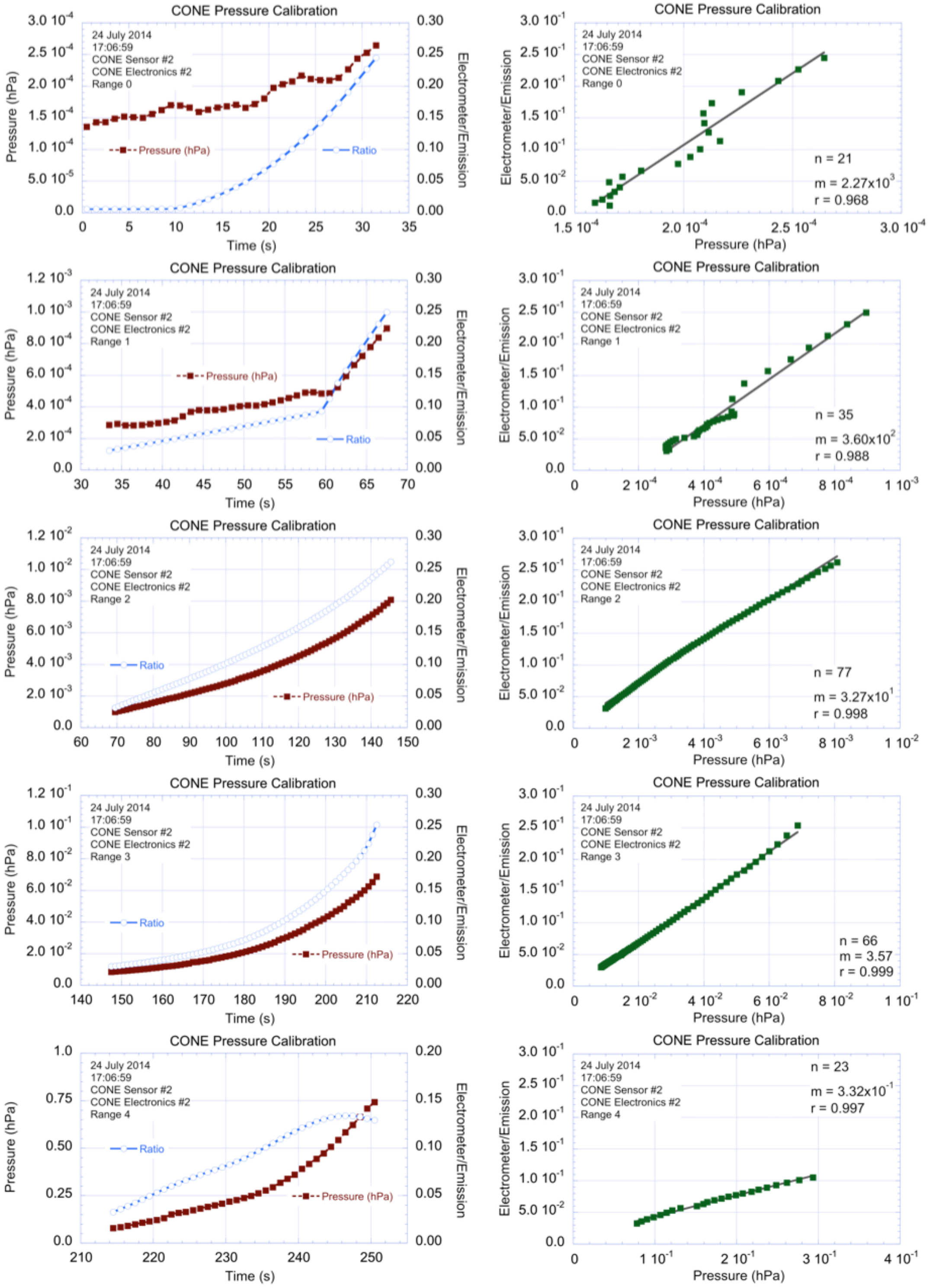

Figure 3.4. Example of CONE pressure calibration data (left) and calibration curves (right) for CONE senor #2 and CONE electronics #2. The left panels show ratio of electrometer-to-emission current with pressure in time of the experiment. The right panels show the calibration curves found for this experiment.

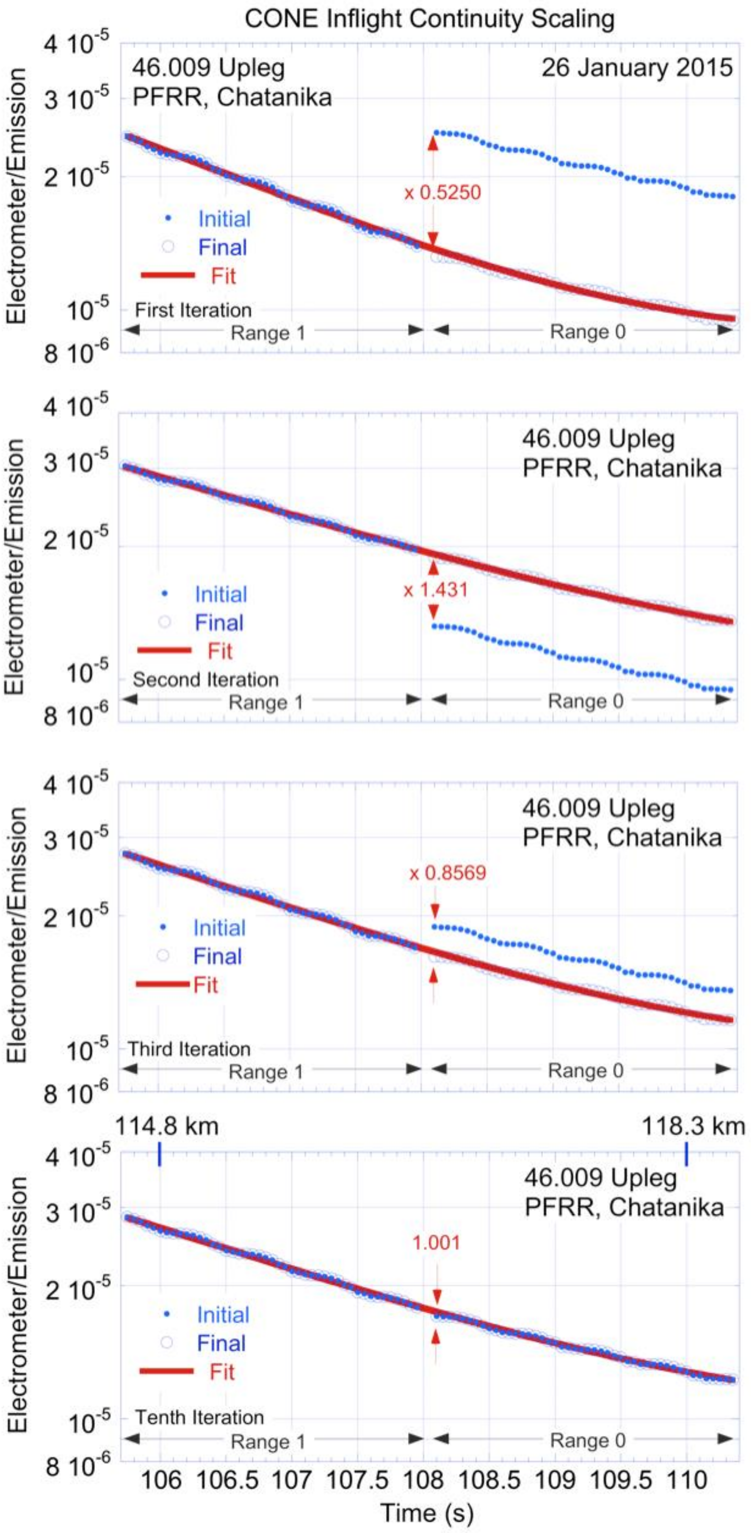

Figure 3.5. Example of iterative method used to make the CONE data continuous over range changes.

measurements of ratio of the electrometer to emission current as a function of pressure. For each measurement range we conduct a linear fit between the ratio of the electrometer to emission current and the pressure. In range 0 we omitted the first ten measurements where the CONE instrument does not appear to respond to the change in pressure at pressures less thab1.5x10^{-4} hPa. In range 4 we omitted the last 14 points at pressures greater than 0.3 hPa. At higher pressure (and density) the CONE instrument saturates and it's measurement sensitivity changes. In Table 3.2 we first tabulate the results of these fits for both CONE instruments, Sensor #1 and Electronics #1 (Cone Instrument #1, 46.010), Sensor #2, and Electronics #2, (CONE instrument #2, 46.009). We report the slope of the linear fit, m, between CONE signal and pressure, which is the measurement sensitivity, S, and the linear correlation coefficient, R. We conducted two measurements or trials for each CONE instrument. As expected the sensitivity decreases as range increases with an order of magnitude change between each range. The correlation coefficients are lowest in range 0 where the CONE instrument noise is highest and the pressure measurements are least precise. We take the average of the sensitivities for each range from trails 1 and 2 and from trials 3 and 4 as our initial estimate of the CONE measurement sensitivities. We tabulate these values in Table 3.3.

We now consider the inverse of the measurement sensitivity as the normalized relative gain of the instrument that relates the measured electrometer-to-emission ratio (or ratio) to the atmospheric density. We first invert the CONE measurement sensitivities and then renormalize them to the value in range 4. We chose range 4 because it has the lowest noise. We tabulate these renormalized gain factors in Table 3.3. Thus we see that for CONE instrument #2 ratio of 0.05 corresponds to a relative density of 5x10^{-2} in

Table 3.2: CONE normalized relative gain from pressure chamber calibration.

Sensor	Electronics		Range				
Trial 1a			0	1	2	3	4
2	2	S	2.27×10^{3}	3.60×10^{2}	3.27×10^{1}	3.57	3.32×10^{-1}
		R	0.968	0.988	0.998	0.999	0.997
Trial 1b							
2	2	S	2.28×10^{3}	3.75×10^{2}	3.32×10^{1}	3.58	3.97×10^{-1}
		R	0.986	0.995	0.998	1.00	0.999
Trial 2a							
1	1	S	1.50×10^{3}	3.03×10^{2}	3.05×10^{1}	3.54	3.18×10^{-1}
		R	0.826	0.999	0.999	0.998	0.998
Trial 2b							
1	1	S	1.85×10^{3}	2.86×10^{2}	2.98×10^{1}	3.36	2.96×10^{-1}
		R	0.905	0.999	0.999	0.999	0.997

Table 3.3: CONE normalized relative gain from pressure chamber calibration[1].

Payload	Instrument	Range				
		0	1	2	3	4
46.009	2	*2.54×10^{3}*	*3.68×10^{2}*	*3.30×10^{1}*	*3.57*	*3.64×10^{-1}*
		3.93×10^{-4}	2.72×10^{-3}	3.03×10^{-2}	2.80×10^{-1}	2.74
		1.43×10^{-4}	9.92×10^{-4}	1.11×10^{-2}	1.02×10^{-1}	1
46.010	1	*1.68×10^{3}*	*2.94×10^{2}*	*3.01×10^{1}*	*3.45*	*3.07×10^{-1}*
		5.97×10^{-3}	3.40×10^{-3}	3.32×10^{-2}	2.90×10^{-1}	3.26
		1.83×10^{-4}	1.04×10^{-3}	1.02×10^{-2}	8.90×10^{-2}	1

[1]: Values in italics are the averages of results from two trials in Table 3.2

range 4, 5.10x10^{-3} in range 3, 5.55 x10^{-4} in range 2, 4.96x10^{-5} in range 1, 7.15x10^{-6} and in range 0. Our goal is to yield an accurate relative density profile that reproduces the actual variation with altitude just like a Rayleigh lidar signal profile.

The L-IAP calibration results in Table 3.3 are a first estimate of the scaling, but they do not eliminate the discontinuities. For this we now use an iterative fitting method. We start with the range 4-range 3 transition. Range 4 is left unscaled and range 3 is scaled by the product of L-IAP calibration and the ratio of a 5-point averaged value on both sides of the range change. We then nudge the range 3 data by a factor ranging from 0.1 to 1.359 in steps of 0.001. At each nudging step we perform a 3rd-order fit in the log-domain to the ratio spanning 2 km on each side of the range change. For each fit we find the RMS error. After all nudging steps we record the scale factor (the product of L-IAP, 5-point average, and the nudge value) of the best fit. We now repeat this process with range 3-range 2 and range 2-range 1. For range 1-range 0 we adapt the process due to the fact that the instrument background current is relatively higher in range 0 than the other ranges. This is evident in Figure 3.3 where the ratio profile flattens out in range 0. For range 1-range 0, we estimate the constant background signal as the average of the ratio at altitude above 150 km. We subtract this value from the range 0 ratio, and proceed with the nudging as before. We now have completed our initial in-flight renormalization. We now proceed iteratively, propagating the background signal through all the ranges. In our first iteration step we use the scaling factors founds in the initial renormalization to estimate the background signal in all ranges. We then subtract this background from the ratios and estimate the new renormalized relative gain factors. We the second iteration process we use the scaling factors founds in the first iteration of the renormalization to update the background signal in all ranges and estimate updated renormalized relative gain factors. We continue with these iterations until the renormalized relative gain factors change by less than one-part-in-one-thousand. We illustrate the process for the upleg in flight 46.009 (CONE instrument #2) in Figure 3.5. The process took 10 iterations to converge. We tabulate our final estimates of the normalized relative gain factors in Table 3.4. The values of the normalization relative gain for CONE instrument #2 differ by less than 15% between the upleg and downleg in flight 46,009. The values of the normalization relative gain for CONE instrument #2 and CONE instrument #1 differ by less than 7% between the downlegs in flight 46,009 and 46.010 respectively. The normalization relative gain in Tables 3.4 and 3.3 differ by between 0% and 37% between the L-IAP calibration and in-flight renormalization. As expected, the differences are largest in the lower ranges (0 and 1) where the influence of the background is greatest.

We tabulate the background signal in Table 3.5. The values show the estimate of the background signal in each range. The value in range 4 represents the value for the background signal when the entire profile is normalized relative to the signal in range 4. We highlight these values in italics. The value in range 0 is the directly calculated value based on the average of the signal at altitudes above 150 km. The values in the other ranges are the scaled values based on the gain normalizations. As expected the values decrease by about an order of magnitude in each range.

Having corrected the electrometer-to-emission-ratio (or ratio) profile for the range changes, we now formally calculate the relative density profile that will be used to determine the temperature. We first take a 3rd-order polynomial fit to the log of the ratio profile over the 70-120 km. We then calculate the residual of the fit as the difference

Table 3.4: CONE normalized relative gain from inflight calibration.

Flight Leg	Instrument	Range				
		0	1	2	3	4
46.009 Upleg	2	1.21×10^{-4}	1.16×10^{-3}	1.11×10^{-2}	1.07×10^{-1}	1
46.009 Downleg	2	1.40×10^{-4}	1.30×10^{-3}	1.24×10^{-2}	1.14×10^{-1}	1
46.010 Downleg	1	1.34×10^{-4}	1.24×10^{-3}	1.16×10^{-2}	1.07×10^{-1}	1

Table 3.5: CONE background signal from inflight calibration.

Flight Leg	Instrument	Range				
		0	1	2	3	4
46.009 Upleg	2	6.78×10^{-2}	7.04×10^{-3}	7.39×10^{-4}	7.68×10^{-5}	8.17×10^{-6}
46.009 Downleg	2	6.40×10^{-2}	6.90×10^{-3}	7.26×10^{-4}	7.85×10^{-5}	8.97×10^{-6}
46.010 Downleg	1	6.15×10^{-2}	6.65×10^{-3}	7.11×10^{-4}	7.66×10^{-5}	8.97×10^{-6}

between the log of the ratio and the third order polynomial. We then smooth the residual with a 2 km running Parzen window [Harris, 1978]. We add the smoothed residual to the third-order polynomial and take the exponential as the relative density profile. We plot the ratio profile in the upleg of flight 46.009 in Figure 3.6. The white curve is the ratio profile. The horizontal dashed line indicates the background signal and corresponds to the value that appears in italics in Table 3.5. The signal is greater than the background signal up to 120 km. The vertical yellow lines indicate the range transitions. The green line is the corrected profile between 70 and 120 km. The dark blue curve is the difference between the ratio profile and the profile based on the third-order polynomial fit. We see that there are up to 10% differences in the two profiles. The light blue dots are the difference between the ratio profile and the profile based on the third-order polynomial fit with the smoothed residual. We see that there are up to 1% differences in the two profiles. The red dots is the difference between the ratio profile and the profile based on a step-wise third-order polynomial fit. We see that there are up to 1% differences in the two profiles. We use the fit with the third-order polynomial and smoothed residual as the relative density profile to compute the temperature profile.

3.5. Retrieval of temperature profile from CONE measurements

We use the standard Rayleigh lidar technique to calculate temperatures from the gain-corrected CONE data (e.g., Thurairajah, 2009). The technique uses a seed temperature at an upper altitude and downward integration of the relative density, under the assumption of hydrostatic equilibrium, to find temperature. This is useful as the integration become insensitive to the initial temperature guess and converges to the true

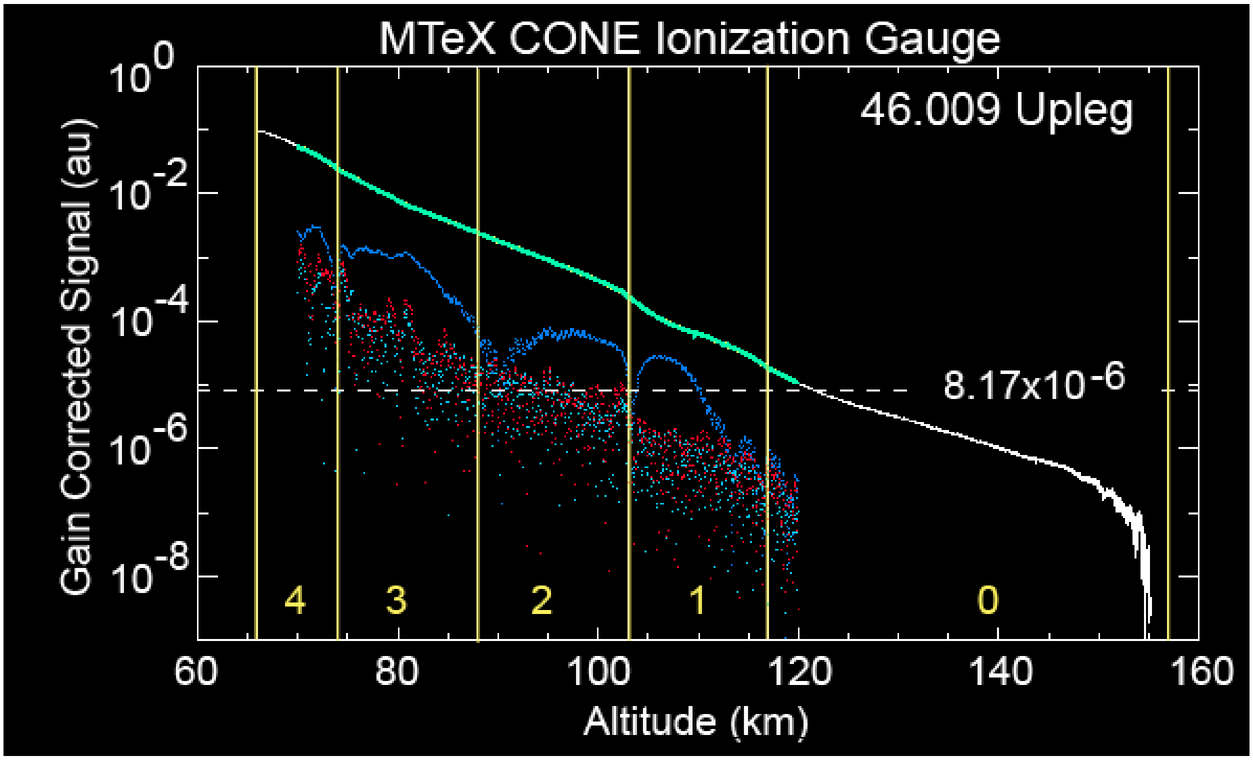

Figure 3.6. The density profile for the upleg of 46.009 of the MTeX investigation. See text for details.

temperature [Leblanc et al., 1998; Thurairajah et al., 2009]. The lidar technique typically uses a constant mean molecular mass of air in its calculations. This value is constant in altitude because the constituents of the atmosphere are well mixed to around 90 km. However, above 90 km the value varies due to changes in the atmospheric composition in the lower thermosphere [Brasseur and Solomon, 1995]. We took constituent profiles from MSIS for 26 January 2015 UT to calculate an altitude varying value of the mean molecular mass of air at 1 km resolution [Hedin, 1991; MSIS, 2016]. The values varied from 28.96 g/mol at 60 km to 26.37 g/mol at 120 km. We then linearly interpolated the profile to the altitude values of the CONE relative density profile, and incorporated these values into the temperature retrieval.

We make two final corrections to the renormalized density profile before calculating the temperature profile. We first remove the effects of spin modulation from the density profile. There is a 2 Hz variation in the CONE measurements due to the payload spinning. We filter the profile with a 0.5 Hz low-pass filter in the log domain to remove this 2 Hz spin contamination from the rocket. We found that without this filtering there is a modulation in the buoyancy frequency profile that is calculated from the derivative of the temperature profile. Second we correct the density profile for ram effects. The MTeX rockets were moving at a speed of ~1000 m/s. In the region of the atmosphere where measurements were taken the rockets are supersonic travelling at ~ Mach 5. At these high Mach numbers there is a piling-up effect in the CONE sensor that increases the density measured by the ion-gauge [Rapp et al., 2001]. This effect is called the ram effect. The CONE density profile must have this effect removed. We used the Rayleigh lidar density data to correct the CONE density profile for each leg of each launch. We did this by comparing the lidar density profile retrieved over the whole night to the CONE density profile in the 70-100 km region. Using the whole night of lidar data, allows us resolve the density profile density up to 100 km. Knowing that the lidar data does not have a ram effect, we calculate the ratio of the CONE density to lidar density. We calculated the ratio by taking averages of the CONE and lidar signals over 5 km altitude intervals and stepping upward by 1 km. This ratio was then normalized so the altitude of smallest ratio was 1. We show the ratios profiles for the upleg in 46.009, the downleg in 46.009, and the downleg in 46.010 in Figure 3.7. We see that the ratio profile behaves similarly for all three legs. The ratio decreases with altitude. This is consistent with the fact that the payload is travelling faster at lower altitudes. The values of the corrections is similar between the legs, and the largest differences are found at the lowest altitude where the payloads are moving fastest and have the greatest differences in their speeds. Having calculated the ram correction at 1 km resolution, we interpolated it to the resolution of the CONE density profile, and divided the CONE density profile by the interpolated correction profile.

We use an initial temperature at 120 km of 347.9 K to seed the three temperature profiles from the CONE data [MSIS, 2016]. We show the temperature profile for the upleg of 46.009 in the top panel of Figure 3.8. We see two mesospheric inversion layers (MILs) near 75 km and 80 km. We see a steady decrease in temperature from 82 km to a mesopause of 140 K at 102 km. From the temperature profile we can calculate the buoyancy frequency using altitude-varying estimates of the acceleration due to gravity and adiabatic lapse rate following Thurairajah [2009]. We show the profile of the buoyancy frequency squared for the upleg in 46.009 in the bottom panel of Figure 3.8.

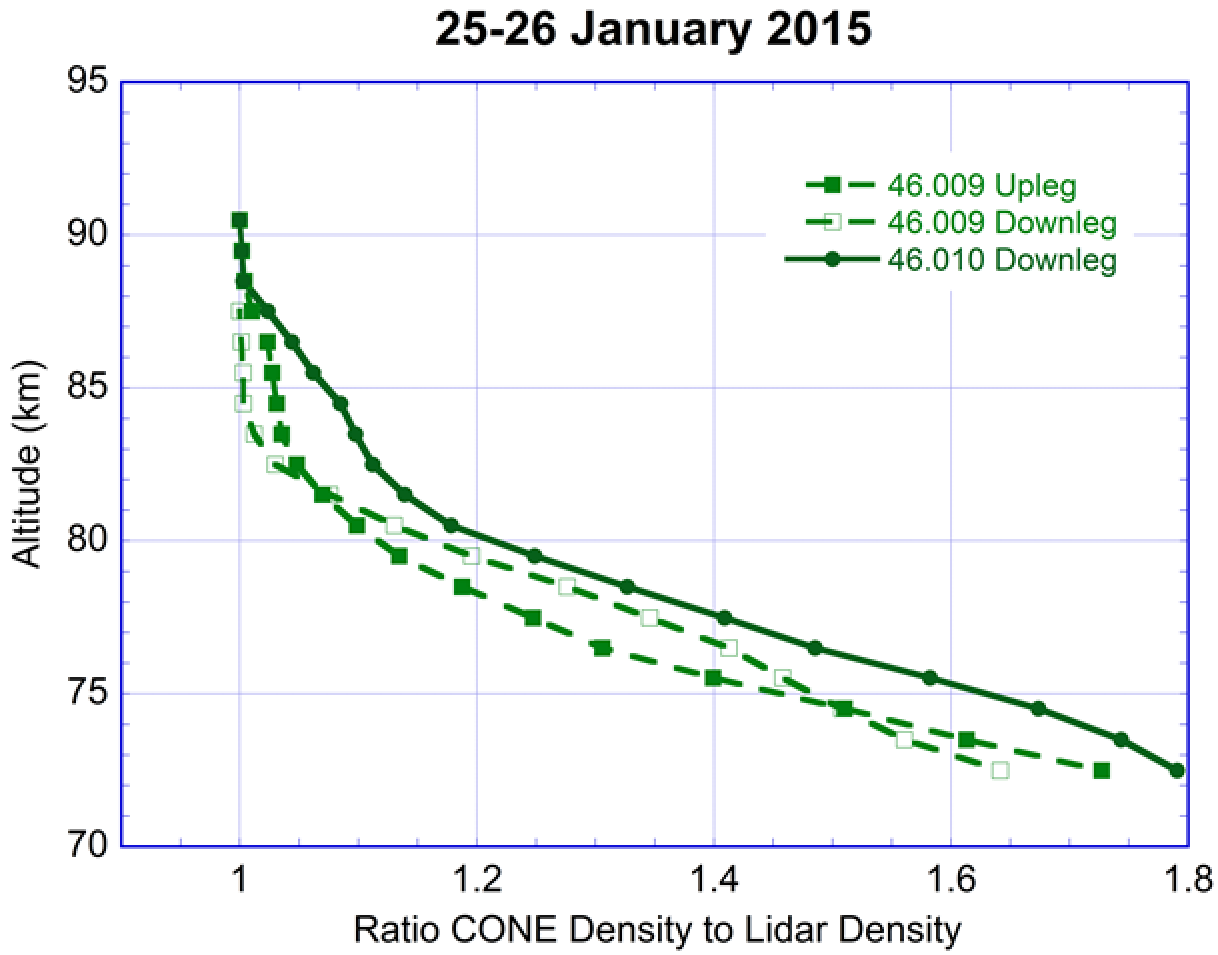

Figure 3.7. Ram corrected ratios for the MTeX investigation.

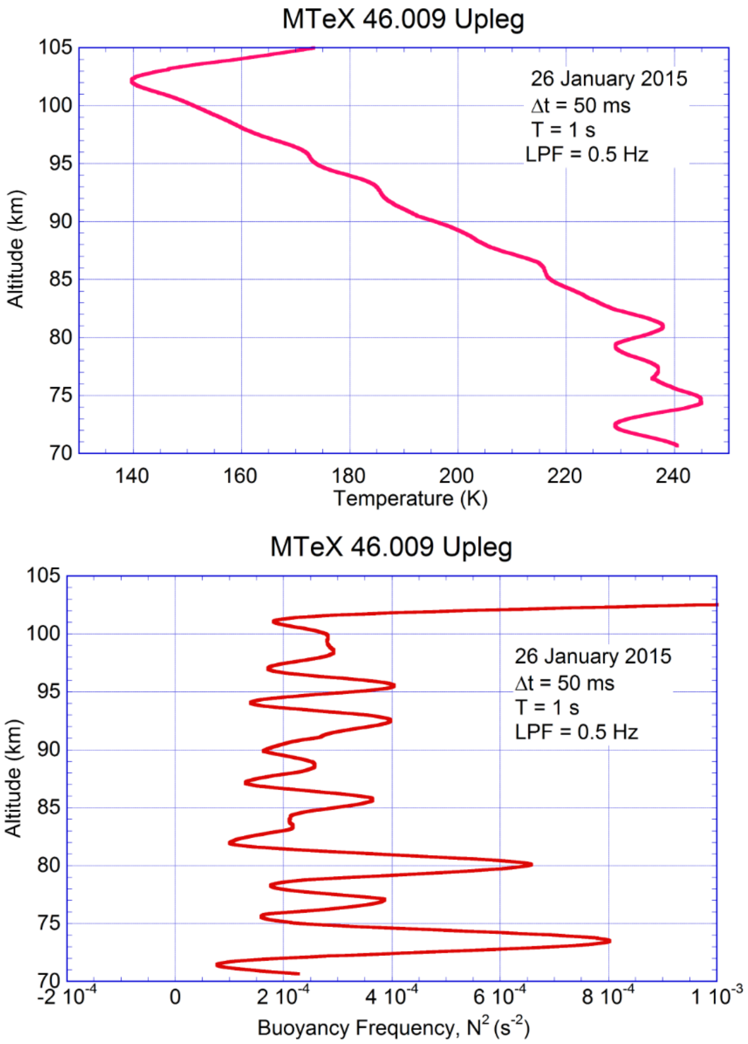

Figure 3.8. Calculated temperature (top) and buoyancy frequency squared (bottom) from the gain-corrected CONE data for the upleg of 46.009. Each profile has approximately 50 m resolution and is calculated from the continuous relative density profile of CONE

We see two regions of high buoyancy frequency squared, indicating enhance stability, near 73 km and 80 km. These regions correspond to the bottomside of the MILs where the temperature increases with altitude. The values of the buoyancy frequency squared remain low (~ 3x10^{-4} s^{-2}) from above the MILs to the mesopause. Having established the density and temperature profiles that define the ambient meteorological conditions we now present our retrieval of the small-scale fluctuations and turbulence characteristics from the CONE measurements.

3.6. Retrieval of small-scale fluctuations from CONE measurements

We calculate the fluctuations following the methodology of Lübken et al. [1993] with some minor changes. Our determination of the small-scale fluctuations is based on the ratio of the electrometer to the emission at the primary CONE instrument resolution of 192 µs resolution. This gives us the highest spatial resolution of ~20 cm. However, the GPS trajectory data was recorded at 50 ms resolution, so we linearly interpolate the 50 ms GPS position data to the 192 µs CONE data in time to provide the altitude of the CONE samples. In each range we subtract the corresponding background signal that was found during the iterative normalization process in Section 3.4 and tabulated in Table 3.5. We carry out all our processing of the CONE data in the time and frequency domain where the data is uniformly sampled. We characterize the fluctuations based on 1-s segments of data that comprise 5029 raw data samples. We show two 1-s segments of the CONE density profile in Figure 3.9. In the top panel of Figure 3.9 we show the density profile measured between 73.4 and 74.4 s after launch corresponding to the 80.3 km to

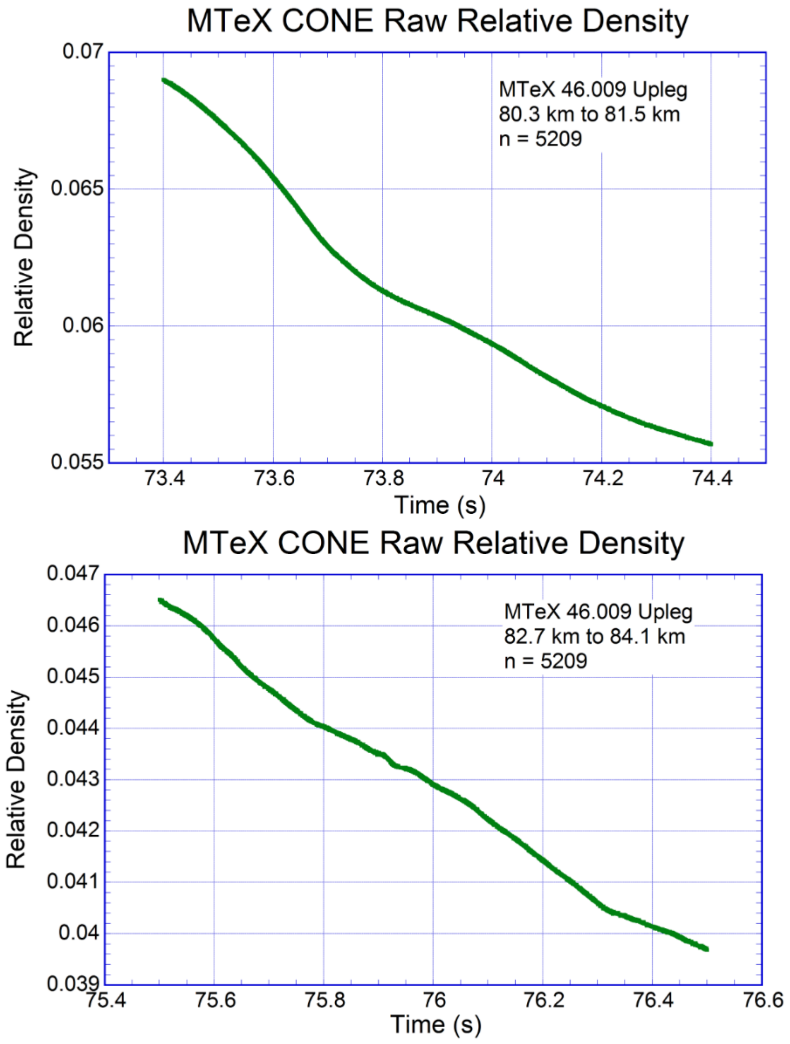

Figure 3.9. An example of raw CONE ratioed data from the upleg in 46.009 in a nonturbuent region (top) and a turbulent region (bottom). The time axis is seconds after turn on of the CONE sensor. Each plot is of 1 s of data comprising of 5209 data points. The times are in seconds after launch.

81.5 km altitude range. This measurement was acquired in range 3 of the upleg of 46.009. We will see later that this is a nonturbulent region. In the bottom panel of Figure 3.9 we show the density profile measured between 75.5 and 74.5 s after launch corresponding to the 82.7 km to 84.1 km altitude range. This measurement was also acquired in range 3 of the upleg of 46.009. We will see later that this is a turbulent region.

Having calculated the CONE density profile in each range, we determine a background profile using the same polynomial fitting and residual method that we used in Section 3.4. In each range we take the log of the profile and fit a third-order polynomial. We then calculate the residual as the difference between the log of the profile and the polynomial, and smooth the residual at 2 km. We add the smoothed residual back to the polynomial and take the exponential to yield the background profile. We then generate the relative density fluctuations, by calculating the difference profile between the density profile and the background profile and dividing the difference profile by the background profile. However, these fluctuations still contain the 2 Hz spin contamination from the payload and must to be removed. We removed this spin contamination by filtering the CONE fluctuation data with a 3 Hz low-pass filter. We then subtract the low-passed filtered fluctuation data from the unfiltered fluctuation data. We plot the two fluctuation profiles for the segments from Figure 3.9 in Figure 3.10. We see that there are relative density fluctuations of about 0.2%. In low-pass filtering the data at 3 Hz we introduce a discontinuity due to Gibbs phenomena at the beginning and end of each range. To avoid including the discontinuities in our estimate of the RMS relative density fluctuations we ignore intervals of one-sixth of a second (i.e., half the period of the 3 Hz filter) at the beginning and end of each range. Finally we low-pass filtered the density fluctuations

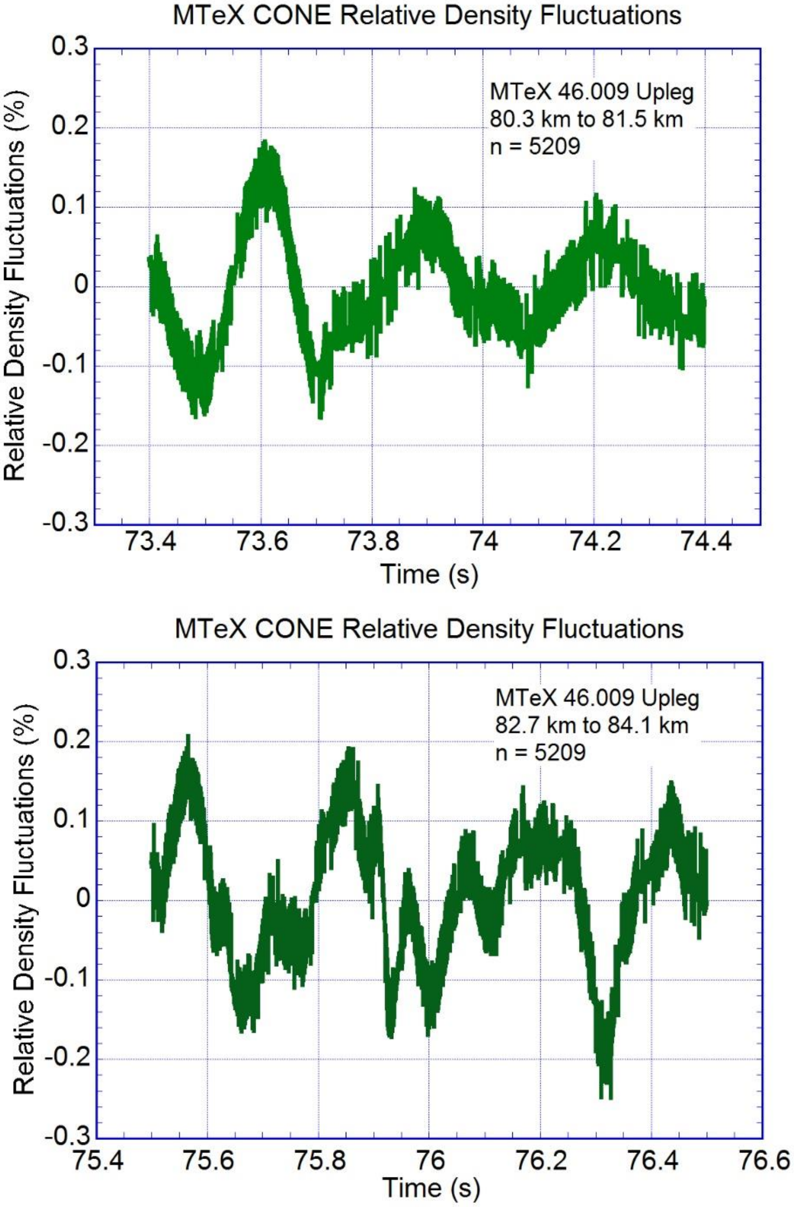

Figure 3.10. Relative density fluctuations for the same data as shown in Figure 3.9. See text for details.

with a cut-off of 20 Hz. We plot the two fluctuation profiles that represent the fluctuations from 3 Hz to 20 Hz, for the segments from Figure 3.10 in Figure 3.11. The value RMS density fluctuation at 80.9 km is 0.06% and the RMS density fluctuation at 83.4 km is 0.08%.

3.7. Estimation of turbulent parameters from CONE measurements

Turbulence is the process of energy cascading from large-scale motions, such as gravity waves, to small-scales where they are dissipated by viscous forces. Richardson first introduced the concept of an energy cascade in the 1920s [Richardson, 1922]. Kolmogorov introduced first formal statistical theory of turbulence came in the 1940s [Kolmogorov, 1941a; b]. Kolmogorov described the spectral properties of turbulence where large-scale eddies breakdown into smaller and smaller eddies until eventually viscous forces dominate and the eddies lose their energy and generate heat. Modern turbulence theory is characterized by randomness, nonlinearity, diffusivity, and dissipation [Tennekes and Lumley, 1972; Kundu and Cohen, 2008]. For a more in-depth discussion of turbulence the reader is directed to Li [2016]. Turbulence is described by a set of parameters. These parameters are the inner scale l_0, the outer scale L_B, and the energy dissipation rate ε. The inner scale is the smallest spatial scale that an eddy can have before it is damped by viscous forces. The outer scale is the largest spatial scale that an eddy can have defined by the buoyancy forces and stability of the large-scale flow. The range of scales between the largest turbulent eddies at the outer scale and the smallest turbulent eddies at the inner scale is called the inertial subrange. The energy dissipation rate is how much energy must flow through the inertial subrange to maintain

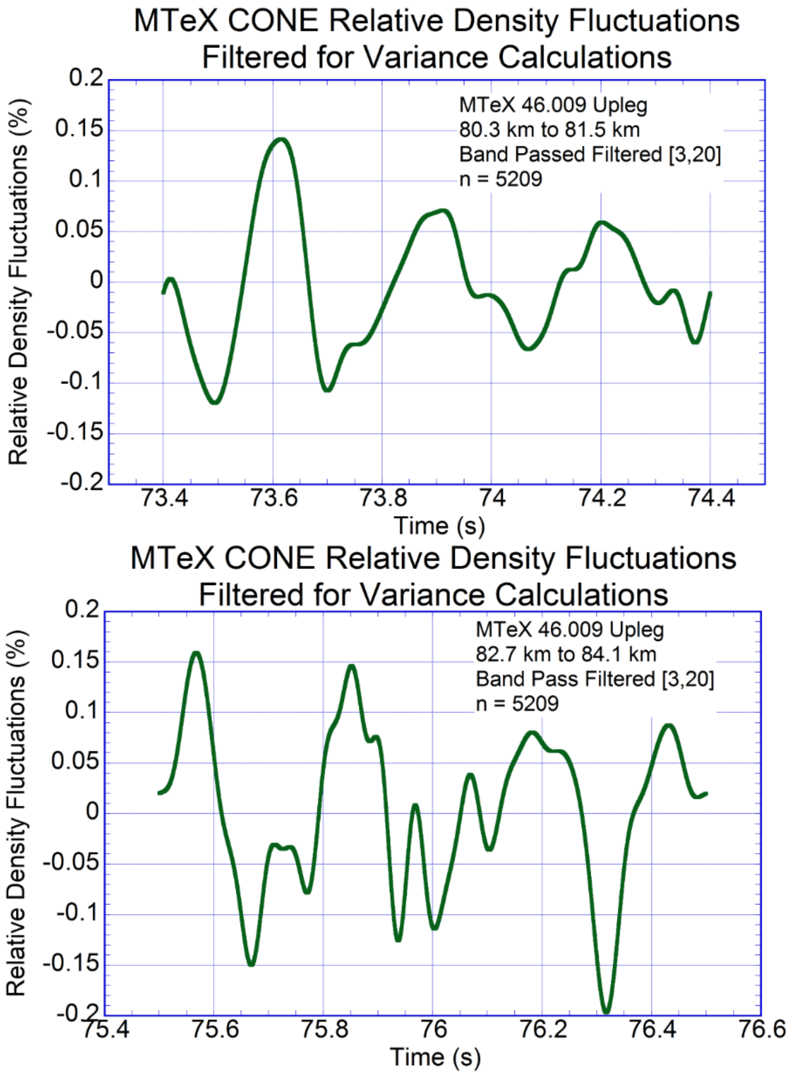

Figure 3.11. Relative density fluctuations filtered between 3 and 20 Hz used to find RMS density fluctuations for the same data from Figures 3.9 and 3.10. See text for details.

the turbulence. As the energy dissipation rate increases the turbulence is more vigorous, turbulent motions extend to smaller scales, and the inner scale decreases. The formal definitions that we use for the scales are given below [Weinstock, 1978; Weinstock, 1981; Lübken et al.,1993],

$$l_0 = 9.90\left(\frac{\nu^3}{\varepsilon}\right)^{\frac{1}{4}} \tag{3.1}$$

$$L_B = 9.97\left(\frac{\varepsilon}{N^3}\right)^{\frac{1}{2}} \tag{3.2}$$

where ν is the kinematic viscosity of air and N is the buoyancy frequency. Equations 3.1 and 3.2 show how each scale is dependent on a scale parameter. l_0 is related to the small scale parameter of dynamic viscosity while L_B is related to the large scale parameter of the buoyancy frequency. These scales represent breaks in the spectra that define the different subranges. The inner scale, l_0, marks where the spectra moves from the inertial subrange to the viscous subrange and L_B shows when the spectra moves from the buoyancy subrange to the inertial subrange. It is the transition defined by l_0 that we will fit to with our turbulence model of choice.

We follow Lübken et al. [1993] and use the Heisenberg model for the turbulent spectra. The Heisenberg spectrum defines the turbulent and viscous subrange, and provides a framework of finding of the energy dissipation by the fitting to a spectrum of fluctuations. It is only dependent on two parameters: ε, and N_Θ. The formulation used by Lübken et al. [1993] is given as,

$$W(\omega) = \left[\frac{\Gamma\left(\frac{5}{3}\right)\sin\left(\frac{\pi}{3}\right)}{2\pi v_r} \right] \frac{a^2 N_\Theta}{\varepsilon^{\frac{1}{3}}} f_a \left[\frac{\left(\frac{\omega}{v_r}\right)^{\frac{-5}{3}}}{\left(1 + \left\{ \frac{\left(\frac{\omega}{v_r}\right)}{k_0} \right\}^{\frac{8}{3}}\right)^2} \right] \tag{3.3}$$

where ω is the angular frequency,

$$\omega = 2\pi f \tag{3.4}$$

and k_0 is the wavenumber associated with the inner scale,

$$k_0 = \frac{2\pi}{l_0} \tag{3.5}$$

and Γ is the Gamma function, v_r is the velocity of the rocket, a is a constant of value 1.74, N_Θ is known as inhomogeneity dissipation rate (which is the rate at which the fluctuations of the tracer Θ are created and disappear due to molecular diffusion), f_a is a constant of value 2 that takes into account different normalizations of N_Θ [Lübken et al. 1993]. The velocity of the rocket is necessary to shift between the temporal frame and the spatial frame, the spatial wavenumber k, is given as,

$$k = \frac{\omega}{v_r} \tag{3.6}$$

We reviewed the formulation of the Heisenberg turbulence model and found that N$_\Theta$ not independent of ε. If we used Equation 3.3 to fit to the spectrum and treated N$_\Theta$ and ε as independent our fits could be biased so we defined a new variable, Ñ$_\Theta$,

$$\tilde{N}_\Theta = \frac{N_\Theta}{\varepsilon} \tag{3.7}$$

We now rewrite Equation 3.3 with Equations 3.1 and 3.5-3.7 to arrive at our formulation of the Heisenberg spectral model in terms of wavenumber, and the parameters, Ñ$_\Theta$ and ε,

$$W(k) = A\tilde{N}_\Theta \varepsilon^{\frac{2}{3}} k^{\frac{-5}{3}} \left[\frac{1}{\left(1 + bk^{\frac{8}{3}} \varepsilon^{\frac{-2}{3}}\right)^2} \right] \tag{3.8}$$

Here the constants have been all combined in constants A and b, where the constant A is given as,

$$A = \frac{a^2 f_a \Gamma\left(\frac{5}{3}\right) \sin\left(\frac{\pi}{3}\right)}{2\pi v_r} \tag{3.9}$$

and the constant b is given as,

$$b = \left(\frac{9.90}{2\pi}\right)^{\frac{8}{3}} \nu^2 \tag{3.10}$$

Equation 3.8 is the same as 3.3 but with an independent Ñ$_\Theta$. It also highlights the expected Kolmogorov energy spectrum relation in the internal subrange of k$^{-5/3}$ and ε$^{2/3}$.

A smooth transition into the k^{-7} relation expected in the viscous subrange is also evident in this form of the model.

To fit the Heisenberg model to the spectrum of the fluctuations we first apply a Von Hann window to the fluctuations over a 1 s interval and then take the Fast Fourier Transform (FFT) [Harris, 1978]. The Von Hann window limits the spectral leakage from edge effects of the FFT. The 1 s interval results in a frequency resolution of 1 Hz and a maximum frequency of 2604 Hz. We then carry fit the Heisenberg Model to the spectra. We then move to the next 1 s interval centered on the next 50 ms point defined by the GPS position. This gives us overlapping 1 s intervals to characterize the turbulence every 50 ms that correspond to a given temperature and buoyancy frequency found in Section 3.5. We then calculate ε following six steps,

1. A spectral background is calculated as the average power seen at frequencies greater than 1000 Hz and is subtracted from the spectrum.
2. The minimum frequency is the frequency with the highest power between 4 and 10 Hz. This minimum frequency was chosen to avoid possible contamination from the removed 3 Hz background.
3. The maximum frequency is found by locating the highest frequency that is at least one order of magnitude above the noise in that spectrum. The frequency with the minimum power in the range 5 Hz before and 5 Hz after this highest frequency is the maximum frequency.

4. We calculate the angular frequencies using Equation 3.2 and then use the IDL procedure “curvefit” to fit to the log of the spectrum. This procedure uses a gradient-expansion algorithm to compute a nonlinear least squares fit and used three functions that we define: the Heisenberg Model, the derivatives of the Heisenberg model in ε and the derivative of the Heisenberg model in $\tilde{N}_{\Theta}$ (in the log domain).
5. The initial frequency guess is stepped from the minimum frequency (Step 2) to the maximum frequencies (Step 3) in 1 Hz increments.
6. For each initial guess the algorithm convergence state and the RMS error is recorded.

These steps are the same steps adopted by Szewczyk [2015]. We then apply the following three conditions to ensure that our fit is significant,

1. The fit that converged and has the lowest RMS error is checked to make sure that the frequency of best-fit falls in the frequency range between the minimum and maximum frequencies. If it falls outside this frequency range the fit is rejected.
2. The outer scale found must be larger than the inner scale. If the inner scale is greater than the outer scale the fit is rejected.
3. The integrated power spectrum of the model fit must be over 50% of the integrated power spectrum of the fluctuations.

Condition 1 is adopted from Szewczyk [2015] while conditions 2 and 3 are added for our method. We added condition 2 to account for two unphysical situations: when the outer scale is equal to or less than the inner scale or when the outer scale is infinitely large.

The first situation would mean that the smallest scales are equal to or larger than the largest scales. The second situation means that all large scale flows are within the inertial subrange. However a critical assumption of turbulence theory is that energy is only transferred through the inertial subrange. If there is no source region there can be no turbulence.

These eight conditions give us the best estimates of ε for all altitudes during the MTeX investigation. We thus create an altitude profile of ε that can be compared to the meteorological conditions. We plot the spectra for the fluctuations for the two regions of Figure 3.9 in Figure 3.12. In Figure 3.12 we see spectra where the fitting algorithm fails (upper panel) and the fitting algorithm succeeds (lower panel) corresponding to the intervals that we have shown earlier in Figures 3.9, 3.10, and 3.11. The fitting algorithm fails to converge for the fluctuations at 80.9 km despite the fact the RMS density fluctuations are of similar value at 80.9 km and 83.4 km.

3.8. Upgrade of Rayleigh lidar system

For the MTeX investigation we upgraded the Rayleigh lidar system at the Lidar Research Laboratory at Poker Flat Research Range in Chatanika, Alaska (64° N, 143° W). A full description of the original Rayleigh lidar system can be found in Irving [2012]. Our goal was to increase the altitude range of the measurements and obtain measurements lower in the stratosphere and higher in the mesosphere than we had previously obtained. The Rayleigh lidar was a single-channel system with a temperature and density measurement altitude range of 40 km to 80 km [Thurairajah et al. 2009;

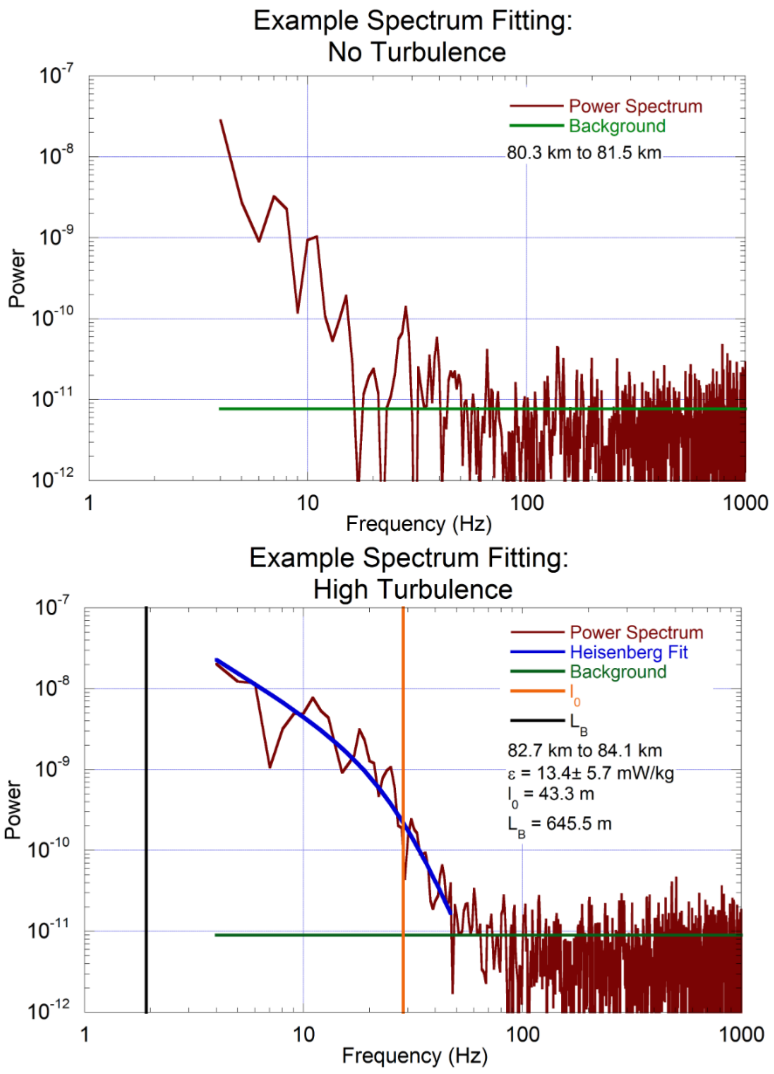

Figure 3.12. Power Spectra in frequency of the same altitudes from Figures 3.9 with turbulent fitting shown in the bottom panel where turbulence was found. See text for details.

2010a; b; Irving et al., 2014]. The dynamic range of the single-channel Rayleigh lidar system defined the measurement altitude range. Below 40 km the signal is too high and results in a non-linear response in the detectors. Above 80 km the signal-to-noise ratio is too low. We can decrease the lower altitude of the measurement by reducing the signal (for example by decreasing the laser pulse energy or decreasing the telescope area) but this would also decrease the upper altitude. We can increase the lower altitude of the measurement by increasing the signal (for example by increasing the laser pulse energy or increasing the telescope area) but this would also increase the upper altitude. Thus we decided to upgrade the Rayleigh lidar into a dual-channel system. Furthermore, we needed to extend the scope of the data acquisition system to allow real-time calculation of temperature profiles so that we could call the MTeX rocket launches based on the appearance of a MIL. This required changes in both the system hardware and software.

A dual-channel system is based on extending the dynamic range of the system by splitting the light received by the telescope between two channels with independent detectors. Thus the receiver system includes a low-altitude channel where a portion of the returned light (typically 10-20%) is split using a beam-splitter to a detector, and a high-altitude where the remainder of the light (80-90%) is reflected by a mirror to a detector. In order to increase the signals in the high-altitude channel we increased the size of the telescope, replacing the original 60 cm telescope with a 1.04 m telescope. We also decided to have three receiver channels that would support a dual-channel Rayleigh system operating at 532 nm, and an independent single-channel resonance lidar system that could operate at other wavelengths (e.g., 589 nm, 372 nm, and 337 nm). We show a schematic of the dual-channel Rayleigh lidar system in Figure 3.13. A dichroic beam

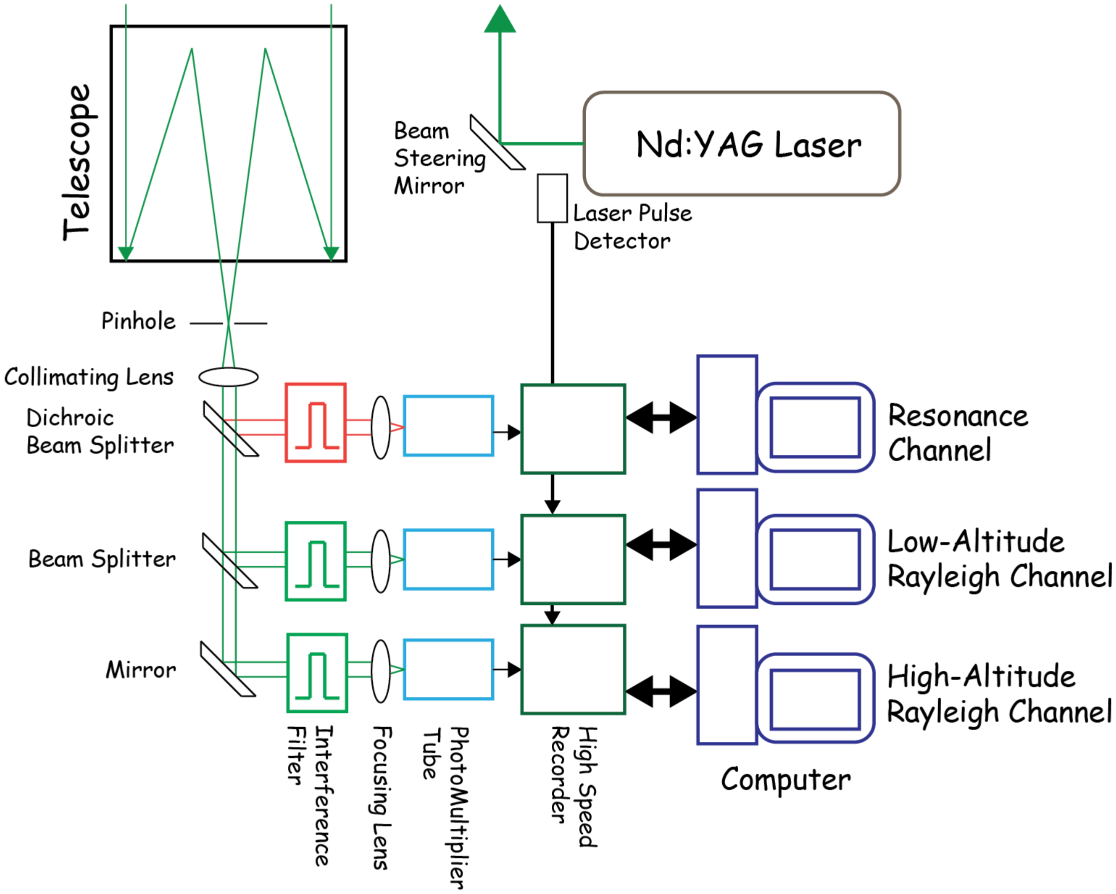

Figure 3.13. Schematic diagram of the new dual-channel Rayleigh lidar system at PFRR. The upper receiver channel is for a resonance lidar system also at PFRR.

splitter separates the two wavelengths, 523 nm and 589 nm, so that the resonance lidar system uses the first channel and the Rayleigh lidar system uses the second and third channel. The Rayleigh lidar channels are designated the low-altitude channel (RL) and the high-altitude channel (RH). The Rayleigh lidar receiver channels are synchronized to the Nd:YAG laser transmitter. The resonance receiver channel is synchronized to a dye laser transmitter (not shown for clarity). For the MTeX investigation the receiver included both a sodium resonance lidar operating at 589 nm and the Rayleigh lidar system operating at 532 nm. The beam-splitter was a nominal 80/20 splitter, transmitting 80% of the incident light and reflecting 20%. The Nd:YAG laser was the same “Power Lite 8020” laser (Continuum Laser, Santa Clara, USA) that was used in the original system. This pulsed laser operates at a wavelength of 532 nm and 20 pulses per second with an average power of 7.1 W. In fall of 2014 we had attempted to upgrade the transmitter to a “Power Lite 9030” laser (Continuum Laser, Santa Clara, USA). This pulsed laser operates at a wavelength of 532 nm and 30 pulses per second with an average power of 21 W. However, the “Power Lite 9030” proved unstable, losing energy over several hours of operation, and we could not use it as a lidar transmitter. We also upgraded the high-speed recorders and computer systems. We replaced the original Ortec Turbo T914 Multichannel Scaler (MCS) (EG&G, Wellesley, USA) recorders with SR430 MCS (Stanford Research Systems, Sunnyvale, USA) recorders. The new T914 MCS recorders were designed in the early 1990s to operate in a direct memory-mapped mode, and could not operate with contemporary computers and operating systems. The SR430 recorders were designed to operate under GPIB control and could interface with LabView™ software (National Instruments, Austin, USA). We replaced the 1990s-era computers with contemporary computers with Windows 7™ (Microsoft Corporation, Redmond, USA) operating system hosting LabView. We also installed Interactive Data Language™ (IDL) (Harris, Melbourne, USA) on the computer. The new computers allowed us to both simultaneously acquire lidar data (using LabView-based programs) and analyze that data (using IDL-based programs). We streamlined our IDL program software to allow real-time calculation of temperature profiles. This was critical for the MTeX investigation. Without the real time analysis capability, we could not have monitored the MILs in the atmosphere and made the launch decision in response to the presence of the MIL.

The lidar data was acquired in our established fashion. When the laser fires the MCS is triggered to record the atmospheric echo from the laser pulse. The echo is recorded at 48 m resolution from the ground to an altitude of 197 km (4096 points in altitude). The integrated echo from 1000 laser pulses is recorded by the MCS unit and transferred to the computer. The raw profiles are saved sequentially, eight at a time, into a raw data file. Each sequence of eight profiles is called a set. Each data file takes about 7 minutes to acquire. At the end of each file the data acquisition pauses until the operator tells the computer to begin acquiring the next set. This pause allows the operator to respond to any problems in the lidar system (e.g., drift in laser alignment and loss of power) before continuing to acquire further data.

We show the lidar signals that we acquired on 25-26 January 2016 with the new dual-channel Rayleigh lidar system in Figure 3.14. These signals are integrated over the whole night of observation from 1827 LST to 0715 LST (0227- 1615 UT). On the night of 25-26 January 2016 we set up the data acquisition to acquire eight profiles per set, and acquired 112 sets of data. Due to errors in communication between the computer and

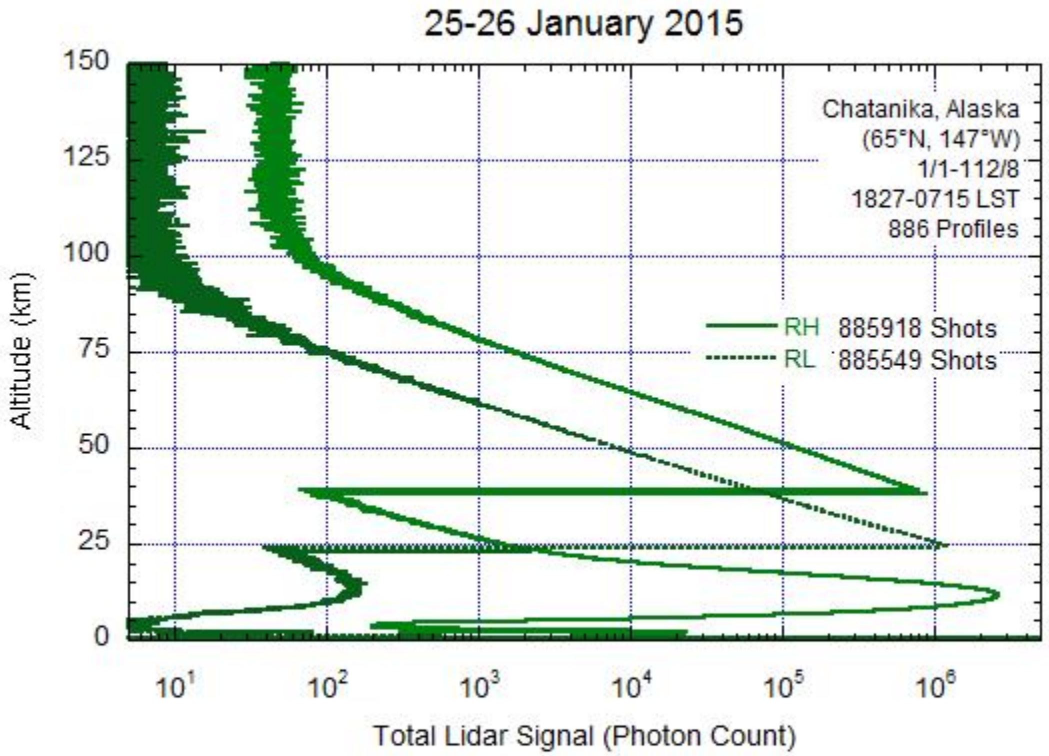

Figure 3.14. Lidar signal profiles for data taken on 25-26 January 2015 for the MTeX investigation. See text for details.

the MCS units, some of the profiles ended before 1000 laser pulses (operationally termed shots) had been recorded, and some of the sets ended before 8 profile had been recorded. Thus we expected to acquire 112 sets of data with 896 profiles based on 886,000 laser pulses.   The high-altitude signal actually represents the integration of 886 profiles based on 885,918 laser pulses. The low-altitude signal actually represents the integration of 886 profiles based on 885,549 laser pulses. We see that the gain of the low-altitude channel is electronically switched at 150 μs to avoid overloading of the receiver by signals below 22.5 km. The gain of the high-altitude channel is electronically switched at 250 μs to avoid overloading of the receiver by signals below 37.5 km. We see that the lidar signal decreases with altitude and above 100 km the atmospheric echo is negligible and the lidar signal is dominated by the background signal due to skylight that is constant with altitude. We see that the lidar signal in the high-altitude channel extends to approximately 100 km, while the lidar signal in the high-altitude channel extends to approximately 90 km. The lidar signal in the high-altitude channel is approximately 10 times larger than the signal in the low-altitude channel.

We compare the basic performance of the new Rayleigh lidar system with the original system by examining the lidar signals integrated over the whole night of 25-26 January 2016 and comparing them with observations made with the original system during the Turpopause experiment on the night of 17-18 February 2009 [Collins et al., 2011]. We present the results in Table 3.6. On 17-18 February 2009 the single-channel Rayleigh lidar system operated from 1827 LST to 0715 LST (327-1515 UT) and the integrated lidar signal represented the echo from 736,000 laser pulses. The average laser power was 8.2 W. We determine the total lidar signal over the altitude 60-65 km

Table 3.6: Rayleigh Lidar Performance.

Date	Time (LST)	Laser Pulses	Lidar Signal[1]			
			Total 60-65 km	Total 170-175 km	Signal 60-65 km	Signal per Laser Pulse
17-18 February 2009	1947-0711	736,000	3.88×10^{5}	5.68×10^{2}	3.87×10^{5}	5.26×10^{-1}
25-26 January 2015	1827-0715	885,918	1.55×10^{6}	4.89×10^{3}	1.55×10^{6}	1.74×10^{0}
		885,549	9.13×10^{4}	5.85×10^{2}	9.08×10^{4}	1.02×10^{-1}

[1]: Lidar signals are given in photon counts. Signal per laser pulse is given in photon counts per pulse.

and 170-175 km altitude. The total lidar signal at 60-65 km represents the sum of the lidar signal from the atmospheric echo altitude and the background signal. The total lidar signal at 170-175 km represents the background signal. We subtract the background signal from the total lidar signal at 60-65 km to get the lidar signal from the atmosphere. We then normalize the signal by the number of laser pulses to get a per pulse measure of the lidar signal. We see that the high-altitude channel yield signals that are 17 times larger than the low-altitude channel, and 3.3 times larger than the single-channel system. The telescope upgrade from a 60 cm telescope to a 1.04 m telescope would yield a signal increase of a factor of 3.0. However, the decrease in average power from 8.1 W to 7.1 W would yield a signal decrease of a factor of 0.88. Thus we would expect an increase of a factor of 2.6. The apparent larger gain in lidar signal by a factor of 1.3 (= 3.3/2.6) can be attributed to the following combination of effects: differences in the reflectivity of the telescope, differences in sky conditions, careful optical alignment of the new receiver before the MTEX investigation, differences in gain in the photomultiplier tubes, and differences in the transmission of the optical interference filters.

We also compared the performance of the low- and high-altitude channels by examining the lidar signals at corresponding altitudes and corresponding sets. We integrated the lidar signal over 11 5-km intervals starting at 40-45 km and ending at 90-95 km. We plot the signals in Figure 3.15. We see that the two channels show the best agreement at 60-65 km. At lower altitudes (50-55 km and below) the high-altitude channel signals are biased low due to overloading of the detectors [Irving, 2012]. At higher altitudes (80-85 km and above) the low-altitude channel signals are scattered due to the statistics of the detection process which have a Poisson distribution [Papoulis, 1984].

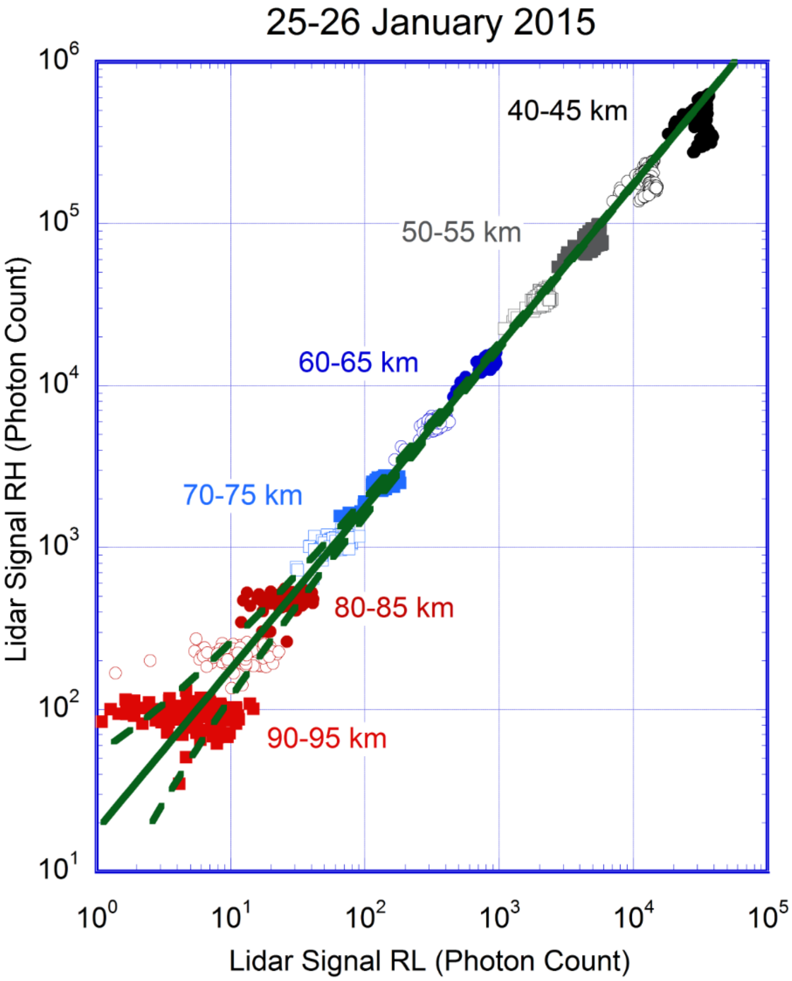

Figure 3.15. Plot of high altitude channel signal (RH) and low altitude channel signal (RL) on the night of 25-26 January 2015.

Poisson random variables have a variance equal to their mean, and so as the expected signal decreases the relative scatter in the data increases.

We now demonstrate the performance of the upgraded lidar system in terms of the temperature measurements derived from the lidar signals over the whole night. We calculated the temperature from the lidar signal following standard Rayleigh lidar technique that assumes hydrostatic equilibrium (e.g., Thurairajah et al. [2009; 2010a; b]). For the high-altitude channel we used an initial temperature estimate at 90 km from the CONE instrument. For the low-altitude channel we used an initial temperature estimate at 65 km from the high-altitude temperature profile. We plot both the high-altitude and low-altitude temperature profiles in Figure 3.16. We see that below 60 km the high-altitude temperature profile departs significantly from the low-altitude temperature profile, and the differences increase as the altitude decreases. The apparent higher values of the high-altitude temperatures at lower altitudes is expected due to increasing signal loss at lower altitude. This increasing signal loss with decreasing altitude yields a longer scale height in the high-altitude lidar signal profile than the low-altitude lidar signal profile. Thus the high-altitude density profile has a longer scale height than the low-altitude density profile. Thus under the assumption of hydrostatic equilibrium the atmosphere as measured by the high-altitude channel appears (incorrectly) warmer than that measured by the low-altitude channel of the lidar system. The final temperature profile is a composite profile based on both the high-altitude and low-altitude profile. We truncate both profiles at 61 km, the high-altitude profile represents the temperatures from 61 km to 90 km and the low-altitude and the low altitude profile represents the temperatures from 35 km to 61 km. We now compare the errors in the temperature measurements of

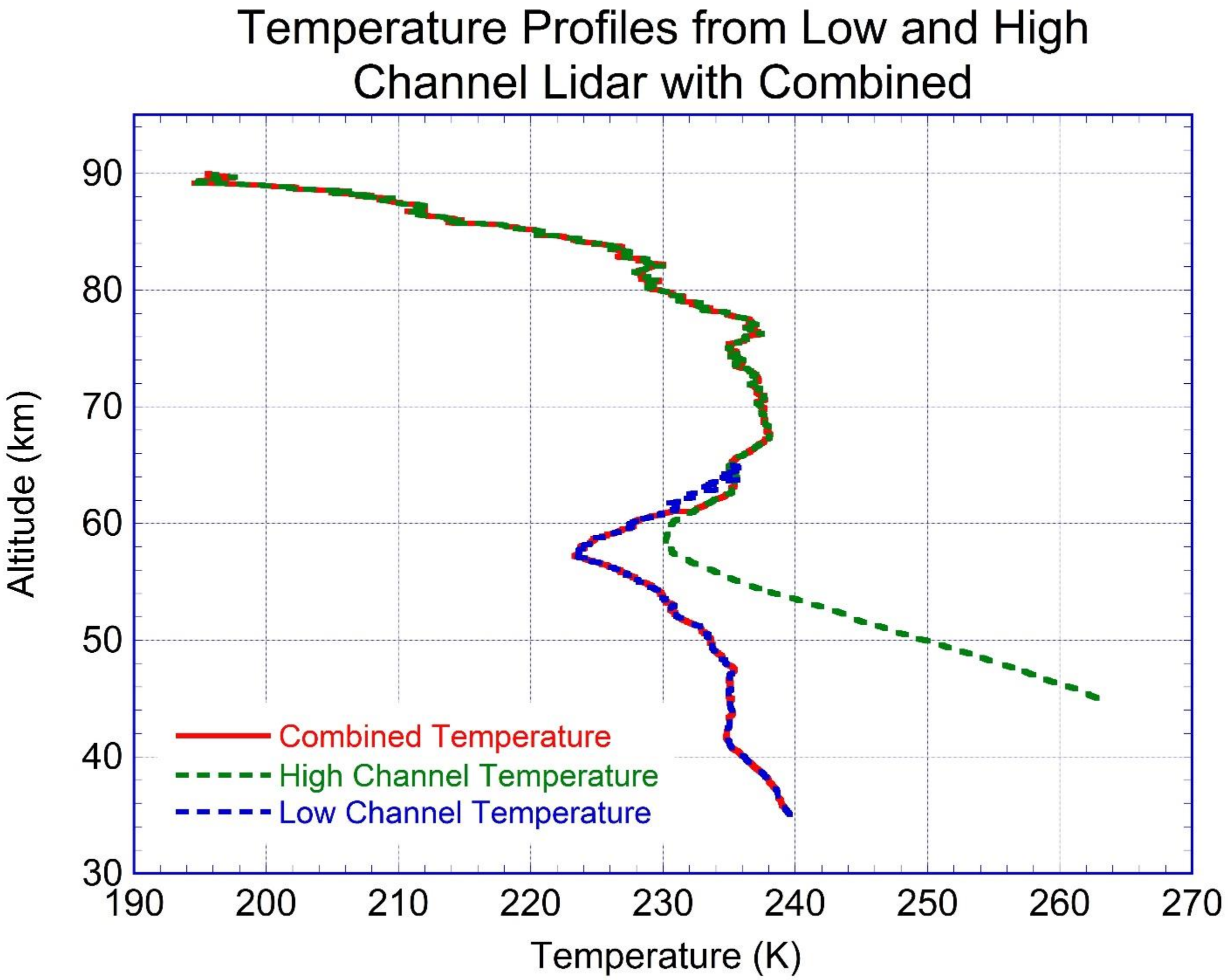

Figure 3.16. Nightly temperature profile for 25-26 January 2015 measured by the Rayleigh lidar. The high altitude channel, low altitude channel as well as the combined are shown.

the MTeX and Turpopause experiments [Lehmacher et al., 2011]. We present the results in Table 3.7. We see that below 61 km, where the MTeX temperatures are based on the low-altitude channel, the MTeX measurements have twice the error of the Turbopause measurements. We see that above 61 km, where the MTeX temperatures are based on the high-altitude channel, the MTeX measurements have half the error of the Turbopause measurements. We note that the error in the MTeX measurements at 88 km is 3.5 K, the same as the Turbopause measurement at 80 km. Thus we summarize the improvement in the temperature measurements at high altitude as follows: the upgraded lidar system yields temperature measurements with half the error of the original system, and extends the temperature measurements by an altitude of 8 km.

3.9. Summary and conclusions

In this Chapter we have presented the retrieval of the CONE measurements for meteorological and turbulent measurements as well as the upgrade of the Rayleigh lidar system. We have seen that in order to get a continuous density profile from the CONE data an iterative fitting method was applied. This method allows for the use of density continuity arguments to be the main fitting parameter as well as giving us the smoothest profile possible. This is a new method created during the course of this study that allowed for an independent look at the CONE instrument.

We have described a new fitting method for the Heisenberg model of turbulence. In it we find a background over a whole range in the CONE data and filter it to remove the 2 Hz spin of the rocket. This gives us a measure of the density fluctuations which we then fit to the Heisenberg model giving a direct measurement of the energy dissipation rate at each 50 ms step.

Lastly, updates to the Rayleigh lidar system at PFRR have increased the altitudes that can be studied by the Rayleigh lidar as well as the vertical resolution. This update has given us the highest quality data for this lidar system to date.

Chapter 4 The Mesosphere-Lower Thermosphere Turbulence Experiment

4.1. Introduction

The Mesosphere-Lower Thermosphere Turbulence Experiment (MTeX) was a sounding rocket investigation to study turbulence in well-defined meteorological conditions. At the core of the MTeX investigation was a rocket-based neutral density sensor, CONE as described in Chapter 3. Mesospheric Inversion Layers (MILs) were chosen for the well-defined meteorological condition studied by MTeX because of their temperature structure and the long-term studies already done on MILs at Poker Flat Research Range (PFRR) [Irving et al., 2014]. MILs consist of a stable positive bottomside temperature gradient and an unstable negative topside temperature gradient. The bottomside temperature gradient leads to increasing buoyancy frequencies. These higher buoyancy frequencies can cause high-frequency gravity waves to break. The topside temperature gradient can be near-adiabatic and indicates the presence of convective instability.

On the night of 25-26 January 2015 two Terrier-improved Malemute rockets (46.009 and 46.010) were launched at 0013 AKST (0913 UT) and 0046 AKST (0946 UT) from PFRR, Chatanika, AK (64º N, 143º W). The trajectories and details for these launches were already presented in Chapter 3. We use the two CONE instruments onboard the MTeX rockets in conjugation with satellite, reanalysis, and Rayleigh lidar data to get a complete view of meteorological conditions on the night. In this Chapter we discuss data taken by the Sounding of the Atmosphere using Broadband Emission Radiometry (SABER) instrument aboard NASA’s Thermosphere Ionosphere Mesosphere Energetics Dynamics (TIMED) satellite, Modern-Era Retrospective analysis for Research and Applications (MERRA) reanalysis data, Rayleigh lidar data, and CONE data. The SABER data allows us to characterize the large-scale planetary wave activity. The MERRA data allows us to characterize the winds and ΔNBE. Rayleigh lidar data gives us the temperature and gravity wave activity. CONE data gives us the temperature, atmospheric stability, and turbulence. The combination of all these data sets provides us with a complete view of the atmospheric dynamics from the largest to the smallest scales.

4.2. Synoptic scale meteorology from satellite and reanalysis data

SABER uses a multi-channel radiometer for limb infrared atmospheric emissions. A total of ten channels from 1.27 μm to 17 μm are available. These channels provide data on vertical distributions of temperature, pressure, and some chemical species such as CO_2, O_3, OH, and NO [Mertens et al., 2002]. In Figure 4.1 we plot the geopotential height perturbations (contours) and overplot the temperature gradients (shaded regions) using Level 2A version 2.05 SABER data [Remsberg et al., 2008]. The left panel shows the geopotential height perturbations in altitude and longitude for the night of the MTeX investigation. The right panel shows the geopotential height perturbations in altitude and latitude on the night of the MTeX investigation. PFRR is located at the dashed vertical line in both panels. These geopotential height perturbations are interpreted as planetary wave activity of wave number 1 where we see a perturbation with a single cycle in longitude around the globe. There is a positive phase over North America and the Atlantic and a negative phase over Eurasia. The wave propagates westward with altitude as expected for planetary waves (see Figure 2 of Irving et al. [2014] for comparison). However, there are regions where the phase of the wave changes abruptly and there is

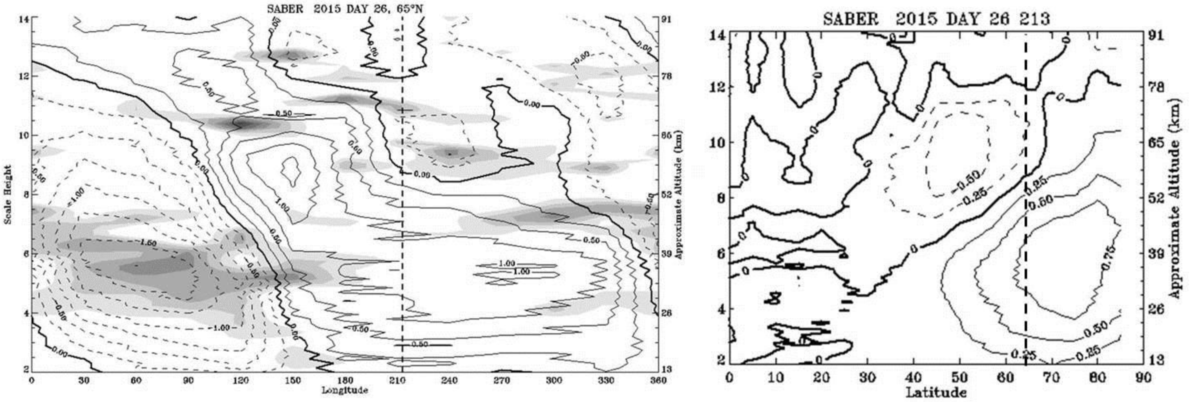

Figure 4.1. SABER derived geopotential perturbations for 26 January 2015. Poker Flat Research Range is indicated by the vertical dashed lines. The left panel shows the geopotential height perturbations in altitude versus longitude. Dark regions are temperature gradients in 1K/km. The right panel show the geopotential height perturbations in altitude versus latitude. For both panels solid contours are positive, bold contour is zero value, and dashed contours are negative.

a temperature inversion (e.g., near 60 km just east of PFRR). This combination of a phase change and MIL is indicative of planetary-wave breaking [Irving et al., 2014]. We will see later in the Section 4.3 that the locations of the MILs near 60km, 70 km and 80 km are consistent with those seen by the Rayleigh lidar. In the right panel of Figure 4.1 we also see evidence of planetary wave breaking. The positive phase of the wave changes abruptly reversing near 50 km rather than extending upward into the mesosphere (see Figure 2 of Irving et al. [2014] for comparison). The SABER data represents a composite over a day indicating wave-breaking and the MILs in Figure 4.1 are persistent meteorological features. This planetary-wave breaking is also consistent with the sudden stratospheric warming (SSW) that occurred in early January 2015 [Manney et al., 2015]. While the 2015 SSW was characterized as minor, it resulted in changes in trace gases and temperature and a splitting of the stratospheric vortex that are characteristic of a major stratospheric vortex. The SSW in 2015 highlights ongoing discussion about how disturbance in the stratosphere are characterized.

In Chapter 2 we saw that structure of the winds is a critical factor in the control of gravity wave activity. We calculate gradient winds from the SABER data. These winds represent the wind averaged over all longitudes. We show the gradient winds in the latitude band from 20° N to 80° N in for 26 January 2015 in the left panel of Figure 4.2. Again we indicate PFRR by the vertical dashed line. The wind speeds are between 10 and 30 m/s. For comparison, we show the MERRA instantaneous reanalysis zonal wind speed for 25-26 January 2015 at 6 UT over PFRR in the right panel of Figure 4.2. The MERRA winds peak at 11 km with a speed of maximum of 20 m/s. The wind decreases to 0 m/s at 36 km. The wind peaks locally at 54 km with a speed of -10 m/s.

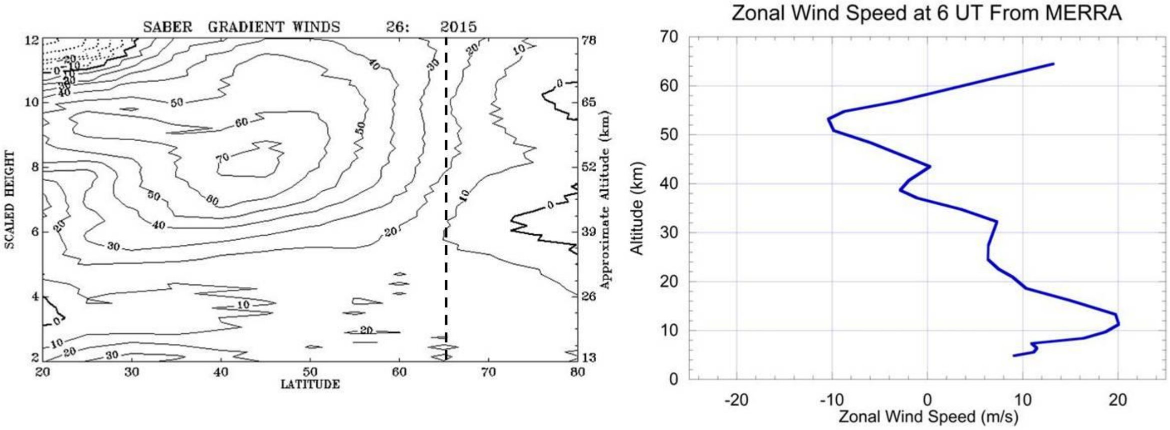

Figure 4.2. Gradient winds as calculated by SABER data on the night of 25-26 January 2015 (left) and zonal wind speed from MERRA reanalysis for 6 UT 26 January 2015 over Chatanika, Alaska (right). Left panel Solid (dotted) contours are westerly (easterly) winds. These winds are averaged over all longitudes for the latitudes 20° N to 80° N

Above 54 km the wind goes westward to eastward with a speed of 10 m/s at 64 km. The MERRA winds show that above the jet stream in the troposphere the wind weakens with a zero wind line at 36 km. Both the SABER and MERRA wind speeds in Figure 4.2 are low. This means that the gravity waves generated by the jet will be blocked before they reach the 70-102 km altitudes that CONE observes and we expect low levels of gravity wave activity in the mesosphere and lower thermosphere.

Since we expect that the winds will suppress gravity wave activity, we calculate the ΔNBE to see there is significant ageostrophic flow in the middle atmosphere that will enhance the gravity wave activity. Following our approach in Chapter 2 we calculate the ΔNBE at each altitude averaged over the 800 km radius circle centered on PFRR. We plot the ΔNBE profile for 06 26 January 2015 UT in Figure 4.3. The highest values for ΔNBE are $6.5\text{x}10^{-9}$ s^{-2} at ~8 km. The value of ΔNBE decreases above this altitude and has a new maximum of $2.7\text{x}10^{-9}$ s^{-2} at 48 km. The value of ΔNBE never reaches the $4\text{x}10^{-9}$ s^{-2} used by Hoffmann et al. [2013] as a threshold for gravity wave generation. The values for ΔNBE in Figure 4.3 are similar to the lowest values found in February 2009 in Chapter 2 (Figure 2.10). Thus on the night of the MTeX investigation we expect that the combination of weak winds and low levels of ageostrophy should yield low levels of gravity wave activity in the middle atmosphere.

4.3. Local meteorology from Rayleigh lidar

The Rayleigh lidar was operated from 1827 LST to 0714 LST on the night of 25-26 January 2015. The raw lidar profiles were acquired over 50 s intervals. In order to

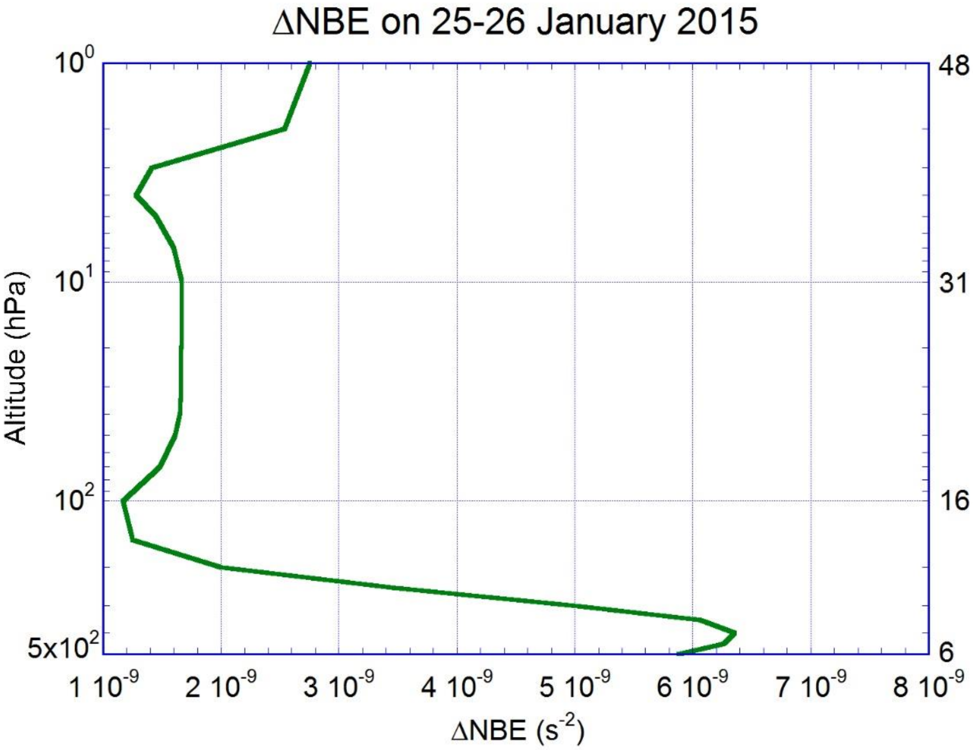

Figure 4.3. ΔNBE in altitude over PFRR for the MTeX investigation. It is plotted over the same values as Figure 2.10 in Chapter 2 for comparison.

produce accurate temperature and density profiles we integrate the raw lidar profiles. Three different integration intervals are used in our analysis. First, we integrate over the whole night to provide background profiles of temperature and density for determining the buoyancy frequency and relative density fluctuations respectively. Second, we integrate over two hour periods at successive 15 minute steps for determining temperature and density profiles and investigating the characteristics of MILs and longer-period gravity waves. Third, we integrate over 30 minute periods at successive five minute steps for determining density profiles and investigating the characteristics of shorter-period gravity waves. The integration is centered on the hour, yielding nominal samples on regular 15- and 5- minute centers and spanning the launch times. We presented the retrieval of the temperature and density data from the dual-channel Rayleigh lidar system in Chapter 3. We plot the average temperature profile for the whole night (1827 – 0714 LST) and around the MTeX launches (2330 – 0130 LST) in Figure 4.4. The whole night temperature profile was initialized with a CONE temperature at 100 km was two-hour temperature profiles was initialized with a CONE temperature at 92.5 km. For comparison we plot the temperature profiles from the Mass Spectrometer Incoherent Scatter (MSIS) model in green [Hedin, 1991] and from the Stratosphere-Troposphere Processes and their Role in Climate (SPARC) January climatology in blue [SPARC, 2002]. The MSIS and SARC temperature profiles show a well-defined stratopause near 50 km. Clearly, the temperature structure was quite different from that of either the MSIS or SPARC profiles. The lidar temperature profiles show a colder stratosphere and warmer mesosphere with a near isothermal profile between 35 km and 85 km and no discernible stratopause. In this altitude range the lidar profile only varies by 15 K while MSIS and SPARC both vary

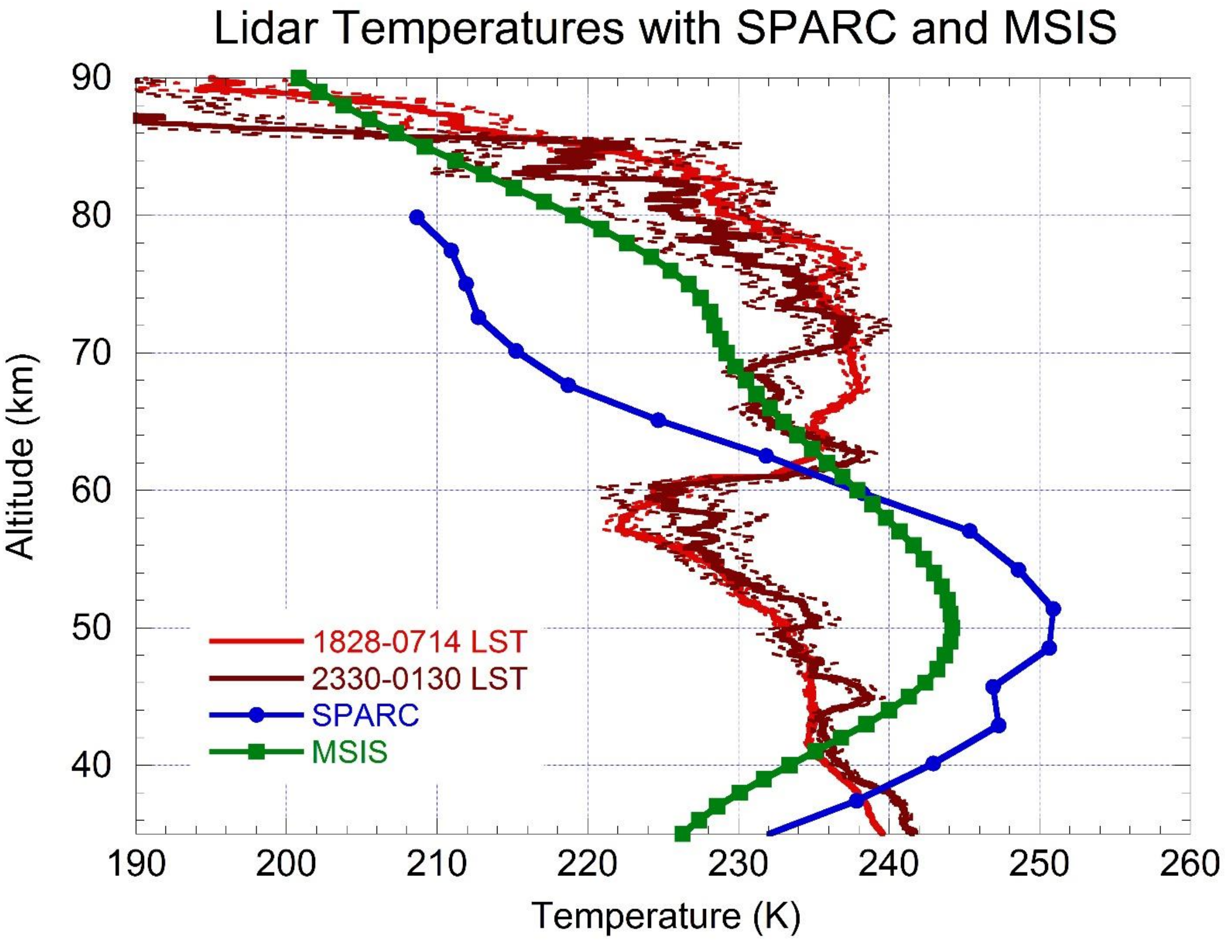

Figure 4.4. Nightly averaged lidar, 120-minute lidar centered on MTeX rocket launch times, MSIS and SPARC temperature profiles for 25-26 January 2015. See text for details.

by 40 K over the same altitude range. These differences indicate that the Arctic atmosphere was disturbed on the night of the MTeX investigation, consistent with the planetary wave activity in the previous Section.

There are MILs present near 76 km and 85 km in the two-hour lidar temperature profile in Figure 4.4. To investigate these MILs further we present a false-color temperature contour plot for the whole night in Figure 4.5. Figure 4.5 shows the presence of several long-lived temperature maxima. We again see the two MILs in altitude range of the CONE measurements above 70 km: at 76 km and 85 km. We characterize the MILs following Irving et al. [2014]. We plot the characteristics of the MILs in Figure 4.6 and present the average characteristics of these two MILs in Table 4.1. The peak altitude is where the altitude of the maximum temperature of the MIL. The amplitude is the difference between the maximum temperature at the peak and the minimum temperature below the peak and shows the strength of the MIL. The topside gradient is given as the largest gradient shows the instability of the topside of the MIL. The depth of the MIL is difference between the altitude of the maximum and the altitude of the minimum and shows the size of the MIL. The 85 km MIL is a large amplitude MIL and has a super-adiabatic gradient on its topside for most of its existence. The 76 km MIL is a smaller MIL with a sub-adiabatic lapse rate on its topside. The topside of the 85 km MIL appears to be convectively unstable while the 76 km MIL appears to be stable. The upper MIL is relatively narrow with a depth of about 1 km. We can compare the characteristics of these two MILs to the 79 MILs investigated by Irving et al. [2014]. We note that these two MILs are between 15 km to 20 km higher than Irving et al. [2014]. The upper MIL has a similar amplitude while the lower MIL smaller than Irving et al. [2014]. The lower MIL has a

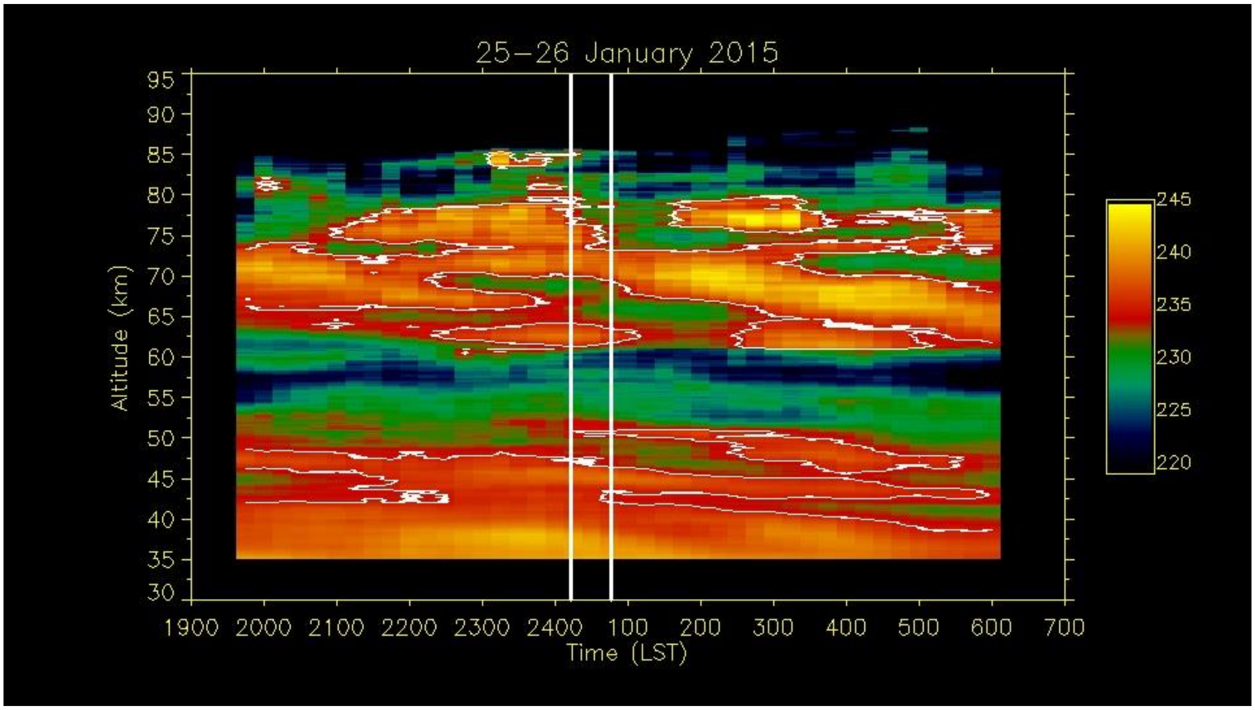

Figure 4.5. False color temperature plot on the night of 25-26 January 2015. The two vertical white lines show the times of the MTeX investigation rocket launched. The white contour is 235 K.

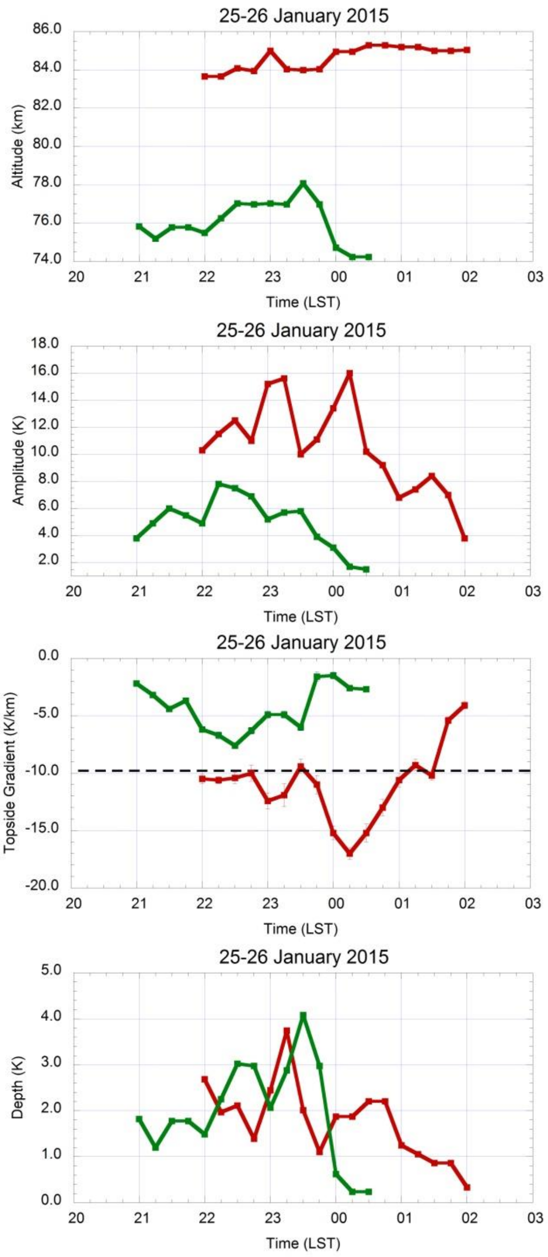

Figure 4.6. Temporal evolution of peak altitude (first, top), amplitude (second), topside lapse rate (third), and depth (fourth, bottom) for the upper MIL in red and the lower MIL in green. The dashed line in the third panel is the adiabatic lapse rate.

Table 4.1: Average characteristics of MILs at PFRR on 25-26 January 2015

	Upper MIL	Lower MIL
Time (LST)	2200-0200	2100-0030
Peak Altitude (km)	85	76
Amplitude (K)	10.4	4.9
Topside Lapse Rate (K/km)	10.7	4.3
Depth (km)	1.7	2.0

similar topside gradient while the upper MIL has a stronger topside gradient than Irving et al. [2014]. Finally, the depth of both MILs are similar to Irving et al. [2014].

We plot the relative density fluctuations derived from the Rayleigh lidar signals in Figure 4.7. In the top panel we plot the fluctuations derived from two hour integrated densities at 15 minute cadence. This panel shows the longer-period (> 4 hr) gravity waves during the night. In the bottom panel we plot the fluctuations based on 30 minute integrated densities at five minute cadence. We have also removed fluctuations with periods of greater than 4 h from the fluctuations in the lower panel. This panel shows the shorter-period (< 4 hr) gravity waves during the night. We have calculated these fluctuations over the 37.5 km to 52.5 km and 62.5 km to 77.5 km altitude regions. Thus the fluctuations in the upper panel represent periods between 4 h and 12 h and vertical wavelengths between 2 km and 15 km. The fluctuations in the lower panel represent periods between 30 min and 4 h and vertical wavelengths between 2 km and 15 km. We analyze the Rayleigh lidar gravity wave data as we did earlier in Chapter 2. We characterize the gravity wave activity in the 40 km to 50 km region and the 45 km to 55 km region. The gravity wave characteristics that we calculated are given in Table 4.2. From Table 4.2 we can see that all the gravity wave activity in the 40 km to 50 km range is within the range of values found in January from the multi-year study of Chapter 2, but it is lower than the average January values. These values are consistent with the suppressed wave activity expected as a result of the light winds and low ageostrophy reported in the previous Section. We see that the gravity wave activity in the 45 km to 55 km altitude range is lower than that found in the 40 km to 50 km attitude range. As in Chapter 2, we calculate the ratio of specific potential energies and ratio of densities over

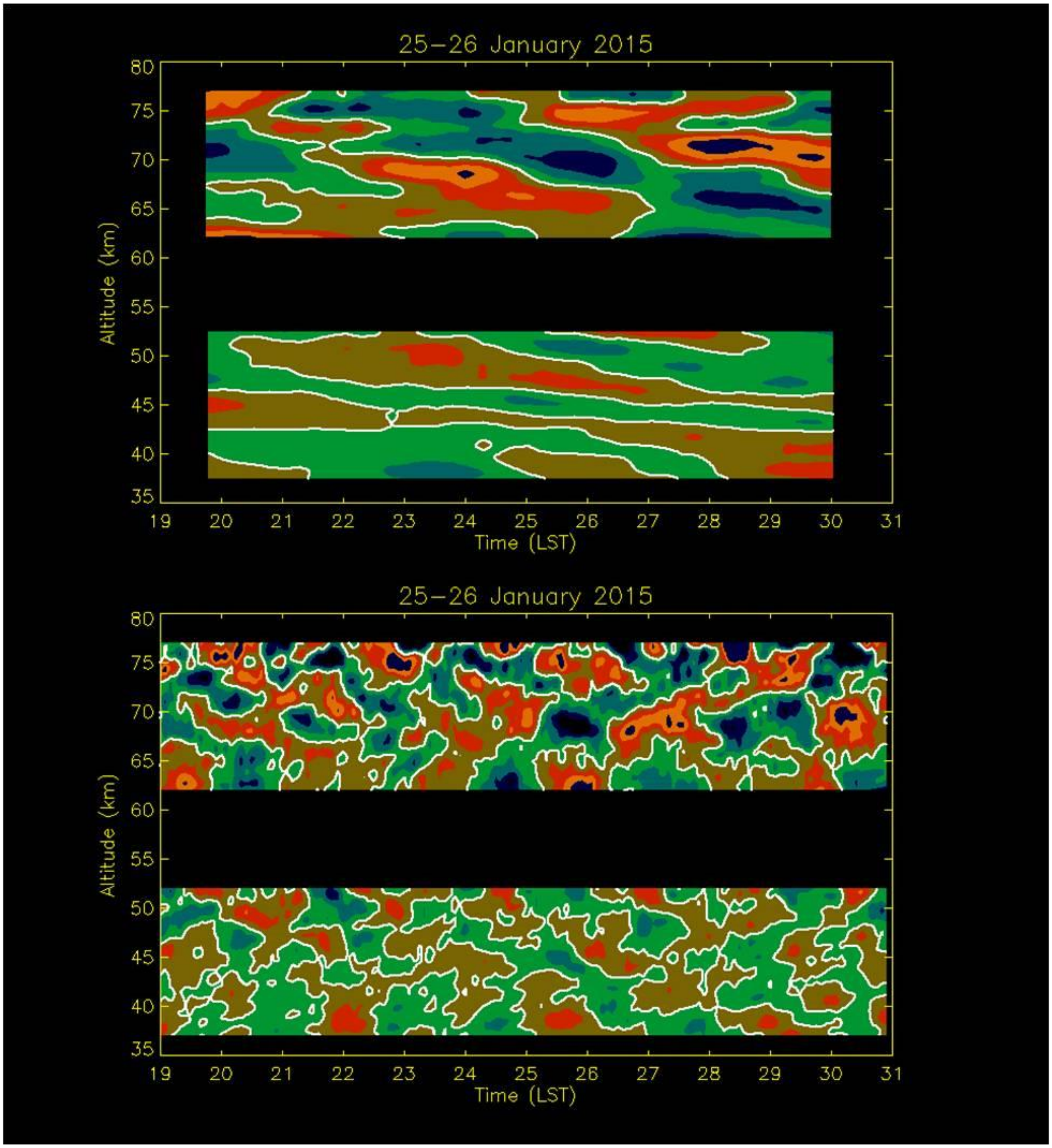

Figure 4.7. Gravity waves as seen in the Rayleigh lidar density perturbations on the night of 25-26 January 2015. The top panel is the 120 minute integrated data. The bottom panel is the 30 minute data.

Table 4.2: Gravity wave activity at PFRR on 25-26 January 2015[1]

Altitude Range (km)	RMS Density Fluctuations (%)	RMS Vertical Displacement (m)	Specific Potential Energy (J/kg)	Buoyancy Period (s)
40-50	0.26 (0.46)	66 (103)	0.84 (2.66)	319 (303)
45-55	0.11	28	0.15	326

[1]: Values in parenthesis are average values for January from Chapter 2.

these two altitude ranges. We calculate a specific potential energy ratio of 0.17 that corresponds to a decay length of 2.6 km and a density ratio of 0.49 which corresponds to a scale height of 7.0 km. These correspond to an energy ratio of 0.085 and a decay length of 2.0 km. All of these values are smaller than those found in Chapter 2, and indicate that the waves are damped as they propagate upwards. This damped behavior is similar to that seen during a major SSW on the night of 21-22 January 2009 that we presented in Chapter 2.

We can also characterize monochromatic gravity waves using both the 2-h and 30-min density data shown in Figure 4.7. We average the density over successive 1 km altitude ranges and fit a single harmonic of a given period to the densities. At each altitude range we identify the harmonic with the highest signal-to-noise ratio (SNR). We then investigate if that harmonic shows a coherent downward phase progression over a range of altitudes. We choose that harmonic that has the highest SNR and shows a coherent phase progression over the altitude range as representing a monochromatic gravity wave. In the 2-h data we find a 9.8-hour wave with a vertical wavelength of -7.7 ± 3.7 km and an SNR of 4.9 over 44 km to 51 km. This same wave is found with a vertical wavelength of -11.2 ± 8.6 km and an SNR of 2.3 over 62.5 km to 73.5 km. This 9.8-hour wave persists through the night. In the 30-min data we find a 2.5-hour wave with a vertical wavelength of -11.2 ± 5.0 km and an SNR of 0.17 over 44 km to 50 km. The lower SNR is reflects the smaller integration time of the new lidar signals. However, we cannot find a 2.5-hour wave with a coherent phase progression over the whole night in the upper range. When we limit the time interval from 1900 to 0000 LST, we find a 2.5-hour wave in the upper range with a coherent downward phase progression. This wave has a vertical wavelength of -6.24 ± 4.11 km and SNR of 0.57 over 64 km to 77 km. We use the gravity wave polarization and dispersion relationships to calculate the wind speed, phase speed, and horizontal wavelength of these waves from the observed period, vertical wavelength and thermal conditions [Hines, 1960]. We present these results in Table 4.3. In the upper range the phase speed of the 2.5-hour wave of 20.1 m/s is close to the RMS superposition of the horizontal wind speed of the 2.5-hour and 9.8-hour waves of 14.8 m/s. Thus in this altitude range the 2.5-hour wave could relatively easily be rendered unstable and break.

The amplitudes of these waves are estimated based on the relationship between displacement fluctuation and relative density fluctuation in a stratified incompressible atmosphere,

$$\zeta \frac{N^2}{g} = \frac{\Delta n}{n} \tag{4.1}$$

where ζ is amplitude (vertical displacement) of the wave, N^2 is the buoyancy frequency squared, g is gravity, and Δn/n is the relative density fluctuations. If we consider a compressible atmosphere, the relationship becomes,

$$\zeta \kappa \frac{N^2}{g} = \frac{\Delta n}{n} \tag{4.2}$$

where κ is the ratio of specific heats (2/7) [Sutherland, 2010]. Thus for a given relative density fluctuation the corresponding displacement fluctuation will be 7/2 times larger in a compressible fluid than in an incompressible fluid. This factor of 7/2 would increase the horizontal wind speed of the 2.5-hr wave from 6.4 m/s to 22.3 m/s and the RMS superposition of the two waves from 14.8 m/s to 65.8 m/s. We conclude that the conditions exist, whether through superposition of two waves and the background winds or through

Table 4.3 Characteristics of Monochromatic Gravity Waves at PFRR on 25-26 January 2015.

Altitude range (km)	Period (hr)	Amplitude (%)	Vertical Wavelength (km)	Horizontal Wavelength (km)	Horizontal Phase speed (m/s)	Horizontal wind speed (m/s)
44-51	9.8	0.75	-7.7±3.7	1260	36	6.7
62.5-73.5	9.8	1.5	-11.2±8.6	1810	51	13.3
44-50	2.5	0.43	-11.2±5.0	318	35	2.1
64-77	2.5	1.3	-6.2±4.1	181	20	6.4

the wave alone, for the 2.5 hr wave to break in the upper mesosphere near the time of the MTeX launches

4.4. High resolution data from CONE

4.4.1. Temperature and stability

We have described the synoptic- and local-scale meteorology on the night of 25-26 January 2015 based on satellite and lidar measurements. Now we will describe the meteorology and fluctuations measured by the CONE instruments. We described the CONE instrument and data retrieval methods in Chapter 3. We show the temperatures retrieved from CONE for the 46.009 upleg, 46.009 downleg, and 46.010 downleg in Figure 4.8. Figure 4.8 shows two MILs in all three legs that are consistent with the two MILs described above in Section 4.3. The top left panel shows the temperature profile for the upleg in 46.009 with two MILs at 75 km and 82 km. The middle left panel shows the temperature profile for the downleg in 46.009 with two MILs at 73 km and 82 km. The bottom left panel shows the temperature for the downleg in 46.010 with a MIL at 80 km and evidence of the topside of the lower. The upper (lower) MIL corresponds to the upper (lower) MIL of Table 4.1. Similar temperatures are measured by both CONE instruments and the Rayleigh lidar in the 70-90 km. We estimated the buoyancy frequency squared (N^2) from the CONE temperature profiles. These profiles are shown in the right panels of Figure 4.8. These N^2 profiles show that the atmosphere had multiple regions of stability (higher N^2) and instability (lower N^2). The profiles for both the downlegs of 46.009 and 46.010 have negative values for N^2 at 81 km. In regions where N^2 is negative the

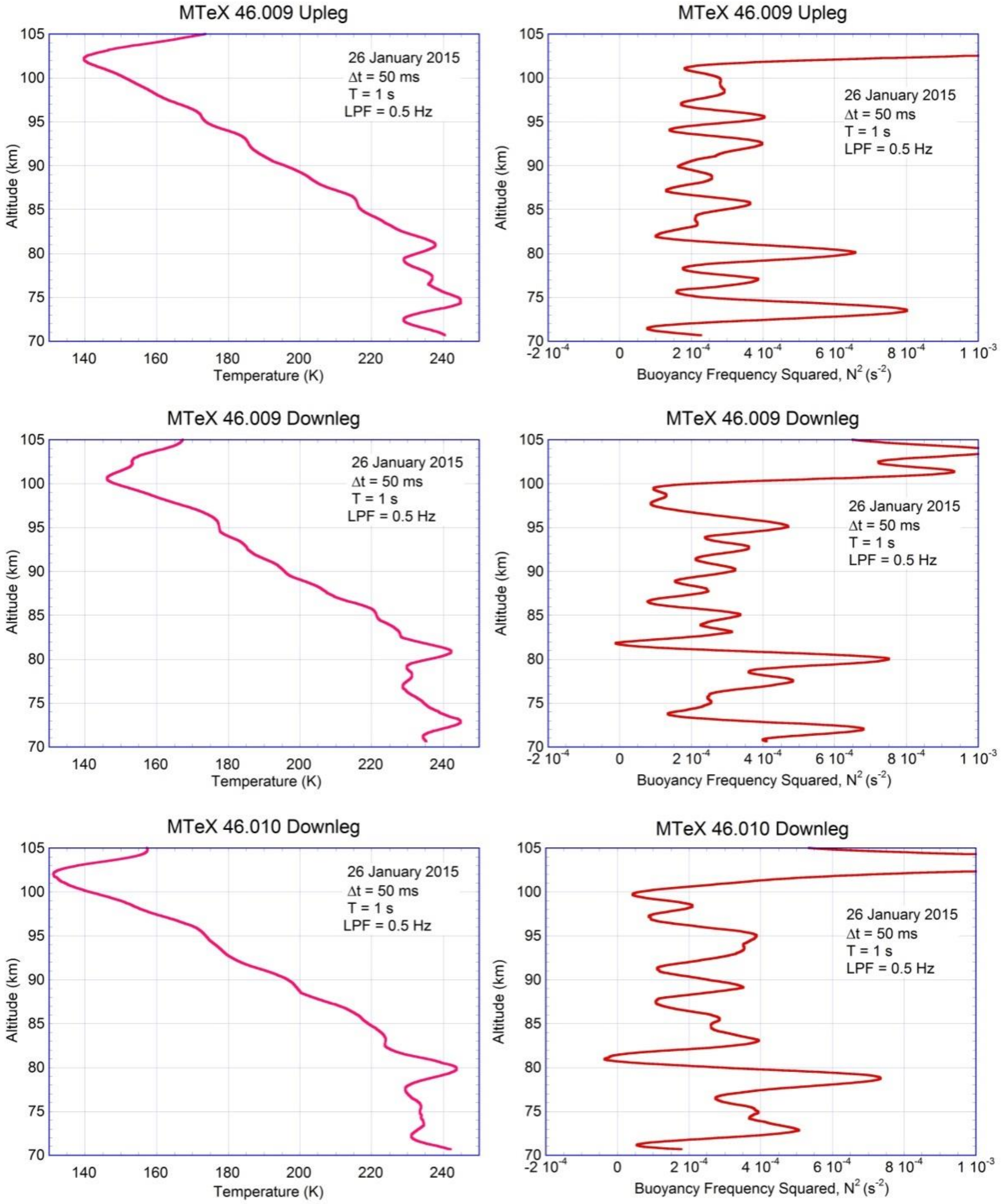

Figure 4.8. Temperature (left) and buoyancy frequency (right) profiles from CONE instruments. Top panels are the upleg of 46.009. Middle panels are the downleg of 46.009. Bottom panels are the downleg of 46.010.

atmosphere is highly unstable and gravity waves cannot readily propagate through these regions. It is around this altitude, which coincides with the altitude of the upper MIL detected by the lidar that we expect to find large values of density fluctuations.

As we discussed earlier, we are basing our lidar and CONE measurements of atmospheric fluctuations on relative density fluctuations, $\Delta n/n$, and then deriving vertical displacement fluctuations, ζ, to describe wave activity and turbulent activity. However, the physical basis of these motions is that vertical displacements give rise to the density fluctuations that we measure. As we saw in Equation 4.1 the relationship between $\Delta n/n$ and ζ is very sensitive to the atmospheric stability, due to the N^2. In regions of low stability, low N^2, a given vertical displacement will result in a smaller density fluctuation, while in regions of higher stability, high N^2, a given vertical displacement will result in a larger density fluctuation. At the point of instability, where N^2 is zero, the vertical displacement fluctuation becomes “invisible”. Thus in investigating the fluctuations measured by the CONE instrument we will report both the RMS relative density and RMS vertical displacement fluctuations.

4.4.2. Small-scale fluctuations

We examine the small-scale fluctuations measured by CONE by investigating the power spectrum of the fluctuations. We use the method described in Chapter 3 to determine the power spectrum of the fluctuations based on 1-s intervals of 5208 samples off-set every 50 ms in altitude. We plot the spectra at all altitudes for all three flight legs in Figure 4.9. In processing these spectra we have removed the 2 Hz spin of the rocket and have also applied a Von Hann window to the fluctuations. In Figure 4.9 we see multiple layers where the spectra extend to higher frequencies (i.e., smaller scales). In

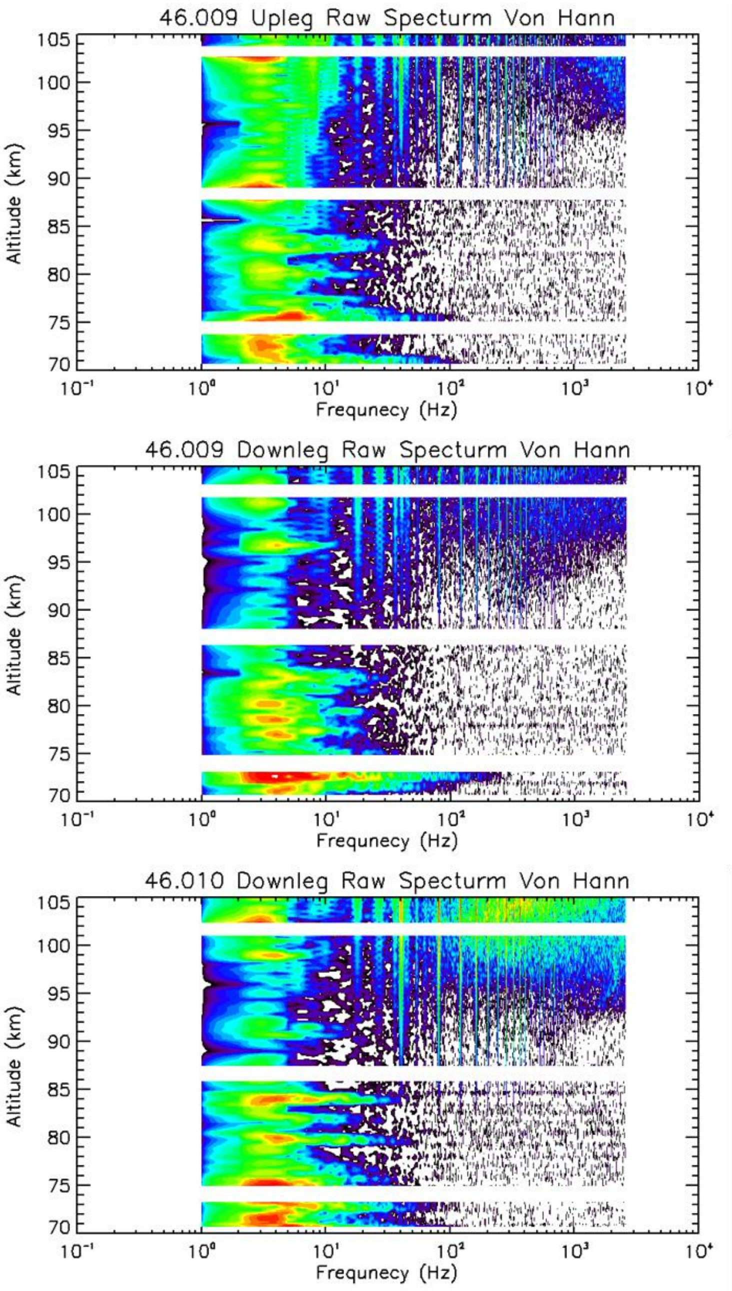

Figure 4.9. Final power spectra from the CONE data for 25-26 January 2015. Top panel is the upleg of 46.009. Middle panel is the downleg of 46.009. Bottom panel is the downleg of 46.010.

Figure 4.9 we also see that at higher altitudes above 90 km there are spikes in the spectra at frequencies above 20 Hz. The cause of these spikes is believed to be instrumental in origin and is still under investigation. Accordingly we limit our analysis of the fluctuations to altitudes below 90 km.

We start examining the CONE measurements of the small-scale fluctuations by investigating the relationship between the altitude distribution of the RMS density ($\Delta n/n$) and vertical displacement (ζ) fluctuations and the CONE measurement temperature profiles. In Figure 4.10 we plot the RMS density fluctuations and temperature (left) and the RMS vertical displacement and temperature (right) as functions of altitude. The upper panels show the measurements in the upleg of 46.009, the middle panels show the measurements in the downleg of 46.009, and the lower panels show the measurements from the downleg of 46.010. The discontinuities in both RMS relative density fluctuations and RMS vertical displacements are not geophysical in nature but are due to the range changes in the CONE instrument that we discussed in Chapter 3. We see that the values of the RMS density fluctuations are higher in all three panels around the MILs. There are enhancements in the fluctuations on both the bottomside and topside of the MILs. The largest RMS density fluctuation is found during the downleg of 46.009 at 73 km with a value of 0.4%. This enhancement coincides with the bottomside of the lower lidar MIL. The RMS vertical displacements are also higher in all three panels around the MILs. Again, there are enhancements on both the bottomside and topside of the MILs. The largest RMS displacement enhancement is found during the downleg of 46.009 at 81 km with a value of greater than 1000 m. This enhancement is on the topside of the upper lidar MIL. The side-by-side panels of Figure 4.10 illustrate Equation 4.1 perfectly. In

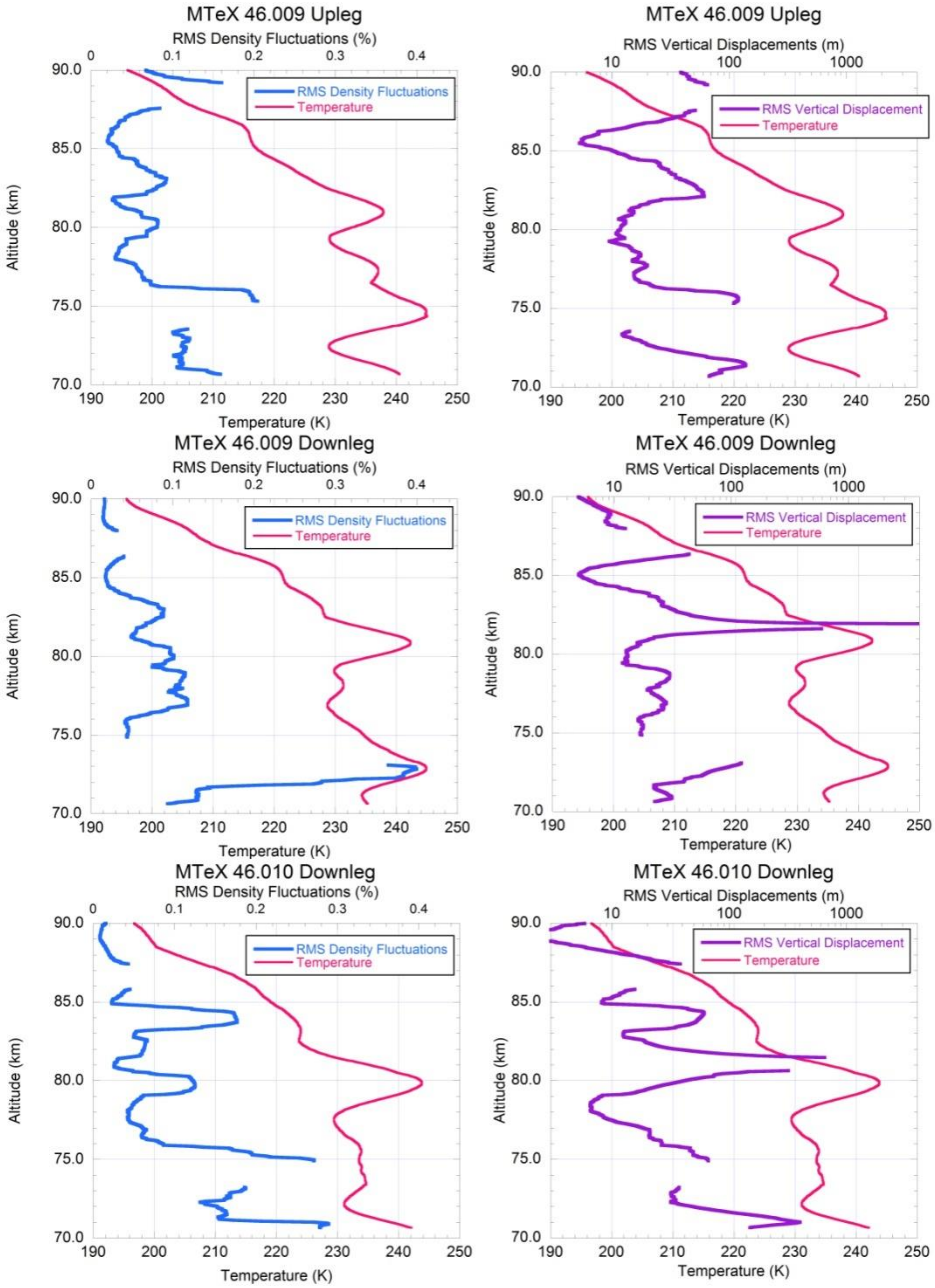

Figure 4.10. RMS density fluctuation (left) and RMS vertical displacement (right) with temperature profiles on 25-26 January 2015. Top panels are the upleg of 46.009. Middle panels are the downleg of 46.009. Bottom panels are the downleg of 46.010.

regions of low N^2, the topsides of the MILs, the RMS vertical displacements are very large while the corresponding RMS relative density fluctuations remain low. For example, the highest value of RMS vertical displacement mentioned above is at 81 km with a value greater than 1000 m. The RMS density fluctuation seen by the CONE instrument in that region is 0.06%, a very low value. The low N^2 masks the large RMS vertical displacement from the direct CONE measurement. To directly compare N^2 with both RMS relative density and RMS vertical displacement we present scatter plots in Figure 4.11. In the top panel of Figure 4.11 we plot the RMS relative density fluctuations versus N^2 for all three flight legs of the MTeX investigation. The bottom panel of Figure 4.11 is the RMS vertical displacements versus N^2 for all three flight legs of the MTeX investigation. The RMS relative densities are plotted on a linear scale while the RMS displacements are plotted on a log scale. These two panels show different behaviors. The top panel of Figure 4.11 shows that low values of N^2 (low atmospheric stability) led to smaller fluctuations in the atmosphere. The largest RMS relative density fluctuations with values of ~0.4% occur at high values of N^2 (high atmospheric stability). The bottom panel of Figure 4.11 shows that low values of N^2 are associated with larger fluctuations in the atmosphere. The largest RMS vertical displacements with values greater than 100 m occur near zero values of N^2.

Figures 4.10 and 4.11 demonstrate one important fact not yet mentioned. There are fluctuations through the whole atmospheric region measured by the CONE instrument. The background meteorology may be masking some fluctuations from the direct CONE measurements, but fluctuations exist everywhere regardless of local meteorology. These data do not tell us anything about the origins of the fluctuations. In order to discover which of these fluctuations are turbulent in origin we must now turn to

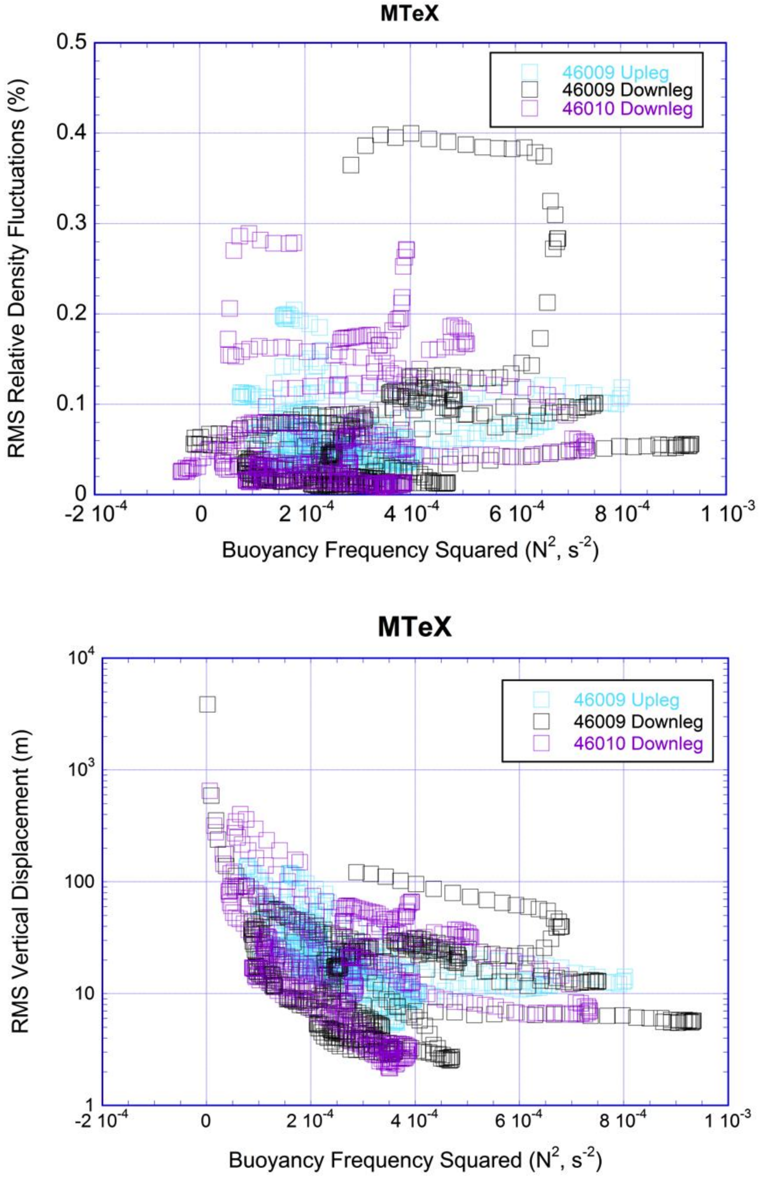

Figure 4.11. RMS density fluctuations versus the buoyancy frequency squared for all three analyzed legs (top) and RMS vertical displacement versus the buoyancy frequency squared for all three analyzed legs (bottom).

the turbulent analysis that we presented in Chapter 3

4.4.3. Characterization of turbulence

We conducted the turbulent analysis that we described in Chapter 3 to the CONE measurements. For each 1-s segment of data we calculated a spectrum and attempted to fit a Heisenberg model and estimate a value of the energy dissipation rate, ε. Unlike the RMS relative density and vertical displacement calculations we applied nine criteria to our fits to ensure they the results were significant. We plot the results of our turbulent analysis in Figure 4.12. The left panels of Figure 4.12 show the values of ε over-plotted with the CONE temperature profiles. The right panels of Figure 4.12 show the values of the inner scale, l_0, over-plotted with the CONE temperatures. We see that the number of estimates of ε and l_0 is much less than the number of RMS relative density and vertical displacement. For the upleg in 46.009 we have 488 RMS relative density and vertical displacement estimates and 58 ε and l_0 estimates. The values of ε and l_0 vary between 0.16 mW/kg and 29 mW/kg and 16 m and 121 m respectively. For the downleg in 46.009 we have 484 RMS relative density and vertical displacement estimates and 62 ε and l_0 estimates. The values of ε and l_0 vary between 0.12 mW/kg and 8.7 mW/kg and 12 m and 113 m respectively. For the downleg in 46.010 we have 477 RMS relative density and vertical displacement estimates and 20 ε and l_0 estimates. The values of ε and l_0 vary between 0.19 mW/kg and 18 mW/kg and 40 m and 93 m respectively. In all three flight legs the highest values of ε are located in the topside of the MILs in the negative temperature gradients. The strongest and most persistent turbulence appears in the topside of the upper MIL between 80 km and 85 km. While we show that the values of ε are clustered in distinct altitudes, there is significant variation over sub-kilometer scales

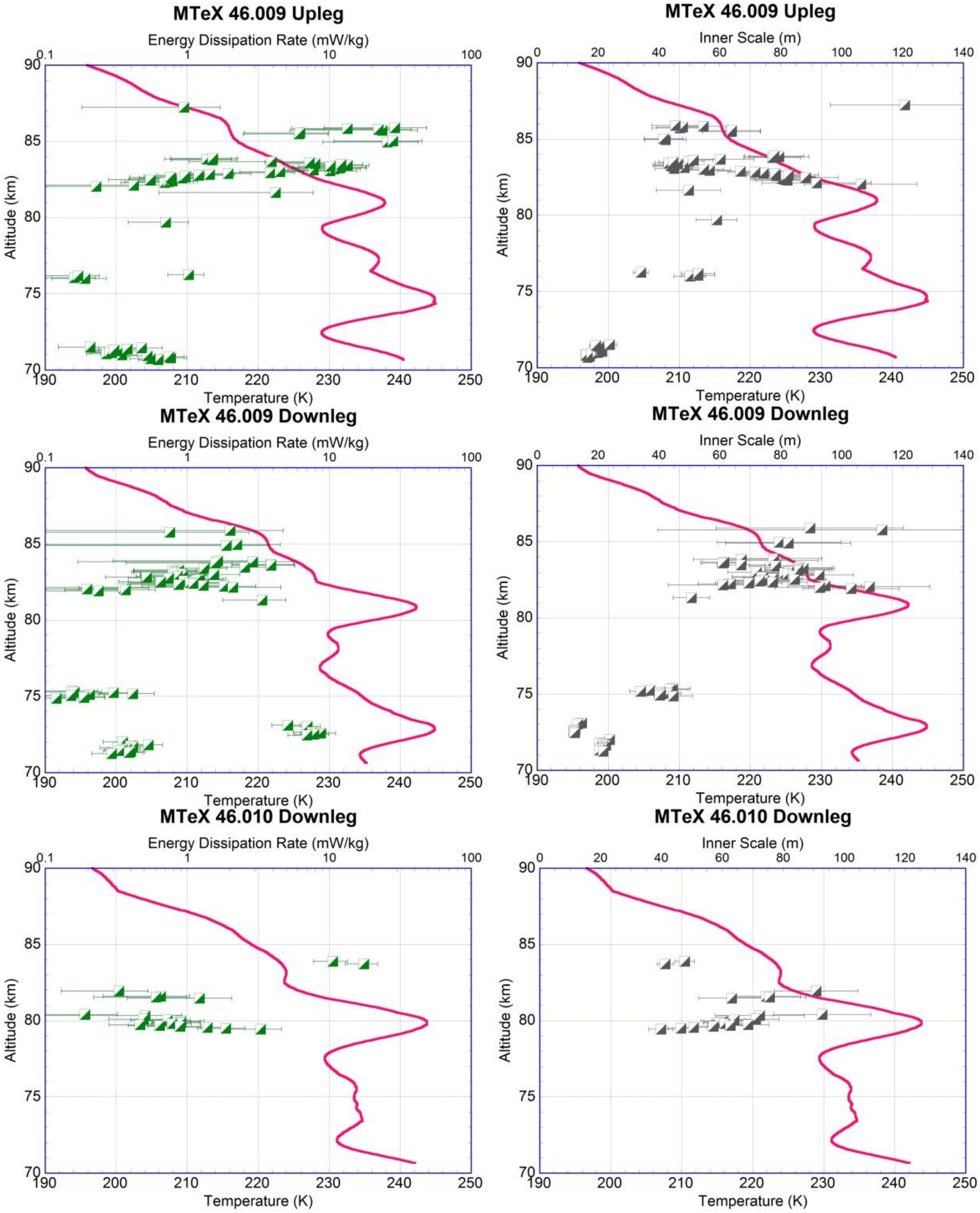

Figure 4.12. Energy dissipation rate (left) and inner scale (right) with error bars and temperature profiles on 25-26 January 2015. Top panels are the upleg of 46.009. Middle panels are the downleg of 46.009. Bottom panels are the downleg of 46.010.

within the clusters. The largest value of turbulent dissipation rate is 29 mW/kg, which is relatively low compared to the values we reviewed in Chapter 1. We also note that the smallest ε for a given turbulent energy the value of l_0 increases as the kinematic viscosity increases with altitude.

We plot ε versus N^2 in Figure 4.13 for all three flight legs. We separate the values of ε based on whether they occur in a region of positive or negative temperature gradient. We see that the values ε decrease as N^2 goes to zero just as we saw in the RMS relative density fluctuations in Figure 4.11. As we have discussed earlier this behavior highlights the inherent sensitivity bias in the CONE measurements based on relative density fluctuations. However, more significantly we see in Figure 4.13 that of our 139 turbulent measurements, 115 (or 83%) measurements are detected in regions with negative temperature gradients. This suggest that the turbulence occurs in association with convective instabilities and is generated by gravity wave breaking.

4.5. Evidence of wave breaking

Our measurements and analysis has shown the following: there was a MIL with a super-adiabatic lapse rate in the upper mesosphere, there was a gravity wave of period 2.5 h that appeared to break in the upper mesosphere and there was enhanced and persistent turbulence in the upper mesosphere that is collocated with regions of convective instability.

To investigate the wave-breaking and stability in upper mesosphere further, we calculated the potential temperature from the 2-h Rayleigh lidar temperature data under

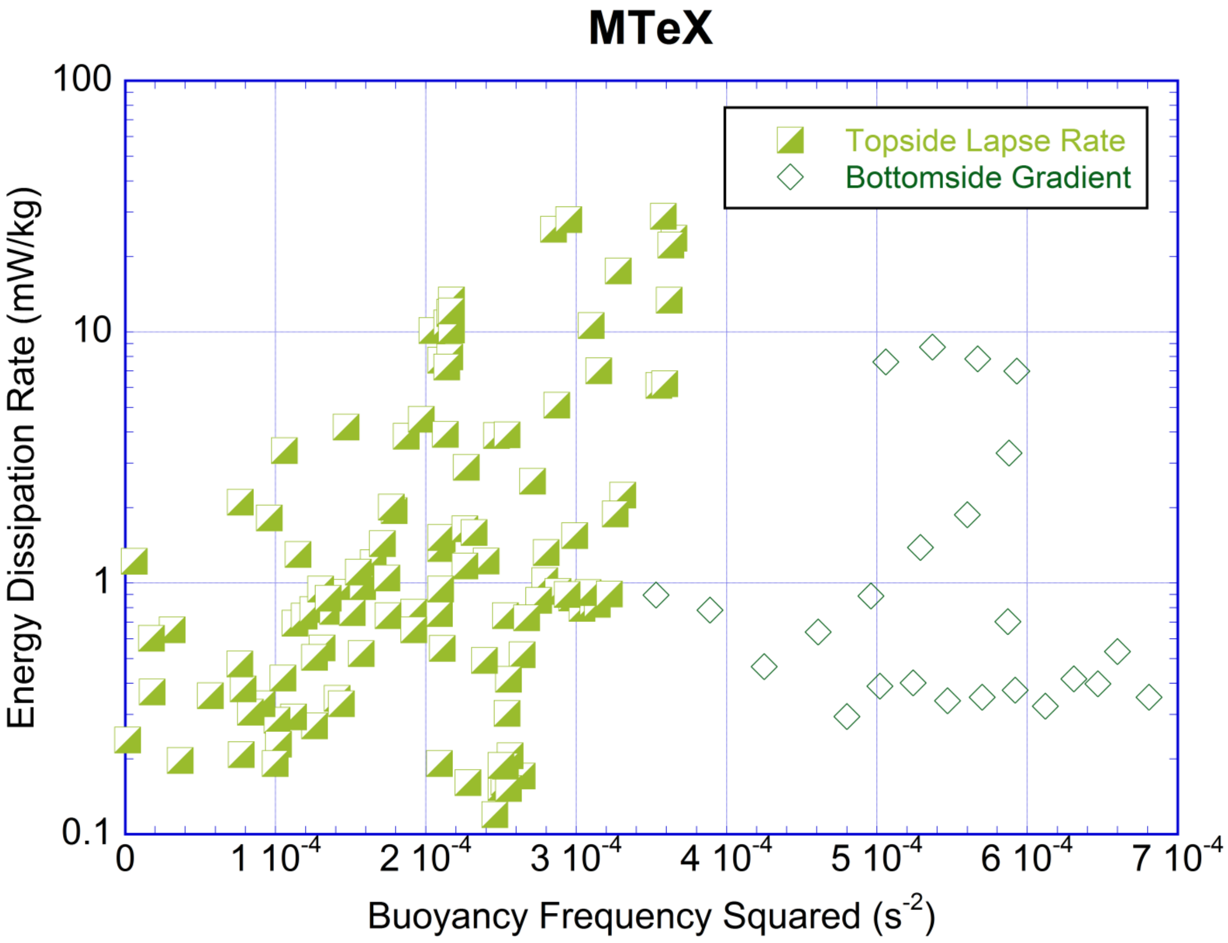

Figure 4.13. Energy dissipation rate versus buoyancy frequency squared and location in the MIL.

the assumption of hydrostatic equilibrium [Franke and Collins, 2003]. Following Franke and Collins [2003] we initialized the calculations of the potential temperature at a reference altitude of 62 km and integrated upwards. We plot the contours of potential temperature as a function of time and altitude in the upper panel of Figure 4.14. Potential temperature represents the temperature that the air parcels would have if they descended adiabatically to 62 km. We note the use of a 62 km initial altitude yields values of potential temperature of less than 700 K instead of the much higher values that we would expect relative to the ground. Under adiabatic motions, such as non-breaking waves, the contours (or isentropes) undulate but remain a fixed distance apart from each other. Under diabatic motions such as breaking waves the contours (or isentropes) undulate and spread, and eventually overturn [Franke and Collins, 2003; Xu et al., 2006], In Figure 4.14 we see clear spreading of the isentropes between 2230 and 0200 in the 85 km to 90 km altitude region. Given the low temporal resolution of our temperature data (2 h) and the proximity to the reference height (62 km) we assume that the potential temperature is more strongly disturbed than appears in our estimate. However, we have one other diagnostic available to investigate this further.

On the night of 25-26 January 2015 we also operated a sodium resonance lidar at PFRR. The sodium resonance lidar yielded measurements of the mesospheric sodium layer that typically exists between 70 km and 120 km [Collins and Smith, 2004; Collins et al., 2011]. We calculate sodium profiles over successive 1 h intervals every 15 min. We plot the sodium density as a function of time and altitude in the lower panel of Figure 4.14. Starting near 87 km at 2130 LST we see strong downward motion in the lower half of the layer. This is followed by overturning of the sodium between midnight and 0200 LST.

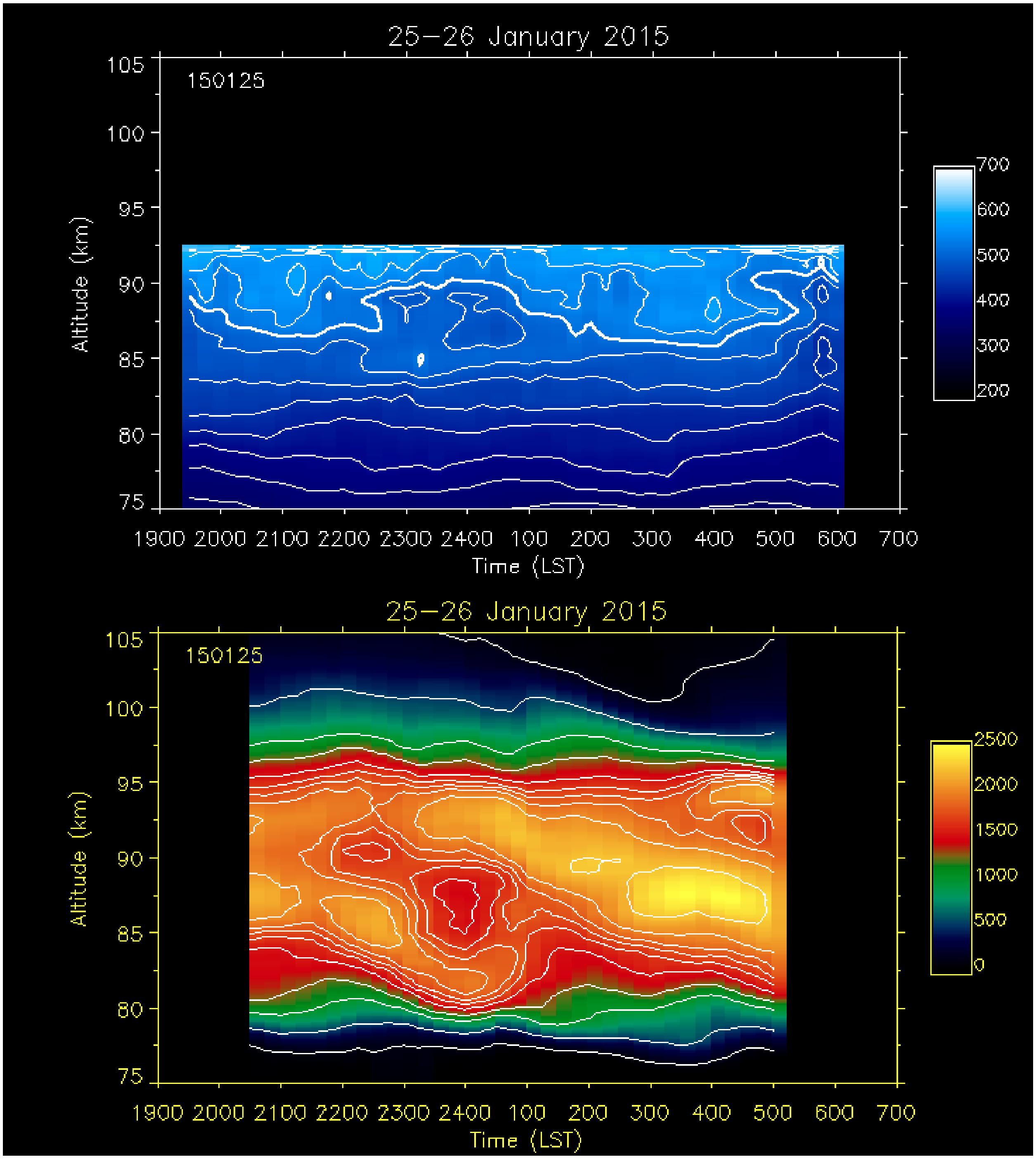

Figure 4.14. Sodium densities (top) and potential temperatures (bottom) in time on 25-26 January 2015.

While sodium is not a passive tracer, the apparent motion of the sodium reflects the spreading background atmospheric motion at these time scales [Collins et al., 2011]. The overturning in the sodium measured by the resonance lidar coincides with the isentropes that are independently derived from the Rayleigh lidar measurements and persists for about 2.5 h, which corresponds to the period of the small-scale monochromatic wave.

4.6. Summary and conclusions

In this Chapter we have investigated the meteorology from the planetary to turbulent scale on the night of the MTeX investigation: 25-26 January 2015. We found that the atmosphere was highly disturbed in the wake of a SSW event in early January. The MTeX investigation appears to have occurred early in the recovery phase of the SSW. During this period the winds were weak, and there was little ageostrophy, resulting in weak gravity wave activity in the middle atmosphere. In the midst of this disturbance we found turbulence associated with instability and gravity wave breaking in the 80-85 km region. The turbulence was relatively weak with energy dissipation rates less than 30 mW/kg.

Our observations and analysis indicate that the generation of turbulence is associated with mesospheric inversion layers (MILs) as follows. We find most turbulence in the topside of the MILs and little evidence for turbulence in the bottomside of the MIL. We conclude that the turbulence is generated by waves breaking and producing convective instabilities rather than by waves breaking as they propagate into regions of increased stability in the bottomside of the MIL.

Chapter 5 Summary and Conclusions

In this study we have extended the scope of previous studies of the wave-driven circulation of the Arctic middle atmosphere at Poker Flat Research Range (PFRR), Chatanika, Alaska in several ways. We developed a consistent analysis of Rayleigh lidar data to conduct a multi-year study of gravity wave activity. In support of this study we developed and validated an analysis of ageostrophy using the reanalysis data. We upgraded the Rayleigh lidar system to support a variety of new studies: dual channel Rayleigh lidar measurements, simultaneous multi-channel lidar studies, and real-time retrieval of temperature and density to support rocket observations. We conducted a rocket-borne investigation of turbulence, and developed retrieval and analysis tools to conduct an independent investigation of the turbulence.

In our multi-year study of gravity waves at PFRR we documented the gravity wave activity in the upper stratosphere and lower mesosphere (USLM) over 14 years based on uniform processing of a high-quality set of Rayleigh lidar observations. Despite large daily variability, the gravity wave activity shows a clear annual cycle with a maximum in winter, and systematic inter-annual variability associated sudden stratospheric warming events. The gravity waves in the USLM are saturated and are losing energy with altitude and have a decay length of 17 km.

We find that the gravity wave activity in the upper stratosphere and lower mesosphere is controlled by the winds in the lower stratosphere, where weak winds in the lower stratosphere block the upward propagation of gravity waves through critical layer filtering. This control is evident on both daily and seasonal time scales, where systematic changes in the winds are associated with sudden stratospheric warming (SSW) events.

We find that the gravity wave activity in the upper stratosphere and lower mesosphere is correlated with the ageostrophy in the tropospheric jet. This coupling is only apparent when the waves are not blocked by the winds in the lower stratosphere. Thus we conclude that the primary control of the gravity wave activity is critical layer filtering by the winds in the lower stratosphere, and the secondary control of gravity wave activity is ageostrophic adjustment by the tropospheric jet.

In the Mesosphere-Lower Thermosphere Turbulence Experiment (MTeX) we investigated the meteorology from the planetary to turbulent scales on the night of 25-26 January 2015. We found that the atmosphere was highly disturbed in the wake of a SSW event in early January. The MTeX investigation appears to have occurred early in the recovery phase of the SSW. During this period the winds were weak, and there was little ageostrophy, resulting in weak gravity wave activity in the middle atmosphere. In the midst of this disturbance we found turbulence associated with instability and gravity wave breaking in the 80-85 km region. The turbulence was relatively weak with energy dissipation rates less than 30 mW/kg.

Our observations and analysis indicate that the generation of turbulence is associated with mesospheric inversion layers (MILs) as follows. We find most turbulence in the topside of the MILs and little evidence for turbulence in the bottomside of the MIL. We conclude that the turbulence is generated by waves breaking and producing convective instabilities rather than by waves breaking as they propagate into regions of increased stability in the bottomside of the MIL.

We update Figure 1.6 with the MTeX measurements and present it as Figure 5.1. Like the other values, there is a wider spread in the values of K than ε, reflecting the variations in the atmospheric stability, and the buoyancy frequency squared N^2. We see that the MTeX values of turbulent energy dissipation rate, ε, and eddy diffusion coefficient, K, are lower than reported by the other studies, particularly the Arctic wintertime values reported by Lübken [1997], L97.

We conclude that the low levels of gravity wave activity resulted in these low levels of turbulence. The gravity wave potential energy on the night of 25-26 January 2015 is one of the lowest values recorded in our 14 years of measurements. We see that in a disturbed winter planetary waves control the winds, the winds control the gravity waves, and the gravity waves control the turbulence. This has implications for current model studies of transport, where there is significant uncertainty in the role of eddy transport relative to advection and molecular transport.

A critical limitation of the study is the lack of wind measurements. Our analysis of winds and planetary waves is based on indirect estimates of the wind rather than direct measurements of the wind. Our analysis of stability and wave breaking is based on measurements of temperature and density and thus is biased toward convective instability rather than dynamic instability. Physical theories of turbulence are predicated on dynamic instability and wind shear. Efforts are underway to address this observational limitation at PFRR. Addition of a wind-temperature lidar would provide common volume and scale measurement of wind, temperature and metal density in the mesosphere and lower thermosphere (70-120 km) and directly extend the studies of wave-breaking. Addition of a meteor radar would provide continual wind measurements allowing

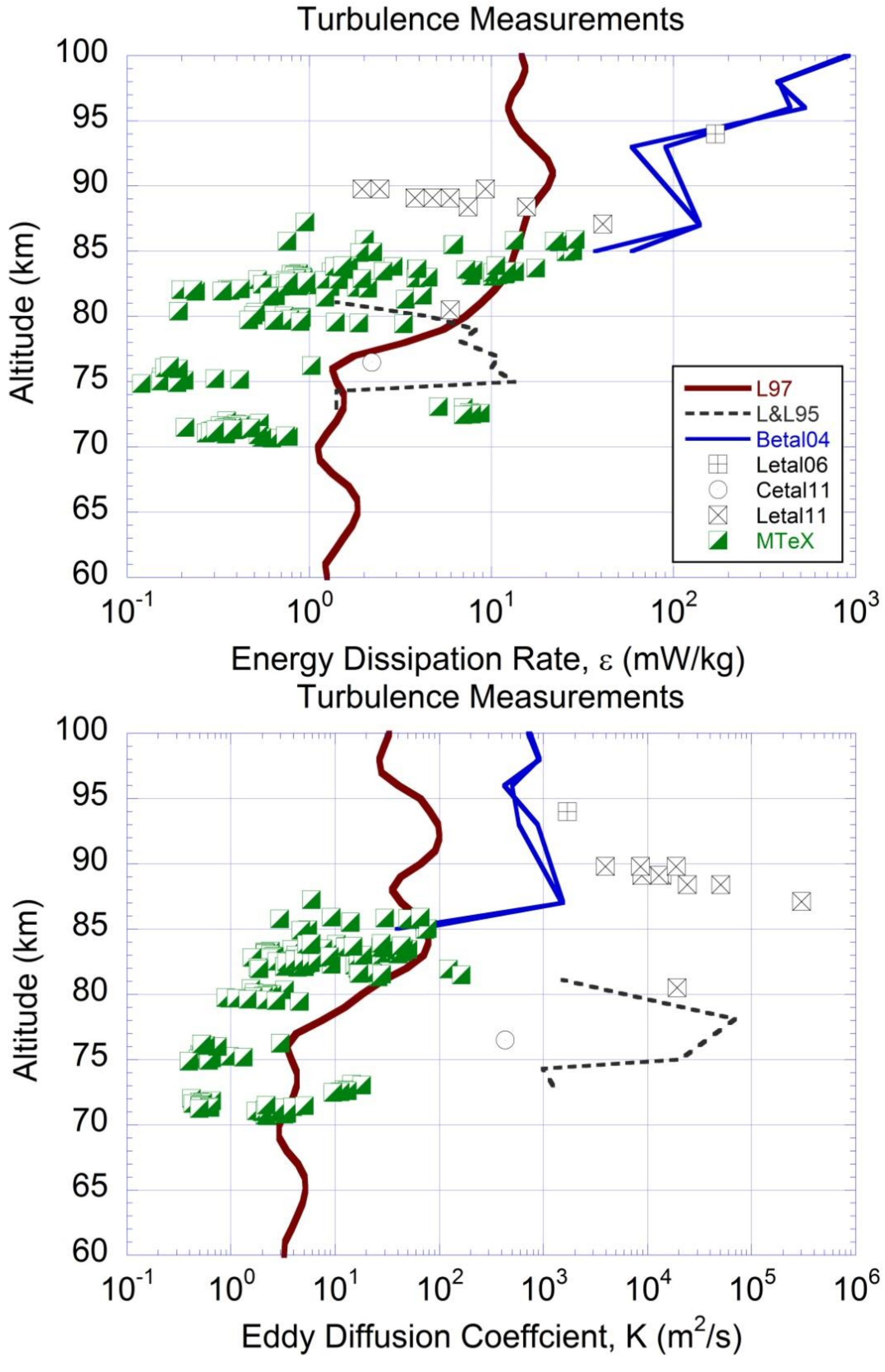

Figure 5.1. Updated energy dissipation rates (top) and eddy diffusion coefficients (bottom) with values found from the MTeX investigation. See Figure 1.6 for details.

characterization of mean winds, planetary waves and tides at the site. The National Science Foundation is currently reviewing proposals to deploy such lidars and radars at PFRR.

References

Ahrens, C. D. (2009), *Meteorology today: An introduction to weather, climate, and the environment*, 549 pp., Cengage Learning, California.

Alexander, M. J., and K. Sato (2015). Gravity Wave Dynamics and Climate: An Update from the SPARC Gravity Wave Activity. *Report on the 35th Session of the Joint Scientific Committee of the World Climate Research Programme 29 June–4 July 2014,* Heidelberg*,* Germany, 9.

Allen, D. R., R. M. Bevilacqua, G. E. Nedoluha, C. E. Randall, and G. L. Manney (2003), Unusual stratospheric transport and mixing during the 2002 Antarctica winter, *Geophys. Res. Lett.*, *30*, 1599, doi:10.1029/2003GL017117.

Andrews, D. G., J. R. Holton, and C. B. Leovy (1987), *Middle Atmosphere Dynamics*, 489 pp., Academic Press Inc., New York.

Baldwin, M. P., T. Hirooka, A. O'Neill, S. Yoden, A. J. Charlton, Y. Hio, W. A. Lahoz, A. Mori (2003), Major stratospheric warming in the southern hemisphere in 2002: Dynamical aspects of the ozone hole split, *SPARC Newsletter*, *20*, SPARC Office, Toronto, ON, Canada, pp. 24–26.

Bernath, P. F., et al. (2005), Atmospheric Chemistry Experiment (ACE): Mission overview, *Geophys. Res. Lett.*, *32*, L15S01, doi:10.1029/2005GL022386.

Bishop, R. L., M. F. Larsen, J. H. Hecht, A. Z. Liu, and C. S. Gardner (2004), TOMEX: Mesospheric and lower thermospheric diffusivities and instability layers, *J. Geophys. Res*., *109*, D02S03, doi:10.1029/2002JD003079.

Brasseur, G. P., and S. Solomon (1995), *Aeronomy of the middle atmosphere: chemistry and physics of the stratosphere and mesosphere*, 2nd ed, Reidel, Dordrecht, 452 pp.

Cahn, A. (1945), An investigation of the free oscillations of a simple current system, *J. Atmos. Sci.*, *2*(2), 113-119.

Champion, K. S. W., A. E. Cole, and A. J. Kantor (1985), Standard and Reference Atmospheres, In A. S. Jursa (Ed.), *Handbook of Geophysics and the Space Environment*, pp. 14-1-14-43, Air Force Geophysics Laboratory, Virgina.

Chandran, A., R. L. Collins, R. R. Garcia, and D. R. Marsh (2011), A case study of an elevated stratopause generated in the Whole Atmosphere Community Climate Model, *Geophys. Res. Lett.*, 38, L08804, doi:10.1029/2010GL046566.

Chandran, A., R. L. Collins, R. R. Garcia, D. R. Marsh, V. L. Harvey, J. Yue, and L. de la Torre (2013), A climatology of elevated stratopause events in the whole atmosphere community climate model, *J. Geophys. Res.*, *118,* 1234-1246, *doi:10.1002/jgrd.50123.*

Chandran, A., R. L. Collins, and V. L. Harvey (2014), Stratosphere-mesosphere coupling during stratospheric sudden warming events, *Adv. Spa. Res.*, 53, 1265–1289, doi: 10.1016/j.asr.2014.02.005

Chipperfield, M. P., S. S. Dhome, W. Feng, R. L. McKensie, G. J. M. Velders, and J. A. Pyle, (2015), Quantifying the ozone and ultraviolet benefits already achieved by the Montreal Protocol, *Nat. Communs.*, *6*, doi: 10.1038/ncomms8233.

Collins, R. L., and R. W. Smith (2004), Evidence of damping and overturning of gravity waves in the arctic mesosphere: Na lidar and OH temperature observations*, J. Atmos. Sol. Terr. Phys*., *66*, 867–879.

Collins, R. L., G. A. Lehmacher, M. F. Larsen, and K. Mizutani (2011), Estimates of vertical eddy diffusivity in the upper mesosphere in the presence of a mesospheric inversion layer, *Ann. Geophys.*, *29*(11), 2019-2029, doi:10.5194/angeo-29-2019-2011.

Collins, R. L., C. C. Triplett, A. Barjatya, G. A. Lehmacher, and D. C. Fritts (2015), Using lidar and rockets to explore turbulence in the atmosphere, *SPIE Newsroom*, 7 May 2015, doi: 10.1117/2.1201505.005922

Crutzen, P. J., I. S. A. Isaksen, and G. C. Reid (1975), Solar Proton Events: Stratospheric sources of nitric oxide, *Science*, *189*(4201), 457-459, doi:10.1126/science.189.4201.457.

Cushman-Roisin, B., and J.-M. Beckers (2011), *Introduction to geophysical fluid dynamics*, 827 pp., Elsevier Academic Press, Massachusetts.

Farman, J. C., B. G. Gardiner, and J. D. Shanklin (1985), Large losses of total ozone in Antarctica reveal seasonal ClOx/NOx interaction, *Nature*, *315*(6016), 207-210, doi:10.1038/315207a0.

Fischer, H., and H. Oelhaf (1996), Remote sensing of verical profiles of atmospheric trace constituents with MIPAS limb-emission spectrometers, *Appl. Opt.*, *35*, 2787-2796, doi:10.1364/AO.35.002787.

Franke, P. M., and R. L. Collins (2003), Evidence of gravity wave breaking in lidar data from the mesopause region, *Geophys. Res. Lett*., 30, 1155, doi:10.1029/2001GL014477, 4.

Fritts, D. C., R. B. Smith, M. J. Taylor, J. D. Doyle, S. D. Eckermann, A. Dörnbrack, M. Rapp, B. P. Williams, P.-D. Pautet, K. Bossert, N. R. Criddle, C. A. Reynolds, P. A. Reinecke, M. Uddstrom, M. J. Revell, R. Turner, B. Kaifler, Johannes S. Wagner, T.Mixa, C. G. Kruse, A. D. Nugent, C. D. Watson, S. Gisinger, S. M. Smith, R. S. Lieberman, B. Laughman, J. J. Moore, W. O. Brown, J. A. Haggerty, A. Rockwell, G. J. Stossmeister, Steven F. Williams, G. Hernandez, D. J. Murphy, A. R. Klekociuk, I. M. Reid, and J. Ma (2016), The Deep Propagating Gravity Wave Experiment (DEEPWAVE): An Airborne and Ground-Based Exploration of Gravity Wave Propagation and Effects from Their Sources throughout the Lower and Middle Atmosphere, *Bull. Am. Met. Soc.*, 97, 425-453.

Fritts, D. C., and M. J. Alexander (2003), Gravity wave dynamics and effects in the middle atmosphere, *Rev. Geophys*., 41, 1003, doi:10.1029/2001RG000106

Funke, B., M. López-Puertas, H. Fischer, G. P. Stiller, T. von Clarmann, G. Wetzel, B. Carli, and C. Belotti (2007), Comment on “Origin of the January-April 2004 increase in stratospheric NO_2 observed in northern polar latitude” by Jean-Baptise Renard er al., *Geophys. Res. Lett.*, *34*, L07813, doi:10.1029/2006GL027518.

Garcia, R. R., D. R. Marsh, D. E. Kinnison, B. A. Boville, and F. Sassi (2007), Simulation of secular trends in the middle atmosphere, 1950–2003, *J. Geophys. Res.*, *112*, D09301, doi:10.1029/2006JD007485.

Gill, H. E. (1982), *Atmosphere–ocean dynamics*, 662 pp., Academic Press Inc., New York.

Harris, F. J. (1978), On the use of windows for harmonic analysis with the discrete Fourier transform, *Proc. IEEE*, 66, 51-83.

Harvey, V. L., R. B. Pierce, T. D. Fairlie, and M. H. Hitchman (2002), A climatology of stratospheric polar vortices and anticyclones, *J. Geophys. Res.*, *107*(D20), 4442, doi:10.1029/2001JD001471.

Hedin, A. E. (1991), Extension of the MSIS thermosphere model into the middle and lower atmosphere, *J. Geophys. Res., 96,* 1159 – 1172.

Hertzog, A., C. Souprayen, and A. Hauchecorne (2001), Observation and backward trajectory of an inertia-gravity wave in the lower stratosphere, *Ann. Geophys*., *19*, 1141-1155.

Hillert, W., F.-J. Lübken, and G. Lehmacher (1994), TOTAL: A rocket-borne instrument for high resolution measurements of neutral air turbulence during DYANA, *J. Atmos. Terr. Phys.*, *56*, 1835 – 1852.

Hines, C. O. (1960), On the rotation of the polar ionospheric regions, *J. Geophys. Res*., 65(1), 141–143, doi:10.1029/JZ065i001p00141.

Hitchman, M. H., J. C. Gille, C. D. Rogers, and G. Brasseur (1989), The separated polar winter stratopause: A gravity wave driven climatological feature, *J. Atmos. Sci.*, *46*(3), 410-422, doi:10.1175/1520-0469(1989)046%3C0410:TSPWSA%3E2.0.CO;2

Hoffmann, L., X. Xue, and M. J. Alexander (2013), A global view of stratospheric gravity wave hotspots located with Atmospheric Infrared Sounder observations, *J. Geophys. Res. Atmos.*, *118*, 416-434, doi:10.1029/2012JD018658.

Houghton, J. T. (1978), The stratosphere and mesosphere, *Quart. J. Royal Met. Soc*., *104*, 1-29.

Irving, B. K. (2012) *Rayleigh Lidar Studies of Mesospheric Inversion Layers at Poker Flat Research Range, Chantanika, Alaska*, 159 pp., MS Thesis, University of Alaska Fairbanks.

Irving, B. K., R. L. Collins, R. S. Lieberman, B. Thurairajah, and K. Mizutani (2014), Mesospheric Inversion Layers at Chatanika, Alaska (65°N, 147°W): Rayleigh lidar observations and analysis, *J. Geophys. Res. Atmos*., *119*, 11235–11249, doi:10.1002/2014JD021838.

Kolmogorov, A. N. (1941a), The local structure of turbulence in incompressible viscous fluid for very large Reynolds number, *Dokl. Akad. Nauk SSSR, 30*, 9–13 (reprinted in *Proc. R. Soc. Lond. A*, 434, 9–13, 1991).

Kolmogorov, A. N. (1941b), Dissipation of energy in the locally isotropic turbulence, *Dokl. Akad. Nauk SSSR, 32,* (reprinted in *Proc. R. Soc. London A.*, 434, 15-17, 1991).

Kundu, P. K., and I. M. Cohen (2008), *Fluid mechanics*, 872 pp., Elsevier Inc., Massachusetts.

Labitzke, K.G., and H. van Loon (1999), *The Stratosphere: Phenomena, History, and Relevance*, 179 pp., Springer-Verlag, Berlin.

Leblanc, T., I. S. McDermid, A. Hauchecorne, and P. Keckhut (1998), Evaluation of optimization of lidar temperature analysis using simulated data, *J. Geophys. Res.*, *103*(D6), 6177-6187.

Lehmacher, G. A., and F.-J. Lübken (1995), Simultaneous observation of convective adjustment and turbulence generation in the mesosphere, *Geophys. Res. Lett.*, *22*(18), 2477-2480, doi:10.1029/95GL02351.

Lehmacher, G. A., C. L. Croskey, J. D. Mitchell, M. Friedrich, F.-J. Lübken, M. Rapp, E. Kudeki, and D. C. Fritts (2006), Intense turbulence observed above a mesospheric temperature inversion at equatorial latitude, *Geophys. Res. Lett*., *33*, L08808, doi:10.1029/2005GL024345.

Lehmacher, G. A., T.D. Scott, M. F. Larsen, S. Bilén, C. L. Croskey, J. D. Mitchell, M. Rapp, F.-J. Lübken, and R. L. Collins (2011), The Turbopause experiment: atmospheric stability and turbulent structure spanning the turbopause altitude, *Ann. Geophys*., *29*, 2327-2339, doi:10.5194/angeo-29-2327-2011.

Li, J. (2016) *Radar Studies of Turbulence and Lidar Studies of the Nickel Layer in the Arctic Mesospere*, 119 pp., MS Thesis, University of Alaska Fairbanks.

Limpasuvan, V., M. J. Alexander, Y. J. Orsolini, D. L. Wu, J. H. Richter, and C. Yamashita (2011), Mesoscale simulation of gravity waves during the 2008-2009 major stratospheric sudden warming, *J. Geophys. Res.*, *116*, D17104, doi:10.1029/2010JD015190.

López-Puertas, M., B. Funke, T. von Clarmann, H. Fischer, and G. P. Stiller (2006), The stratospheric and Mesospheric NO_y in the 2002-2004 polar winters as measured by MIPAS/ENVISAT, *Space Sci, Rev.¸125*, 403-416, doi:10.1007/s11214-006-9073-2.

Lübken, F.-J. (1997), Seasonal variation of turbulent energy dissipation rates at high latitudes as determined by in situ measurements of neutral density fluctuations, *J. Geophys. Res.*, *102*(D12), 13,441–13,456, doi:10.1029/97JD00853.

Lübken, F.-J., W. Hillert, G. A. Lehmacher, and U. vonZahn (1993), Experiments revealing small impact of turbulence on the energy budget of the mesosphere and lower thermosphere, *J. Geophys. Res*., *98*(D11), 20369–20384, doi:10.1029/93JD02055.

Manney, G. L., M. L. Santeel, M. Rex, N. J. Livesey, M. C. Pitts, P. Veefkind, E. R. Nash, I. Wohltmann, R. Lehmann, L. Froidevaux, L. R. Poole, M. R. Schoeberl, D. P. Haffner, J. Davies, V. Dorokhov, H. Gernandt, B. Johnson, R. Kivi, E. Kyro, N. Larsen, P. F. Levelt, A. Makshtas, C. T. McElroy, H. Nakajima, M. Concepción Parrondo, D. W. Tarasick, P. von der Gathen, K. A. Walker, and N. S. Zinoviev (2011), Unprecedented Arctic ozone loss in 2011, *Nature*, *478*(7370), 469-477, doi:10.1038/nature10556.

Manney, G. L., Z. D. Lawrence, M. L. Santee, W. G. Read, N. J. Livesey, A. Lambert, L. Froidevaux, H. C. Pumphrey, and M. J. Schwartz (2015), A minor sudden stratospheric warming with a major impact: Transport and polar processing in the 2014/2015 Arctic winter, *Geophys. Res. Lett*., 42, 7808–7816, doi:10.1002/2015GL065864.

Matsuno, T. (1970), Vertical propagation of stationary planetary waves in the winter Northern Hemisphere, *J. Atmos. Sci.*, *37*, 871-883, doi:10.1175/1520-0469(1970)027%3C0871:VPOSPW%3E2.0.CO;2

Matsuno, T. (1971), A dynamical model of the stratospheric sudden warming, *J. Atmos. Sci.*, *28*, 1479-1494, doi:10.1175/1520-0469(1971)028<1479:ADMOTS>2.0.CO;2.

Meraner, K., and H. Schmidt (2016), Transport of nitrogen oxides through the winter mesopause in HAMMONIA, *J. Geophys. Res. Atmos.*, *121*, 2556-2570, doi:10.1002/2015JD024136.

Mertens, C. J., M. G. Mlynczak, M. López-Puertas, P. P. Wintersteiner, R. H. Picard, J. R. Winick, L. L. Gordly, and J. M. Russell III (2002), Retrieval of kinetic temperature and carbon dioxide abundance from nonlocal thermodynamic equilibrium limb emission measurements made by SABER experiment on the TIMED satellite, *Proc. SPIE. Int. Soc. Opt. Eng.*, *4882*, 162-171.

MSIS, (2016), *Virtual Ionosphere, Thermosphere, Mesosphere Observatory (VITMO) MSIS-E-90 Atmosphere Model,* Accessed in January 2016, Available at http://omniweb.gsfc.nasa.gov/vitmo/msis_vitmo.html

Obukhov, A. (1949). On the question of geostrophic wind (in Russian), *Izu. Akad. Nauk. SSSR Ser. Geografs.-Geofiz*., *13*(4), 281-306.

O’Sullivan, D., and T. J. Dunkerton (1995), Generation of inertia-gravity waves in a simulated life cycle of baroclinic instability, *J. Atmos. Sci*., 52, 3695-3716.

Papoulis, A. (1984), *Probability, random variables, and stochastic processes*, 576 pp., McGraw-Hill, New York.

Petterssen, S. (1953), On the relation between vorticity, deformation, and divergence and the configuration of the pressure field, *Tellus*, *5*, 231-237, doi:10.1111/J.2153-3490.1953.TB01052.x

Press, W. H., S. A. Teukolsky, W. T. Vetterling, and B. P. Flannery (1992), *Numerical recipes in Fortran: The art of scientific computing*, 2nd ed., 963 pp., Cambridge University Press, Massachusetts.

Randall, C. E., V. L. Harvey, C. S. Singleton, P. F. Bernath, C. D. Boone, and J. U. Kozyra (2006), *Geophys. Res. Lett.*, *33*, L18811, doi:10.1029/2006GL027160.

Randel, W., P. Udelhofen, E. Fleming, M. Geller, M. Gelman, K. Hamilton, D. Karoly, D. Ortland, S. Pawson, R. Swinbank, F. Wu, M. Baldwin, M.-L. Chanin, P. Keckhut, K. Labitzke, E. Remsberg, A. Simmons, and D. Wu (2004), The SPARC intercomparison of middle-atmosphere climatologies, *J. Climate*, *17*(5), 986-1003, doi:10.1175/1520-0442(2004)017<0986:TSIOMC>2.0.CO;2.

Rapp, M., Gumbel, J., and Lübken, F.-J. (2001) Absolute density measurements in the middle atmosphere, *Ann. Geophys*., *19*, 571-580, doi:10.5194/angeo-19-571-2001.

Remsberg, E. E., B. T. Marshall, M. García-Comas, D. Krueger, G. S. Lingenfelser, J. Martin-Torres, M. G. Mlynczak, J. M. Russell III, A. K. Smith, Y. Zhao, C. Brown, L. L. Gordley, M. J. Lopez-Gonzalez, M. López-Puertas, C.-Y. She, M. J. Taylor, and R. E. Thompson (2008), Assessment of the quality of the Version 1.07 temperature-versus-pressure profiles of the middle atmosphere from TIMED/SABER, *J. Geophys. Res.*, *113*, D17101, doi:10.1029/2008JD010013.

Ren, S., S. Polavarapu, S. R. Beagley, Y. Nezlin, and Y. J. Rochon (2011), The impact of gravity wave drag mesospheric analyses of the 2006 stratospheric major warming, *J. Geophys. Res.*, 116, D19116, doi:10.1029/2011JD015943

Richardson, L. F. (1922), *Weather prediction by numerical processes*, 236 pp., Cambridge University Press., Massachusetts.

Rienecker, M. M., M. J. Suarez, R. Gelaro, R. Todling, J. Bacmeister, E. Liu, M. G. Bosilovich, S. D. Schubert, L. Takacs, G.-K. Kim, S. Bloom, J. Chen, D. Collins, A. Conaty, A. da Silva, et al. (2011), MERRA:NASA's Modern-Era Retrospective Analysis for Research and Applications. *J. Climate*, *24*, 3624-3648, doi:10.1175/JCLI-D-11-0015.1.

Rossby, C. G. (1938), On the mutual adjustment of pressure and velocity distributions in certain simple current systems. II. *J. Marine Res.*, *7*, 239-263.

Scherhag, R. (1952), Die Explosionsartige Stratosphärenerwärmung des Spätwinters 1951/52. Ber. Dtsch. Wetterdienstes US Zone 6, 51–63.

Sinnhuber, M., B. Funke, T. von Clarmann, M. López-Puertas, and G. P. Stiller (2014), Variabillty of NO_x in the polar middle atmosphere from October 2003 to March 2004: Vertical transport versus local production by energetic particles, *Atmos. Chem. Phys. Discuss.*, *14*(1), 1-29, doi:10.5194/acpd-14-1-2014.

Smith, A. K., R. R. Garcia, D. R. Marsh, and J. H. Richter (2011), WACCM simulations of the mean circulation and trace species transport in the winter mesosphere, *J. Geophys. Res.*, *116*, D20115, doi:10.1029/2011JD016083.

Solomon, S. (1999), Stratospheric ozone depletion: A review of concepts and history, *Rev. Geophys.*, *37*(3), 275-316, doi:10.1029/1999RG900008.

SPARC, (2002), *SPARC intercomparison of middle atmosphere climatologies*, SPARC Rep 3., 96 pp.

Sutherland, B. R. (2010), *Internal Gravity Waves*, 377 pp., Cambridge University Press, New York.

Szewczyk, A. (2015), *Mesospheric Turbulence: The Role in the Creation of Mesospheric Inversion Layers and Statistical Results*, 148 pp., PhD Dissertation, Universität Rostock.

Tennekes, H., and J. L. Lumley (1972), *A first course in turbulence*, 300 pp., MIT press, Massachusetts.

Thurairajah, B. (2009) *Role of Waves on the Circulation of the Arctic Middle Atmosphere: Rayleigh Lidar Measurements and Anaylsis*, 182 pp., Ph.D. Dissertation, University of Alaska Fairbanks.

Thurairajah, B., R. L. Collins, and K. Mizutani (2009), Multi-year temperature measurements of the middle atmosphere at Chatanika, Alaska (65°N, 147°W), *Earth, Planets and Space*, *61*(6), 755-764.

Thurairajah, B., R. L. Collins, V. L. Harvey, R. S. Lieberman, and K. Mizutani (2010a), Rayleigh lidar observations of reduced gravity wave activity during the formation of an elevated startopause in 2004 at Chatanika, Alaska (65°N, 147°W), *J. Geophys. Res.*, *115*, D13109, doi:10.1029/2009JD013036.

Thurairajah, B., R. L. Collins, V. L. Harvey, R. S. Lieberman, M. Gerding, K. Mizutani, and J. M. Livingston (2010b), Gravity wave activity in the Arctic stratosphere and mesosphere during the 2007‐2008 and 2008‐2009 stratospheric sudden warming events, *J. Geophys. Res.*, *115*, D00N06, doi:10.1029/2010JD014125.

Triplett, C. C., R. Wing, R. L. Collins, and K. Mizutani (2014), A multi-year analysis of Rayleigh lidar measurements from the Poker Flat Research Range in Chatanika, Alaska, Poster session presented at: 2014 Coupling, Energetics, and Dynamics of Atmospheric Regions (CEDAR) Workshop, Seattle, Washington, 22-26 June

Triplett, C. C., R. L. Collins, V. L. Harvery, K. Neilsen, and K. Mizutani (2015a), Gravity wave activity over Chatanika, Alaska and its relationship to the wind field and geostrophic adjustment, Poster session presented at: 2015 Coupling, Energetics, and Dynamics of Atmospheric Regions (CEDAR) Workshop, Seattle, Washington, 21-25 June.

Triplett, C. C., R. L. Collins, G. Lehmacher, A. Barjatya, D. C. Fritts, F.-J. Lübken, B. Thurairajah, and V. L. Harvey (2015b), Connecting small-scale turbulence to large-scale dynamics in the mesosphere using the mesosphere-lower thermosphere turbulence experiment (MTeX), Presentaion at: 2015 American Geophysical Union (AGU) Fall Meeting, San Francisco, California, 14-18 December.

Wallace, J. M. and P. V. Hobbs (2006), *Atmospheric science: An introductory survey*, 483 pp., Elsevier Academic Press, Massachusetts.

Wayne, R. P. (2000), *Chemistry of Atmospheres*, 3rd ed., 775 pp., Oxford University Press, New York.

Weinstock, J. (1978), On the theory of turbulence in the buoyancy subrange of stably stratified flows. *J. Atmos. Sci.*, *35*, 634-649.

Weinstock, J. (1981), Energy dissipation rates of turbulence in the stable free atmosphere, *J. Atmos. Sci.*, *38*, 880-883.

Xu, J., A. K. Smith, R. L. Collins, and C.-Y. She (2006), Signature of an overturning gravity wave in the mesospheric sodium layer: Comparison of a nonlinear photochemical-dynamical model and lidar observations, *J. Geophys. Res*., *111*, D17301, doi:10.1029/2005JD006749.

Zhang, F., S. E. Koch, C. A. Davis, and M. L. Kaplan (2000), A survey of unbalanced flow diagnostics and their application, *Adv. Atmos. Sci.*, *17*, 205-218.

Zhang, F., S. E. Koch, C. A. Davis, and M. L. Kaplan (2001), Wavelet analysis and the governing dynamics of a large-amplitude mesoscale gravity-wave event along the East Coast of the United States, *Q. J. R. Meteorol. Soc*., *127*, 2209-2245.